

University of Nottingham
UK | CHINA | MALAYSIA

Evaluation of Encapsulated Rejuvenators Conventionally Used for Asphalt Self-Healing Enhancement as Architected Cellular Particles

Laura Traseira Piñeiro

Nottingham Transportation Engineering Centre (NTEC)

Department of Civil Engineering, The University of Nottingham, UK

Thesis submitted to The University of Nottingham for the degree of Doctor of Philosophy

December 2023

Abstract

Recent advancements in pavement engineering have introduced innovative materials and methods to enhance asphalt performance and promote road sustainability. Among these, encapsulated asphalt rejuvenators are gaining attention for their potential in extending the lifespan of pavements by promoting asphalt's self-healing capabilities. Asphalts containing this type of additive are regarded as smart materials, as the capsules, that are added to the asphalt during the mixing process, progressively release the bitumen rejuvenator in response to traffic loading. Thus, bitumen ageing, which causes asphalt to become stiffer and prone to cracking, can be controlled, and the binder regains its ability to flow and close any microcracks, preventing asphalt cracking.

The first research studies focused on examining different categories of asphalt rejuvenators, evaluating not only their effectiveness in restoring the chemical composition of the aged bitumen, but also their stability during the encapsulation process and their thermal degradation during asphalt manufacturing. Concerning the encapsulation process, although different encapsulation methods were evaluated, the prevalent manufacturing technique involved the external gelation of sodium alginate in the presence of calcium. Subsequently, research delved deeper into the optimization of the encapsulated rejuvenators through experimental testing, by assessing their effect on the crack-healing of damaged samples. However, the working mechanism of the capsules is still subject to some uncertainties. Although the calcium-alginate polymeric structure has been studied primarily for its capacity to progressively release the rejuvenator, the impact of the encapsulation structure itself, a cellular material with energy absorption properties, on asphalt performance and durability has not yet been thoroughly explored.

Firstly, this thesis examined the effect of cellular capsules on the mitigation of asphalt ravelling, which is, along with asphalt cracking, one of the most prevalent distresses on the road network. It was observed that asphalt's mass loss linearly decreased as the cellular capsule content was increased. When evaluating the effect

of the compaction level and the aggregate gradation on the mass loss of asphalt specimens with and without capsules, a correlation was found between the efficiency of the cellular capsules in mitigating the mass loss and the air void content of the asphalt mixtures. Moreover, after assessing changes in the internal porous structure of the capsules under loading through a combination of experimental testing and imaging techniques, it was found that the capsules were more than a release mechanism, as their cellular structure experienced a progressive collapse under impact-loading while absorbing energy, which may induce a local re-compaction in the asphalt mixture.

Based on these results, the focus shifted towards a comprehensive evaluation of the cellular capsules' impact on the performance of Stone Mastic Asphalt (SMA) manufactured at an asphalt plant. Variables throughout asphalt production that might influence the mechanisms governing the plastic deformation of the capsules containing an asphalt rejuvenator were evaluated in this assessment and then, results were contrasted with lab-produced asphalt under controlled conditions. Lastly, the capsules' deformation was qualitatively evaluated using a Finite Element (FE) model to verify findings from the testing campaign. It was concluded that cellular capsules can resist mixing at an asphalt plant without compromising their performance, and the deformation of the capsules affected asphalt's stability by up to 13%, reduced the particle loss by up to 25% and increased asphalt's macrotexture by 10%. It was also hypothesised that, to maximize their energy absorption, the cellular capsules must be part of the aggregate skeleton.

Lastly, a fundamental study was conducted to test the hypothesis made, in which the use of lattice structures that absorb energy as an alternative to cellular capsules containing asphalt rejuvenators was evaluated as well due to the advantages they offer in the design, optimisation, and manufacturing processes. Therefore, several lattice structures with a wide range of stiffness, strength, and energy-absorption properties were designed and 3D-printed, and two lattice structures with distinct properties were selected for the fundamental study. Subsequently, the mechanical behaviour of a composite granular medium composed of granite aggregates and either the cellular capsules previously manufactured or 3D-printed lattices was

investigated. Cyclic and monotonic experiments were conducted on this composite granular medium, to measure its mechanical response, the plastic deformation of lattice structures and cellular capsules, and the crushing behaviour of aggregates. Through a comparative analysis of results obtained from lattices with significantly different mechanical and energy-absorption properties, it was found that capsules induced physical changes to the aggregate skeleton of asphalt. Besides, despite design constraints, it was proved that lattice metamaterials could be successfully 3D-printed and tailored to meet specific requirements, and the Voronoi lattice emerged as a potential alternative to replace the capsules.

Keywords

Self-healing asphalt; encapsulated rejuvenators; capsules; cellular materials; energy-absorption; ravelling; mass loss; lattice metamaterials.

Acknowledgements

First and foremost, my sincere gratitude goes to my thesis supervisors, Alvaro Garcia-Hernandez and Gabriele Albertini, who guided me throughout my Ph.D. journey. Their mentorship, insightful guidance, and dedication to my academic growth have been pivotal in shaping the course of my research. I am also thankful for the support and guidance provided by Tony Parry and Gordon Airey, who participated in the thesis supervision as well. Their expertise and constructive feedback have greatly enriched my research.

The technical staff at the University of Nottingham and more particularly at NTEC (Nottingham Transportation Engineering Centre) has been an invaluable resource. Their unwavering support, access to resources, and technical expertise have been indispensable in my research journey.

The research presented in this thesis was made possible through the generous funding provided by Connect Plus. I would like to express my gratitude to Quintin Viljoen and Robert Murray for their dedication in securing the funding and overseeing the project's administration. Furthermore, I would like to acknowledge Frank Haughey, whose expertise and support significantly contributed to the successful completion of this research study.

I am deeply grateful to my family and friends, who have offered unwavering encouragement and support throughout my Ph.D. journey. My parents and brother have been there for me every step of the way, along with Belen and Paula, who I consider to be part of my family. Last but not least, I wish to express my gratitude to Alex for his unconditional support and understanding throughout this journey.

List of Publications

1. **Piñeiro, L. T.**, Parry, T.; Haughey, F.; & Garcia-Hernández, A. (2022). Architected cellular particles to mitigate asphalt stone loss. Construction and Building Materials, 328, 127056.

2. **Traseira-Piñeiro, L.**, Parry, T.; Haughey, F.; & Garcia-Hernandez, A. (2022). Performance of Plant-Produced Asphalt Containing Cellular Capsules. Materials, 15(23), 8404.

3. Ruiz-Riancho, N.; **Piñeiro, L. T.**; Abdalla, M. A.; & Garcia, A. (2022). Encapsulated bitumen rejuvenators for reflective cracking and ravelling mitigation. In Eleventh International Conference on the Bearing Capacity of Roads, Railways and Airfields (pp. 201-209). CRC Press.

4. Pasandín, A. R.; Hernandez, A. G.; Orosa, P.; **Piñeiro, L. T.**; Abdalla, M. A. (2023). Preliminary investigation on the suitability of using sodium alginate as an alternative binder for cold bituminous mixes. Carreteras, 239 (pp 18-26)

5. Under review by Construction and Building Materials: **Traseira-Piñeiro, L.**; Bodaghi, M.; Grizi, A.; Garcia, A & Albertini, G. Energy-absorbing particles for enhanced mechanical performance of asphalt's aggregate skeleton.

Declaration

The research described in this thesis was conducted at the Nottingham Pavement Engineering Centre (NTEC), from the University of Nottingham, between October 2019 and December 2023. This thesis is my work, except for the work of other authors that have been referenced. No part of this thesis has been submitted for any degree at another University.

Laura Traseira Piñeiro

The University of Nottingham

Contents

Abstract ... **ii**
Acknowledgements ... **v**
List of Publications ... **vi**
Declaration ... **vii**
Contents ... **viii**
List of Figures ... **xii**
List of Tables ... **xvii**
List of Abbreviations ... **xviii**

Chapter 1. Introduction ... **1**
1.1 Background ... 1
1.2 Motivation ... 3
1.3 Aims and Objectives ... 4
1.4 Research Methodology ... 5

Chapter 2. Literature Review ... **8**
2.1 Introduction ... 8
2.2 Asphalt Pavements ... 9
2.2.1 Pavement Classification ... 9
2.2.2 Flexible Pavement Layers ... 10
2.2.3 Hot Mix Asphalt ... 11
2.3 Pavement Deterioration ... 16
2.3.1 Primary Causes of Pavement Deterioration ... 16
2.3.2 Main Types of Damage in Pavements ... 18
2.4 Asphalt Self-Healing ... 29
2.4.1 Self-Healing Mechanism ... 29
2.4.2 Manufacturing of Encapsulated Rejuvenators ... 32
2.4.3 Characterization of Encapsulated Rejuvenators ... 39
2.4.4 Evaluation of Asphalt Containing Encapsuled Rejuvenators ... 43
2.4.5 Numerical Models ... 48
2.5 Lattice Metamaterials ... 49
2.5.1 Metamaterials ... 49
2.5.2 Lattice Metamaterials ... 51

2.5.3 Lattice Manufacturing 53
2.5.4 Lattice Characterization 54

Chapter 3. Materials and Methods 57

3.1 Introduction 57
3.2 Capsule Manufacturing 58
3.2.1 Capsule Production in the Laboratory 58
3.2.2 Upscaled Methodology for Capsule Production 59
3.3 Asphalt Manufacturing 62
3.3.1 Raw Materials 62
3.3.2 Asphalt Mixtures Composition 63
3.3.3 Sample Manufacturing 64
3.4 Lattice Manufacturing 67
3.4.1 Materials and Advanced Manufacturing 67
3.4.2 Lattice Design 68
3.5 Testing Methods 71
3.5.1 Evaluation of the Capsule Size and Morphology 71
3.5.2 Capsule Imaging Through Computer Tomography Scanning 72
3.5.3 Capsule Imaging Through Scanning Electron Microscope 72
3.5.4 Evaluation of the Capsule's Distribution and Morphology in Asphalt 73
3.5.5 Evaluation of the Capsule Density 74
3.5.6 Uniaxial Compression Testing of Capsules 74
3.5.7 Evaluation of Asphalt's Bulk Density and Air Void Content 74
3.5.8 Aggregate Loss Test 75
3.5.9 Rutting Resistance Test 77
3.5.10 Semi-Circular Bending Test 77
3.5.11 Evaluation of Asphalt Energy Absorption Under Compression Testing 78
3.5.12 Evaluation of Asphalt Skid Resistance 78
3.5.13 Evaluation of Asphalt Texture 79
3.5.14 Evaluation of Oil Released from the Capsules After Testing 79
3.5.15 Characterization of Asphalt Mastic Rheological Properties 80
3.5.16 Characterization of Materials Used for MJF 81
3.5.17 Mechanical Characterization of Lattice Structures 81
3.5.18 Evaluation of the Manufacturability of the Proposed Lattice Structures 83
3.5.19 Mechanical Response of a Composite Granular Medium Containing Energy-absorbing Particles 83

3.6 Finite Element Modelling 86
3.6.1 Microstructural Model 86
3.6.2 Determination of the Material Properties 87
3.6.3 Evaluation of Results from the FE Model 90

Chapter 4. Evaluation of Cellular Capsules to Mitigate Asphalt Stone Loss...91
4.1 Introduction 91
4.2 Size and Structure of the Cellular Capsules 92
4.3 Effect of Cellular Capsules on Mass Loss, Rutting and Skid Resistance 93
4.4 Effect of Compaction Energy on Mass Loss 96
4.5 Effect of Asphalt Gradation on Mass Loss 97
4.6 Influence of AVC on Mass Loss 99
4.7 Influence of Cellular Capsules on Asphalt Volumetric Properties 100
4.8 Assessment of the Cellular Capsule Deformation During Testing 101
4.9 Assessment of Energy Absorption Under Loading 103

Chapter 5. Performance of Plant-produced Asphalt Containing Cellular Capsules 107
5.1 Introduction 107
5.2 Physical and Mechanical Properties of the Cellular Capsules 108
5.3 Cellular Capsule Distribution and Integrity in Plant-Produced Asphalt Samples 109
5.4 Characterization of Plant-Produced Asphalt 111
5.5 Evaluation of Plant-Produced Asphalt Performance 112
5.6 Validation of Results at the Laboratory Scale: Effect of Mixing Time 114
5.7 Validation of Results at the Laboratory scale: Effect of Bitumen Content Variations 116
5.8 Numerical Simulations Using FEM 118

Chapter 6. Evaluation of Lattice Metamaterials for Enhanced Asphalt Performance 120
6.1 Introduction 120
6.2 Characterization of Materials Used for MJF 121
6.3 Manufacturability of the Proposed Lattices 121
6.4 Evaluation of the Lattice Mechanical Performance 122
6.5 Lattice Selection for Testing in a Granular Medium 126
6.6 Mechanical Response in a Granular Unbound Medium 128

Chapter 7. Conclusions.....134
7.1 Conclusions..... 134
7.2 Evaluation of Cellular Capsules to Mitigate Asphalt Stone Loss..... 135
7.3 Performance of Plant-produced Asphalt Containing Cellular Capsules..... 136
7.4 Evaluation of Lattice Metamaterials for Enhanced Asphalt Performance.. 137
7.5 Recommendations For Future Research 138
References..... a
Appendix I .....s

List of Figures

Figure 2.1. Schematic representation of the load distribution pattern in flexible pavements. 10
Figure 2.2. Flexible pavement layers, extracted from [40]. 11
Figure 2.3. Schematic representation of several asphalt mixtures: (a) Dense-graded, (b) open-graded and, (c) gap-graded. Extracted from [42]. 12
Figure 2.4. Particle Size Distribution (PSD) of dense-graded mixtures (fine-graded and coarse-graded) and maximum density line. Extracted from [47]. 13
Figure 2.5. PSD of an open-graded mixture and maximum density line. Extracted from [47]. 14
Figure 2.6. PSD of a gap-graded mixture (SMA) and maximum density line. Extracted from [47]. 15
Figure 2.7. Generic distresses commonly found on pavements with asphalt surfacing. Extracted from [32]. 18
Figure 2.8. (a) Bottom-up cracking and, (b) top-down cracking. Extracted from [87]. 20
Figure 2.9. Reflective cracking mechanism. Extracted from [91]. 22
Figure 2.10. Shear stresses generated by the vehicles on the pavement surface. Extracted from [92]. 23
Figure 2.11. Modes of failure in asphalt ravelling: (a) Cohesive damage and, (b) adhesive damage. Extracted from [94]. 23
Figure 2.12. Increase of the tensile stress in the asphalt mixture due to the presence of water. Extracted from [96]. 24
Figure 2.13. Pavement texture and wavelength. Extracted from [113]. 28
Figure 2.14. CT scans of the self-healing process of a beam made of SMA. Extracted from [123]. 29
Figure 2.15. Changes in the SARA fractions over time due to oxidative ageing. Extracted from [95]. 31
Figure 2.16. Representation of asphalt crack healing using encapsulated rejuvenators. Extracted from [26]. 32

Figure 2.17. Morphologies evaluated for encapsulated asphalt rejuvenators. Extracted from [29]. 35
Figure 2.18. Different morphologies of encapsulated rejuvenators: (a) Saturated aggregates [143], (b) double-shell core microcapsules [146], (c) polymeric spheres [147] and, (d) compartmented fibres[148]. 36
Figure 2.19. Manufacturing of encapsulated rejuvenators by external gelation of sodium alginate in the presence of calcium using a dripping technique. Extracted from [140]. 38
Figure 2.20. Reconstruction from CT scans of a sample containing capsules: (a) cross-sectional area of the samples, (b) detailed 3D visualisation of the capsules and, (c) 3D reconstruction of the sample. Extracted from [163]. 41
Figure 2.21. Evaluation of the thermal and volumetric stability of sodium alginate capsules containing sunflower oil: (a) TGA results and, (b) TMA results. Extracted from [164]. 43
Figure 2.22. Schematic representation of the test method developed to evaluate asphalt crack healing by 3PB testing. Extracted from [31]. 46
Figure 2.23. Test method developed to evaluate asphalt crack healing by reflective cracking fatigue testing: (a) Schematic representation and (b) testing equipment. Extracted from [159]. 48
Figure 2.24. Potential applications of metamaterials in civil engineering. 50
Figure 2.25. Lattice classification made by Bhate et al. Extracted from [192] 53
Figure 2.26. Stress-strain and efficiency-strain graphs of: (a) An ideal energy absorber and, (b) an experimental energy absorber. 55
Figure 3.1. Steps for manufacturing capsules in the laboratory. 59
Figure 3.2. Capsule formation step with the upscaled methodology for capsule manufacturing. 60
Figure 3.3. Capsules at different steps of the manufacturing process: (a) After collection from the calcium chloride solution, (b) before drying with the filler coating and, (c) after drying and sieving. 61
Figure 3.4. Generation of: (a) Periodic metamaterials (beam-based lattices and walled TPMS) and (b) non-periodic metamaterials (Voronoi tessellation). 69

Figure 3.5. Examples of 3D-printed lattices (left) and, lattice design from which they were 3D-printed (right): (a) BCC, (b) Octet, (c) Voronoi, (d) Diamond, (e) Splitp and, (f) Lidinoid. 70
Figure 3.6. Shape descriptors of the cellular capsules. 71
Figure 3.7. Schematic representation depicting the interior of Los Angeles abrasion machine during the Cantabro test. 75
Figure 3.8. Set-up for uniaxial compression testing of the unbound granular medium. 85
Figure 3.9. Example of a microstructural model and its components, including the stone-capsule-stone surrounded by mastic, a rigid frame surrounded by asphalt, and a rigid plate to apply uniaxial compression. 87
Figure 3.10. Experimental and numerical results of uniaxial compression testing of: (a) Cellular capsules and, (b) stone mastic asphalt. 88
Figure 3.11. Results from DSR of asphalt mastic, master curve fitting and Prony series fitting at 20 °C..... 89
Figure 4.1. Distribution of the cellular capsule equivalent circular area diameter. 92
Figure 4.2. (a) CT reconstruction of an energy-absorbing particle after manufacturing and drying and, (b) top view scan of its inner structure. 93
Figure 4.3. Results from ravelling testing for different cellular capsule contents: (a) Mass loss after 300 cycles and (b) degradation curves. 94
Figure 4.4. Cores with different content of cellular capsules after the Cantabro test (300 cycles) and RGB values for each asphalt sample set..... 95
Figure 4.5. Results from rutting testing for different cellular capsule contents: (a) Proportional rut depth over cycles and (b) summary of results. 95
Figure 4.6. Effect of the compaction energy (number of blows per face using the Marshall compactor) on the mass loss of asphalt containing 0% and 1% of cellular capsules. 97
Figure 4.7. Effect of the asphalt gradation on the mass loss of asphalt containing 0% and 1% of cellular capsules. 98
Figure 4.8. Photographs of asphalt cores after the Cantabro test with and without cellular capsules, and physical properties of the cores before testing. 98

Figure 4.9. Mass loss and AVC of asphalts containing 0% and 1% of cellular capsules. 99
Figure 4.10. Efficiency index for asphalt mixtures containing 1% of cellular capsules, based on the Air Void Content (AVC). 100
Figure 4.11. Correlation between Air Void Content (AVC) of asphalt mixtures with and without cellular capsules. 101
Figure 4.12. Shape descriptors of cellular capsules embedded in asphalt slabs containing 1% of cellular capsules after testing in the Hamburg wheel tracker... 102
Figure 4.13. (a) Diagram of cellular capsule deformation under loading and interaction within the aggregate skeleton, (b) CT-scan of the top view of a cellular capsule extracted from a core specimen after the Cantabro test and, (c) reconstruction of a cellular capsule damaged by the aggregates after impact loading in the Los Angeles machine. 103
Figure 4.14. (a) Compressive load-strain diagram of a cellular capsule, (b) Compressive load-strain curve of asphalt containing 0% and 1% of cellular capsules (c) Energy absorbed by asphalt containing a range of percentages of cellular capsules under compression testing. 104
Figure 4.15. Action mechanism of the cellular capsules. 105
Figure 5.1. SEM images of the inner and outer structure of a bisected cellular capsule..... 108
Figure 5.2. 3D reconstruction of plant-produced asphalt specimens containing cellular capsules, and average number of capsules per mm of height, from batches: (a) B2, (b) B3, (c) B4. 110
Figure 5.3. Results from semi-circular bending test and Air Void Content (AVC) calculations of asphalt manufactured at Mountsorrel Tarmac asphalt plant..... 112
Figure 5.4. Results from the Cantabro test: (a) Percentage of mass loss and (b) aggregate gradation of the lost aggregates. 113
Figure 5.5. (a) Proportional rut depth of asphalt samples after wheel/tracking and (b) reconstruction from the scanned lines of a specimen in the mid-centre before (MPD of 1.50 mm) and after (MPD of 1.56 mm) wheel tracking. 114
Figure 5.6. Testing of NTEC asphalt mixtures with different binder contents with 0% and 0.5% of capsules: (a) AVC, (b) ravelling resistance, (c) rutting resistance

and (d) initial and final asphalt macrotexture during the Hamburg wheel tracking test. 116
Figure 5.7. Total displacement U (in mm) in the FE model after applying uniaxial compression for the five variations in the case study altering the area of mastic. From (a–e), AR of the capsule after loading: 1.35, 1.30, 1.20, 1.14, 1.12. 119
Figure 6.1. Results from uniaxial compression of the lattices, and selected lattices for further evaluation: (a) Young modulus, (b) average stress plateau, (c) energy absorbed, (d) peak stress, (e) maximum efficiency and (f) recovered strain. 124
Figure 6.2. Compressive stress-strain curve and deformation during mechanical testing of the selected lattices made of PA11: (a) Voronoi with 40 points and randomness 2 and, (b) Lidinoid with a unit cell size of 4 mm^3. 126
Figure 6.3. Stress-strain and efficiency-strain graphs of a Voronoi lattice under uniaxial compression (a), with (b) photographs taken at different strain levels during testing. 127
Figure 6.4. Testing of the granular unbound medium under uniaxial compression: (a) Load -strain curves on samples containing cellular capsules, (b) energy absorption on samples containing cellular capsules, (c) load-strain curves on samples containing spherical lattices and (d) energy absorption on samples containing spherical lattices. 129
Figure 6.5. Testing of the granular unbound medium under cyclic loading on: (a) samples containing cellular capsules) and (b) samples containing spherical lattices. 130
Figure 6.6. Particle Size Distribution (PSD) curves after uniaxial compression under cyclic loading. 131
Figure 6.7. Evaluated energy-absorbing particles before and after testing, including: (a) Images of the cellular capsules using the ESEM, (b) photographs of PA66, (c) photographs of Voronoi lattices and (d) photographs of Lidinoid lattices. 133

List of Tables

Table 2.1. Factors that can initiate and/or accelerate ravelling, based on [96]. 25
Table 2.2. Asphalt rejuvenators classification and examples, based on [24] and [132]. 33
Table 2.3. Classification of the methodologies used to characterise capsules, based on [160]. 39
Table 3.1. Summary of materials and methods from Chapter 3. 57
Table 3.2. Cellular capsule composition. 61
Table 3.3. Aggregate gradations of the nominal sizes used for asphalt manufacturing. 62
Table 3.4. Asphalt mixture compositions used in Chapter 4 and Chapter 5. 63
Table 3.5. Details of the core manufacturing for Chapter 4. 65
Table 3.6. Times for adding cellular capsules into the asphalt during the mixing stage in Chapter 5. 66
Table 3.7. Material properties for the FE model. 88
Table 5.1. Compositional analysis of asphalt manufactured at Mountsorrel Tarmac asphalt plant. 111
Table 5.2. Testing of lab asphalt mixtures varying the mixing process on asphalt containing cellular capsules. 115
Table 6.1. Results from tensile testing polyamides PA11 and PA12. 121
Table 6.2. Lattices discarded due to manufacturability (M) or integrity (I) issues, classififed by the material type (PA11or PA12), Unit Cell size (UC of 4mm, 5mm or 6mm) and type of unit cell. 122
Table 6.3. Pearson correlation coefficients of the relationships between the evaluated variables used to characterise the mechanical performance of the lattices. 125
Table 6.4. Geometrical measurements of the evaluated energy-absorbing particles before and after testing in a granular unbound medium. 132

List of Abbreviations

AC	Asphalt Concrete
AFM	Anatomic Force Microscopy
AM	Additive Manufacturing
AR	Aspect Ratio
ASTM	American Society for Testing and Materials
ATPB	Asphalt Treated Permeable Bases
ATR-FTIR	Attenuated Total Reflectance Fourier- Transform Infrared
AVC	Air Void Content
CAD	Computed Aid Design
CT	Computer Tomography
DLS	Dynamic Light Scattering
DMF	Discrete Multi- Physics model
DMLS	Direct Metal Laser Sintering
DMRB	Design Manual of Roads and Bridges
DSC	Differential Scanning Calorimetry
DSR	Dynamic Shear Rheometer
EALF	Equivalent Axle Load Factor
EBM	Electron Beam Melting
EDS or EDX	Dispersive X-ray Spectroscopy
EI	Efficiency Index
ESAL	Equivalent Standard Axle Load
ESALF	ESAL factors
ESEM	Scanning Electron Microscope
FDM	Fused Deposition Modelling
FEM	Finite Element Modelling
FIB	Focused Ion Beam
FTIR	Fourier Transform Infrared spectroscopy
HBGM	Hydraulically Bound Granular Material
HMA	Hot Mix Asphalt
ICP-OES	Inductively Coupled Plasma Optical Emission Spectroscopy
IRI	International Roughness Index
ITS	Indirect Tensile Strength
ITSM	Indirect Tensile Stiffness Modulus
JRC	Jointed Reinforced Concrete
MAD	Median Absolute Deviation
MJF	Multi Jet Fusion

ML	Mass Loss
MMF	Melamine–Formaldehyde modified by Methanol
MPD	Mean Profile Depth
MUF	Melamine-Urea-Formaldehyde
OGFC	Open Graded Friction Courses
PA	Porous Asphalt
PBF	Powder Bed Fusion
PLA	Polylactic Acid
PSD	Particle Size Distribution
PSV	Polished Stone Value
PTV	Pendulum Test Value
RCC	Roller Compacted Concrete
ROI	Regions Of Interest
SARA	Saturates, Aromatics, Resins and Asphaltenes
SEM	Scanning Electron Microscope
SLA	Stereolithography
SLS	Selective Laser Sintering
SMA	Stone Mastic Asphalt
SPAs	Saturated Porous Aggregates
SSD	Saturated Surface Dry
TDC	Top-Down Cracking
TEM	Transmission Electron Microscopy
TGA	Thermo-gravimetrical analysis
TMA	Thermomechanical Analyser
TPMS	Triply Periodic Minimal Surfaces
TSTM	Tensile Strength Testing Machine
URC	Unreinforced Jointed Concrete
UTM	Universal Testing Machine
WCO	Waste Cooking Oil
WEO	Waste Engine Oil
WMA	Warm Mix Asphalt
WTS	Wheel Track Slope
XRD	X-Ray Diffraction

Chapter 1. Introduction

1.1 Background

In the UK, asphalt mixtures are used on 95% of road pavements, with an approximate annual production of 25 million tonnes [1]. This material is composed of graded aggregates, which provide stiffness and resistance to cumulative deformations, and bitumen, a viscous binder material whose primary function is to hold the aggregates together. Because of their viscoelastic properties, bitumen-bound materials can flow within the bitumen-filler mortar, reducing the risk of cracking due to temperature fluctuations or foundation settlements [[2],[3]].

One of the most popular surfacing materials in the UK is Stone Mastic Asphalt (SMA), primarily due to its exceptional performance in terms on rut and fatigue resistance, particularly on pavements with heavy traffic and loads, as well as its rough surface texture [4]. The stone-on-stone contact between the coarse aggregates creates a strong skeleton, providing stability, whereas the voids are partially filled with a bituminous mortar composed of filler and fines, increasing durability [5]. Hence, despite their initial higher cost when compared to dense graded mixtures, SMA mixtures can result in a great investment due to their increased lifespan [6]. Nevertheless, this surfacing material is exposed as well to traffic loads and environmental factors such as temperature, moisture, and frost over its service life, which can contribute to the pavement deterioration and result in asphalt distresses that include asphalt cracking, ravelling, or rutting, among others [7].

Asphalt cracking and ravelling are among the most prevalent distresses on the network. However, surface cracking in gap-graded mixtures is often caused by reflective cracking from the underneath layer, which constitutes a structural problem [[8],[9]]. Ravelling, on the other hand, has a high occurrence on thin overlays and high-textured materials. The loss of aggregates, caused by a weak bond in the stone-

on-stone contact, can be prompted either by cohesive failure of the binder or adhesive failure in the bitumen-aggregate interface [10]. Although several factors may influence ravelling, such as bitumen ageing, it is a particularly concerning distress during wet seasons due to moisture that affects bitumen's cohesive strength and adhesive bond in the interface region. Once initiated, asphalt ravelling rapidly intensifies in the surrounding areas, reducing pavement's service life and requiring maintenance [11]. Rutting is also a concerning material distress, but SMA mixtures are known for their high stability against plastic shear deformations [12]. In most cases, rutting occurs because the asphalt layer is not strong enough to bear the traffic loads, due to inappropriate interlocking or aggregate distribution in the mixture. Consequently, rutting can accelerate pavement deterioration by reducing the drainage capacity and increasing the risk of moisture damage and bleeding [13].

Pavement engineering has advanced significantly over the past decades, with new design approaches and alternative materials to enhance asphalt's performance while constructing more sustainable roads [14]. As an example, warm-mix and cold-mix asphalts use bitumen additives and emulsions to lower the manufacturing temperatures [[15],[16]], and their rheological properties can be altered as well by polymer modification [17], antioxidants [18], or adhesion agents [19], among others. There is an increasing interest in alternatives to natural aggregates, such as recycled aggregates [20], industrial waste products like steel slag or fly ash [21], or crumb rubber from used tyres [22]. Moreover, recycled plastics with high melting points are being evaluated to replace part of the aggregates of asphalt mixtures [23].

In this context, the use of asphalt rejuvenators, whether through spraying or encapsulation methods, has received significant attention within the research community due to their potential for extending the lifespan of asphalt pavements [24]. This technological innovation is based on promoting asphalt self-healing by means of a rejuvenator that is progressively released from the capsule in which it is stored. Thus, bitumen ageing, which causes asphalt to become stiffer and prone to cracking due to an imbalance in the ratio of asphaltenes to maltenes, can be controlled by reconstituting the chemical composition of the binder, regaining its ability to flow and close microcracks [25].

1.2 Motivation

Encapsulated rejuvenators were originally designed for enhancing asphalt self-healing by the progressive release of a rejuvenator that restores the properties of aged bitumen, promoting the healing of cracks [26]. The capsules containing a rejuvenator agent are added to the asphalt during the mixing process, therefore they must resist the stresses and high temperatures induced during asphalt manufacturing. Then, the rejuvenator is progressively released through a mechanism that requires a mechanical load to activate the capsules, followed by a chemical interaction to restore the binder's composition, promoting then the binder flow in a porous medium to seal the microcracks with the restored binder [27].

Diverse types of rejuvenators have been evaluated over time and extensive endeavours have been dedicated to the effective encapsulation of asphalt rejuvenators. It has been reported that vegetable oils and waste cooking oils outperformed petroleum-based and waste engine oils when studying their effect on the rheological properties of the binder [28]. As to the encapsulating process, the external gelation of sodium alginate in the presence of calcium emerged as the most prevalent manufacturing technique. Moreover, the polymeric encapsulated rejuvenators manufactured with this physico-chemical method remain the subject of ongoing investigation for enhancing asphalt self-healing capabilities [29].

Most of the research studies have been focused on evaluating the release and diffusion of the rejuvenator, optimising the design of the capsules through an iterative process based on experimental testing, and assessing the crack-healing and strength recovery of asphalt containing encapsulated rejuvenators on samples with crack damage induced during cyclic loading [[30],[31]]. However, there are some uncertainties regarding their working mechanism. Indeed, while the primary purpose of the polymeric structure made of calcium-alginate initially was to facilitate the release of an asphalt rejuvenator and promote the self-healing of asphalt cracks, the impact of the encapsulation structure itself, a cellular material with energy absorption properties, on asphalt performance and durability has yet to be investigated.

1.3 Aims and Objectives

Past research on encapsulated rejuvenators focused on evaluating the release and diffusion of the rejuvenator and assessing its influence on the self-healing of asphalt cracks. However, despite the potential benefits encapsulated rejuvenators may offer, some unknowns remain about their functioning mechanism. The primary aim of this thesis was to investigate the potential of the cellular capsules in enhancing the energy absorption and durability of asphalt materials. First, laboratory tests were conducted to investigate the influence of the capsules on asphalt ravelling. Based on the initial findings, the study progressed to testing cellular capsules in asphalt produced at an asphalt plant, analysing key performance characteristics. Then, the hypothesis extracted from the practical assessment was validated with a fundamental study.

To accomplish this aim, the following research objectives were outlined:

- Demonstrate the delay of asphalt's aggregate loss by the addition of cellular capsules to asphalt mixtures and assess changes in the internal porous structure of the capsules under loading.
- Evaluate the influence of cellular capsules on the performance of asphalt produced at an industrial site, examining the capsules as cellular materials with energy-absorption properties. In addition, analyse critical variables throughout asphalt manufacturing at an asphalt plant that may affect the mechanisms governing the plastic deformation of the capsules.
- Investigate the non-negligible physical influence of the cellular capsules on asphalt through a fundamental study to test the hypothesis made and evaluate the feasibility of using 3D-printed lattice structures as an alternative to the cellular capsules.

1.4 Research Methodology

To accomplish the aforementioned objectives, the research methodology was divided into the following phases:

Phase 1: Evaluation of cellular capsules to mitigate asphalt aggregate loss

First, cellular capsules containing an asphalt rejuvenator were manufactured at a laboratory scale using the set-up utilised in prior research, and their size and morphology were characterised though imaging techniques, including CT-scanning. Then, SMA mixtures with different contents of capsules (0.0%, 0.5%, 1.0%, 1.5%, 2.0%) were manufactured and tested by means of mass loss (Cantabro test), rutting (Hamburg wheel tracking) and skid resistance testing (pendulum test), to identify the optimum capsule content for the testing programme. The next step involved manufacturing asphalt sample sets with the selected capsule content (in addition to the baseline sample set without cellular capsules) varying the compaction energy and asphalt gradation. The air void content of the samples was determined and then, their mass loss was quantified using the Cantabro test, to investigate correlations among asphalt's physical properties and the efficiency of the capsules in terms of ravelling mitigation.

Lastly, the deformation of the cellular capsules in the asphalt during testing was studied and correlated to their microstructure. The cross-section of asphalt slabs with the selected content of capsules was examined through digital image analysis after rutting testing, to assess changes in the morphology of the capsules by comparing tested and untested regions. Thereafter, samples extracted from tested cores after the Cantabro test were CT-scanned to document changes in their internal porous structure, as well as the deformation of the capsules in the contact areas with the aggregates. This study was completed with an assessment of the energy absorption properties of asphalt containing several percentages of capsules (0.0%, 0.5%, 1.0%, 1.5%, 2.0%), using uniaxial compression testing.

Phase 2: Evaluation of the performance of plant-produced asphalt containing cellular capsules

First, cellular capsules were manufactured with a scaled-up procedure to attain the quantity required for the testing programme. CT-scanning and SEM imaging were used to characterize the capsules' morphology and internal porous structure, and their mechanical properties were determined through uniaxial compression testing. Then, an SMA mixture was manufactured at an asphalt plant producing a total of four batches of half a tonne each, including the baseline without capsules and three batches in which the capsules were added at different stages of the manufacturing process (with the aggregates before pouring the binder, at the beginning of the mixing stage and at the end of the mixing stage). Thereafter, to determine if mixing at an asphalt plant could affect their distribution and integrity, samples of plant-produced asphalt after compaction in the laboratory were CT-scanned to examine the capsules.

Then, prior to the evaluation of the morphological and mechanical properties of the SMA mixtures produced at the asphalt plant, the samples were subjected to a compositional analysis to detect any inconsistencies due to the variability associated with the technologies employed to dose the materials, and the semi-circular bending test was performed to assess whether disparities in the asphalt composition might impact its performance. Asphalt evaluation encompassed an assessment under impact loading (Cantabro test) and cyclic loading (wheel-tracking test), and the determination of asphalt air void content and texture by means of mean profile depth (MPD). However, due to the disparities detected in the binder dosing, a validation with asphalt produced at the lab under controlled conditions was conducted as well, assessing separately the influence of the mixing stage in which capsules were incorporated into the asphalt and variations in the binder content of the batch. Lastly, a simplified FE case study verified the findings from experimental testing with a numerical simulation.

Phase 3: Fundamental study of cellular capsules and lattice metamaterials in a granular unbound medium

Several lattice structures were designed and 3D-printed, varying the type and size of the unit cells to inspect different morphologies and relative densities. Then, the materials used for 3D-printing the particles were characterised through tensile testing, and the mechanical response of the lattice metamaterials was evaluated through uniaxial compression testing, as well as their manufacturability. Two lattice structures with distinctly different mechanical properties were then selected for further evaluation in the second stage.

In the second stage, both the cellular capsules and lattice structures were tested in a granular unbound medium under static and cyclic compression loading. In this fundamental study, the variability associated with the binder dosing and the potential challenges that may arise during the mixing process were discarded and, to further minimise gradation inconsistencies, single-size granite stones were used to evaluate the cellular capsules and the selected 3D-printed lattices, ensuring that the granular media were geometrically similar. Moreover, to discard the effect of introducing spherical particles on the granite granular medium, additional testing was performed using solid Nylon spheres made of PA66 with negligible energy absorption properties. This fundamental study compared the effect of different energy-absorbing particles on the overall response of the composite granular unbound medium, as well as the deformation of the particles and the crushing behaviour of the granite aggregates. Throughout this fundamental study, not only the hypothesis from the previous phases of this research could be tested, but also potential alternatives to the capsules were assessed.

Chapter 2. Literature Review

2.1 Introduction

The use of encapsulated rejuvenators as a method to promote asphalt self-healing has been widely investigated over the past few years. Asphalts containing this type of additive are regarded as smart materials, as the capsules progressively release a bitumen rejuvenator in response to the traffic loading, promoting the binder flow to seal any microcracks and prevent asphalt cracking, thereby increasing the pavement's lifespan. However, despite the potential benefits encapsulated rejuvenators may offer, some unknowns remain about their functioning mechanism, which has been mainly evaluated through lab-based studies.

This chapter aims to evaluate the literature concerning the use of encapsulated rejuvenators for asphalt self-healing purposes, encompassing the manufacturing and characterization of the capsules, and the assessment of asphalt containing encapsulated rejuvenators through experimental studies and numerical modelling. It is, however, imperative to provide an overview of flexible pavements and the most common asphalt mixtures used, as well as review the main types of asphalt distress, with a special focus on asphalt cracking and ravelling. Lastly, the properties of lattice metamaterials and their applications in civil engineering are included in this literature review, as they form part of the research included in this thesis.

2.2 Asphalt Pavements

2.2.1 Pavement Classification

From a road engineering perspective, a pavement is a horizontal structure supported by in situ natural materials, with the main objective of distributing traffic loading to the subgrade while avoiding a loss of the supporting soil's bearing capacity due to excessive stresses [32]. In the United Kingdom, pavement construction types are classified by the Design Manual of Roads and Bridges (DMRB) as [33]:

- Flexible pavements with an asphalt base layer
- Flexible pavements with a Hydraulically Bound Granular Material (HBGM) base layer
- Rigid pavements, including Roller Compacted Concrete (RCC), Unreinforced Jointed Concrete (URC) and Jointed Reinforced Concrete (JRC)

The main difference between rigid and flexible pavement lies in the load distribution characteristics [34]. In flexible pavements, an asphalt surface is constructed over several bituminous and granular layers, whose stiffness tends to decrease with depth [35]. Thus, the load distribution pattern is modified on each layer, see Figure 2.1, and should not lead to excessive stresses in any of the layers to prevent compromising the pavement's structural integrity [36].

Rigid pavements, however, are constructed of a concrete surface, which has a higher elastic modulus than asphalt. Hence, due to the increased material stiffness, traffic loads are distributed over a wider area, and a significant part of the pavement's structural capacity is provided by the concrete slab [34]. Therefore, as opposed to flexible pavements, the bearing capacity of rigid pavements is less influenced by the subgrade characteristics, whereas the structural strength of the concrete is one of the main design parameters [35].

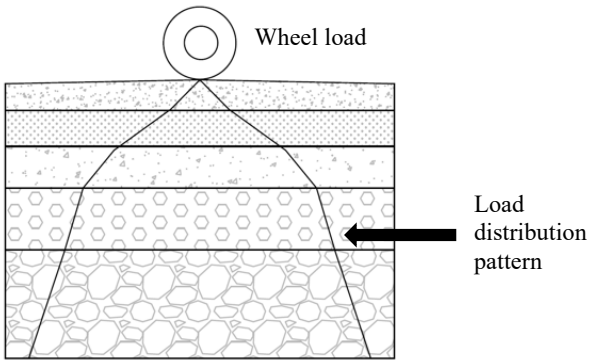


Figure 2.1. Schematic representation of the load distribution pattern in flexible pavements.

2.2.2 Flexible Pavement Layers

In order to decrease the stresses that reach the subgrade, flexible pavements need to have enough structural capacity, which is given by the stiffness and thickness of the different layers [37]. Besides, since the top layers have to withstand higher stress levels compared to the bottom layers, where the load is distributed over a wider area, they are often composed of the highest quality materials [2]. Flexible pavement layers are generally divided into:

- **Surface or wearing course**. It is the top course, typically built of dense graded Hot Mix Asphalt (HMA). In addition to resisting repeated loading and environmental conditions, the surface course must offer a smooth riding surface with proper surface friction, as low roughness is required to provide comfort to users, while also providing adequate skid resistance to ensure road safety. Moreover, this pavement layer prevents the entry of excess water from the surface of the pavement, thereby preventing the soil from being saturated and losing its capability to bear the applied axle loads [[2],[37]].
- **Binder course or basecourse**. It is the layer below the surface course. Its primary function is to contribute to the traffic load distribution to the foundation, as well as ease the construction of the wearing course with an intermediate layer that ensures an even surface [37]. As to the asphalt mixtures used for the binder course, they are composed of larger aggregates

and less binder than the wearing course, resulting in a more economical design [2].

- **Base or roadbase**. Located underneath the binder course, it is a relatively thick course that constitutes the principal support of the pavement structure [37]. This layer can contain Hot Mix Asphalt (HMA) or a Hydraulically Bound Granular Mixture (HBGM) [2].
- **Subbase**. It is the platform upon which the pavement's primary structure is constructed, and therefore it is often regarded as not only part of the pavement but also the foundation [[38],[39]].
- **Subgrade**. Located under the pavement and considered as the main foundation layer, the subgrade consists of soil or borrowed material compacted to the desired density [38]. It might require an improvement layer on the top, known as capping [39].

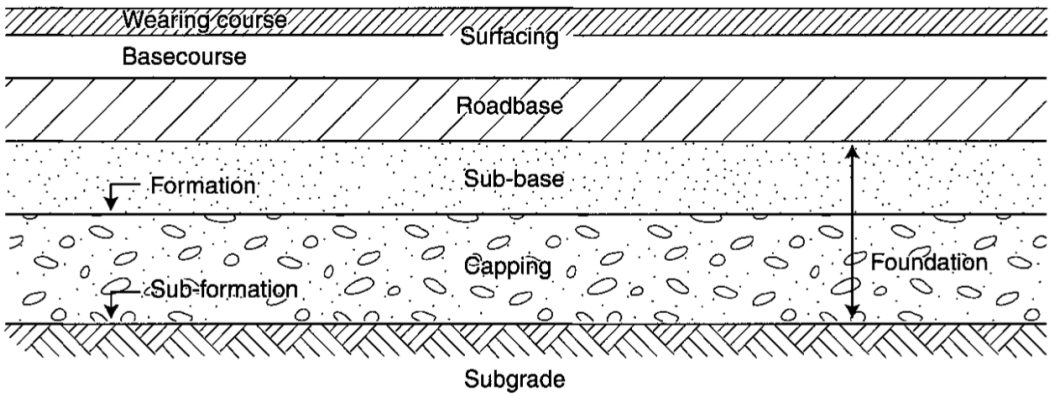
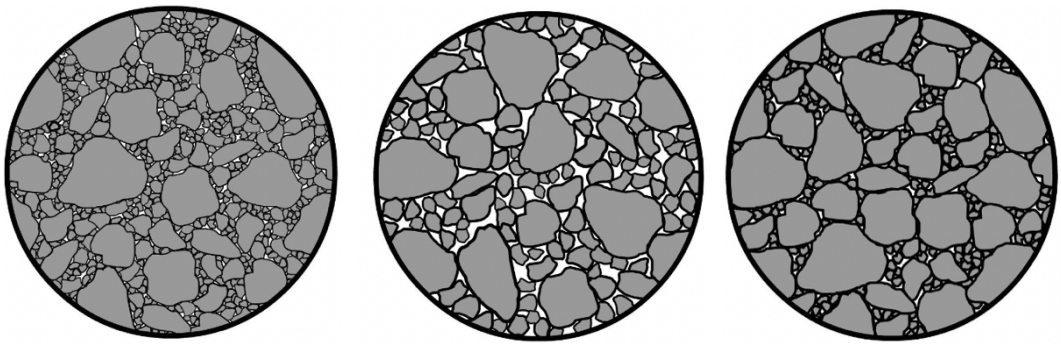


Figure 2.2. Flexible pavement layers, extracted from [40].

2.2.3 Hot Mix Asphalt

This literature review will focus on Hot Mix Asphalt (HMA), which is the most commonly used material for the construction of road pavements in the UK [3]. However, it is noteworthy to mention that Warm Mix Asphalt (WMA) technologies have gained increasing popularity in the UK over the last few years, due to the multiple benefits offered by lowering the production temperatures, such as reducing the risk of premature failure due to early ageing [41].

Typical Hot Mix Asphalt (HMA) mixtures are composed approximately of 95% coarse and fine aggregates by weight, which provide stiffness and resistance to cumulative deformations, and the remaining 5% of modified or unmodified bitumen binder [41]. They can be broadly categorised into dense-graded, open-graded and gap-graded asphalt mixtures [42], see Figure 2.3, and their characteristic properties are determined by the Particle Size Distribution (PSD) envelope and the binder type and content of the mixture [43].



(a) (b) (c)

Figure 2.3. Schematic representation of several asphalt mixtures: (a) Dense-graded, (b) open-graded and, (c) gap-graded. Extracted from [42].

In addition to the mixture design, the properties of the aggregates, which are the largest constituent of asphalt mixtures, substantially affect asphalt's performance [20]. The interactions within the particles, their frictional forces and resistance to cracking are influenced by their geometrical properties, the type of aggregate and the origin [44]. Angular particles and rough textures increase the internal friction, elongated aggregates are more susceptible to cracking, and the aggregate size, which is correlated with the surface area, influences the amount of binder required to coat the particles [45].

2.2.3.1 Dense-graded Asphalt Mixtures

Dense-graded mixtures, also known as well-graded mixtures, are produced with continuously graded aggregates that are uniformly spread across the range of sieves used [46]. These mixtures are commonly referred to as Asphalt Concrete (AC), and

can be used in the surface, binder or base courses [47]. After placement and compaction, dense-graded mixtures have a low air void content, which typically ranges between 4 % and 7 %, preventing the entry of water [48]. Based on the proportion of fine aggregates, well-graded mixtures can be categorised into fine-graded or coarse-graded mixtures, see Figure 2.4 [49].

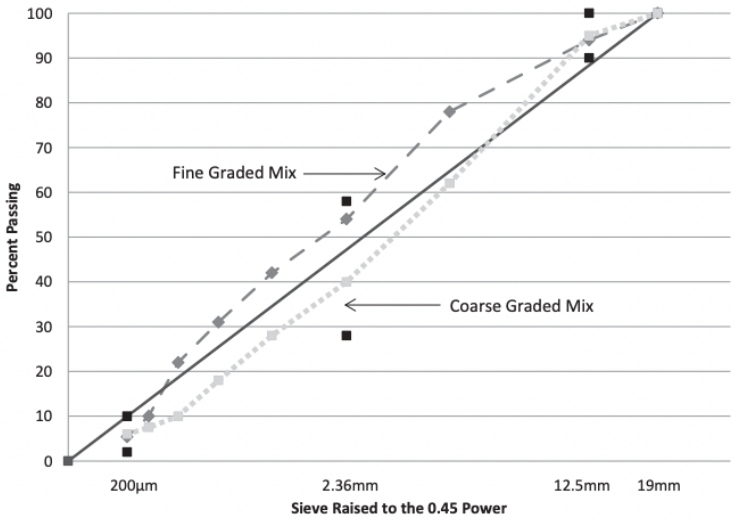


Figure 2.4. Particle Size Distribution (PSD) of dense-graded mixtures (fine-graded and coarse-graded) and maximum density line. Extracted from [47].

2.2.3.2 Open-graded Asphalt Mixtures

Open-graded mixtures are produced by increasing the coarse aggregates and reducing the fines, obtaining a Particle Size Distribution (PSD) curve with an abrupt drop in the intermediate-sized particles [50], as shown in Figure 2.5. These mixtures are characterised by a porous structure with interconnected voids that rely on the stone-on-stone contact, providing noise reduction, permeability, improved friction, and resistance to permanent deformation [51]. However, due to the high air void content, typically greater than 20%, the use of fibres or modified binders is recommended to prevent binder drain-down during placement and compaction [52].

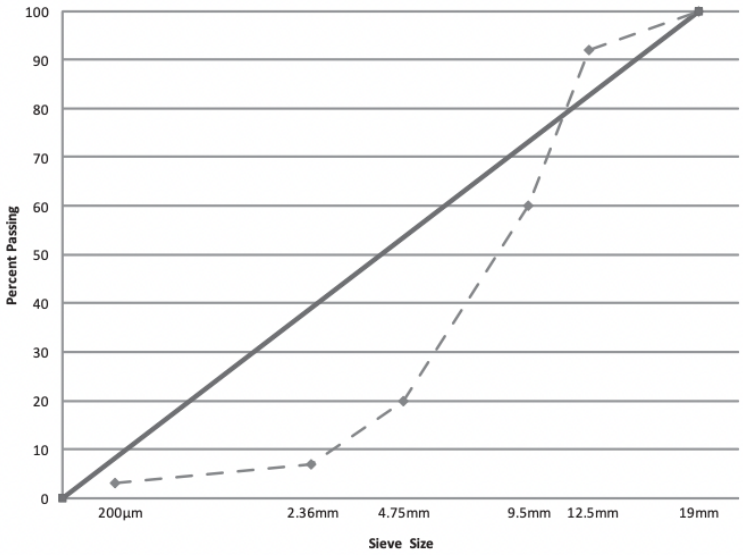


Figure 2.5. PSD of an open-graded mixture and maximum density line. Extracted from [47].

Open-graded mixtures such as Open Graded Friction Courses (OGFC) or Porous Asphalt (PA) are solely used in the surface course [53], while Asphalt Treated Permeable Bases (ATPB) are typically used in conjunction with a sub-drain system to evacuate water below the pavement surface [54]. Thereby, the clogging potential of OGFC or PA should be thoroughly studied when considering the use of open-graded mixtures in the surface course, as the intrusion of fines and dirt into the voids can negatively affect their performance [55].

2.2.3.3 Gap-graded Asphalt Mixtures

Gap-graded asphalt mixtures are produced by intentionally avoiding or reducing intermediate-sized particles, obtaining a Particle Size Distribution (PSD) curve with either a drop (reduced intermediate-sized particles) or a plateau region (absence of intermediate-sized particles) in the intermediate range of sieves [50], see Figure 2.6. One of the most used gap-graded mixtures is Stone Mastic Asphalt (SMA), which is well known for its durability and stability [56]. The high proportion of coarse aggregates ensures an adequate aggregate skeleton structure with stone-on-stone contact, while the mastic formed with the fine aggregates, filler, and binder partially fills the voids, permitting the aggregate interlock [57]. SMA mixtures require higher

binder content than dense-graded mixtures to form a thick coat of mastic around the aggregates, which not only reduces friction between particles but allows them to flow within the mastic. Thus, stabilising agents such as cellulose fibres or polymers are required to prevent bitumen bleeding and draining [58].

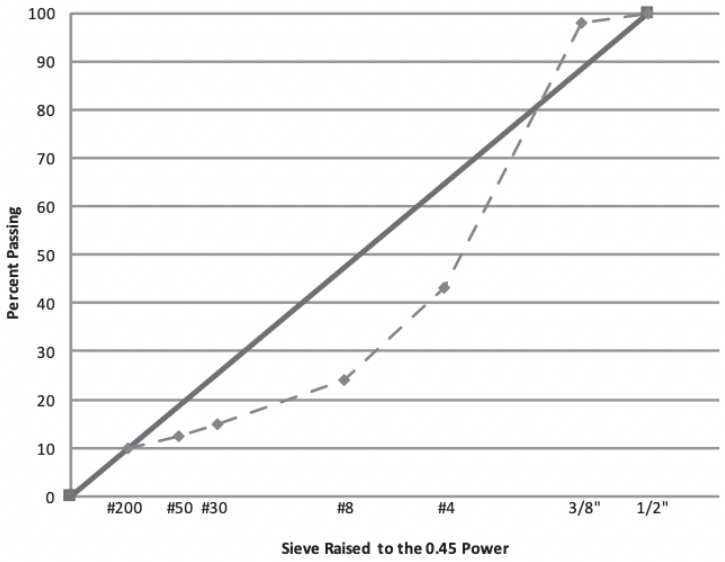


Figure 2.6. PSD of a gap-graded mixture (SMA) and maximum density line. Extracted from [47].

As a result of the increased binder content, aggregate requirements, and the use of additives, SMA mixtures have a higher initial cost when compared to dense graded mixtures, about 20% to 40% more costly [6]. However, this surfacing material can result in a great investment due to its increased lifespan, offering multiple advantages among which the following stand out [4]:

- **Rut resistance and increased durability**, due to the aggregate skeleton that relies on the stone-on-stone contact and the mastic that binds the particles together.
- **Age hardening and fatigue resistance**, resulting from the reduced air void content and a thick film of mastic surrounding the aggregates, which provide permeability and flexibility, and reduce the risk of reflective cracking from the underlying layers as well.

- **Rough surface texture with adequate skid resistance**, that offers surface water drainage and noise reduction. It is noteworthy to mention that in the early service life of SMA, its skid resistance might be affected by the thick film of binder on the surface, that must be worn away by the vehicles.

2.3 Pavement Deterioration

2.3.1 Primary Causes of Pavement Deterioration

There are multiple modes of failure associated with pavement structures, and the main causes of pavement failure can be generally categorized as traffic loading and environmental factors such as temperature, moisture, or frost [7]. However, there are other factors that contribute to pavement deterioration, such as the capacity of the subgrade, which must withstand traffic loading and prevent any excessive flexing that could affect the performance of the upper layers [59]. The construction process can also significantly impact the pavement's performance, as proper compaction is essential not only for achieving the target asphalt density and strength but also for preventing several types of pavement damage [60]. Moreover, even the maintenance plan can compromise the pavement performance if it is not planned or executed properly [61].

2.3.1.1 Traffic Loading

A major consideration when designing and maintaining pavements is the load induced by traffic that a pavement is going to support over its lifespan [62]. This calculation may become quite complex when it comes to mixed traffic and each type of vehicle has different axle loads and repetitions [63]. What is more, the main concern lies in determining the damage caused to the pavement by the diverse axle loads, rather than calculating the loads themselves [64].

To tackle this problem and transform the damage caused by different vehicles into an equivalent number of standard loads, the AASHO developed a traffic feature named Equivalent Standard Axle Load (ESAL) [39]. The ESAL concept makes use of load equivalency factors, known as ESAL factors (ESALF) or Equivalent Axle

Load Factor (EALF) to establish a ratio between the damage on a pavement per pass of a particular axle to the damage per pass of a standard axle used as a reference, which usually consists of an 80 kN single axle with dual tyre [65].

2.3.1.2 Environmental Conditions

Water is one of the greatest important environmental factors that can affect the performance of a pavement. With the presence of moisture in the pavement structure, the adhesion bond between the binder and the aggregate may be weakened in a process named stripping [66], and asphalt cohesion can be reduced as well due to softening, reducing the strength and stiffness of the asphalt layers [67]. There are different ways through which water can break into the pavement structure, such as infiltration through cracks and joints or from the subsoil [68], or because of deficient drainage or the existence of leaking mains, so that water moves to the asphalt layers and saturates them due to capillary action [69].

Another agent that can largely contribute to road damage is frost [70], due to its capability of being expanded by up to 9% on freezing [71], but it is also dependent on other factors, such as the duration and the intensity of the freezing or the fluctuation of temperatures [72]. The main processes that lead to the pavement deterioration are summarised as:

- **Frost heaving**, which is a most common type of frost damage, arises because of the formation of ice lenses when the frost penetrates the pavement and makes it lift of heave [73]
- **Frost shattering**, induced by the expansion of water inside porous stones, which leads to asphalt cracking or the breaking down of aggregates [74]

As to other climatic agents, it is neccesary be mindful of the relationship between the temperature of a pavement and the variation of air temperature, determined by the hour of the day and the season of the year [75], which induces an adjustment of the strength and deformation of the asphalt layers, affecting the functionality and bearing capacity of the pavement [76]. Also, during the construction process, the range of temperatures used should let the binder cover the aggregate and achieve a fluid mix

that can be compacted properly, but excessive temperatures can lead to asphalt binder hardening, causing premature ageing of the binder [77].

2.3.2 Main Types of Damage in Pavements

Numerous publications have presented diverse classifications for the most common types of road defects, which can range from damage to the surface, see Figure 2.7, to a deterioration of the pavement that affects its structural strength [78].

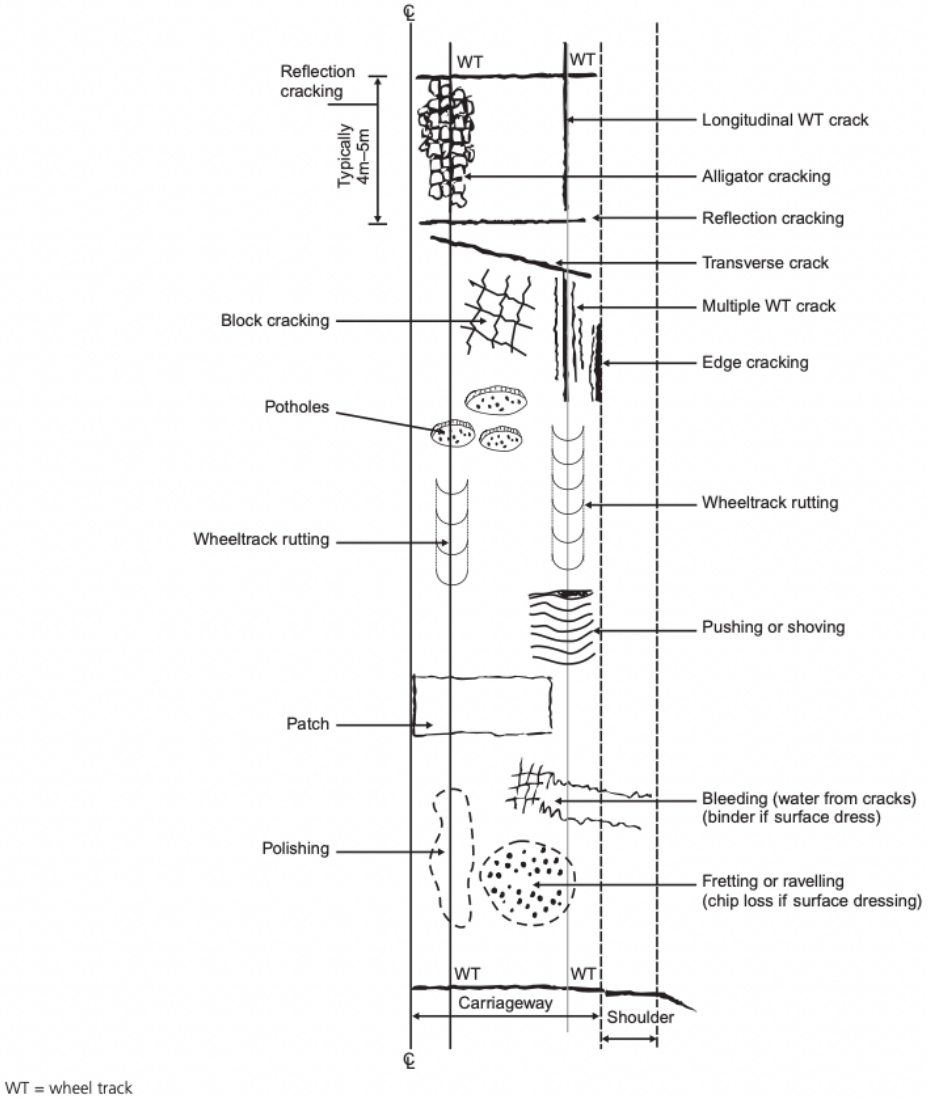


Figure 2.7. Generic distresses commonly found on pavements with asphalt surfacing. Extracted from [32].

This literature review will use the pavement distress classification of the U.S. Federal Highway Administration Manual [79], focusing on visible defects in the surface that can be detected by visual inspection with manual, semi-automatic or automatic surveys [80], and with a particular emphasis on asphalt cracking and ravelling. The assessment of the surface texture will be included as well in this review due to its significant role in road safety [81].

2.3.2.1 Asphalt Cracking

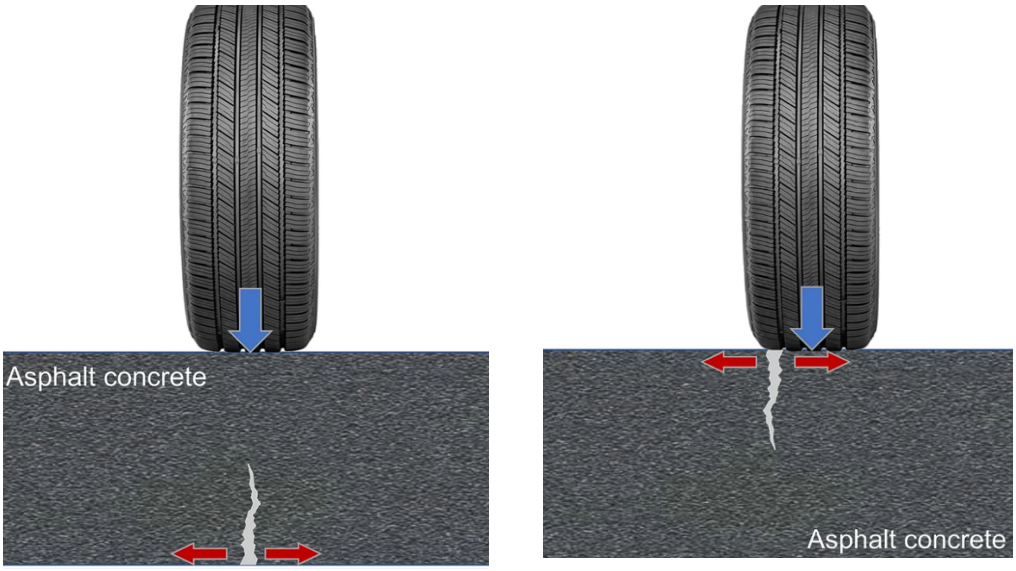
Asphalt cracking is a common distress on thick and mature asphalt pavements. Although there are many factors that can contribute to asphalt cracking, the two most frequent ones are structural issues brought on by repeated traffic loading and thermal stresses associated with the viscoelastic nature of asphalt binders, which become brittle at low temperatures [32]. Oxidative ageing and hardening of the surface can contribute to crack initiation and propagation as well, reducing the pavement's capacity for withstanding the thermal and traffic-induced stresses [[82],[83]].

There are numerous types of cracking, that can be broadly catalogued as follows:

Fatigue cracking

This distress can be manifested as a group of interconnected cracks forming sharp-angled fragments, generating a crocodile pattern. The cracks initially propagate as small longitudinal parallel cracks located in one or both wheel paths, to later create a characteristic crocodile pattern [[35],[79]], that can lead to the disintegration of the pavement surface if the cracks continue growing [36].

Fatigue cracking is regarded as major load-related structural distress [[35],[84]], and has been traditionally associated with the tensile stresses generated at the bottom of the asphalt base, which produce cracks that then propagate to the asphalt surface. Thus, this mechanism is commonly referred to as bottom-up cracking [[80],[82],[84]]. However, another approach has been increasingly studied, based on the propagation of the cracks from the top layer to the base, referred to as top-down cracking (TDC) [[85],[86]], as shown in Figure 2.8.



(a) (b)

Figure 2.8. (a) Bottom-up cracking and, (b) top-down cracking. Extracted from [87].

Extensive research has been conducted on identifying the exact mechanisms responsible for the initiation and propagation of top-down cracking, including both field and laboratory testing campaigns [[82],[85]] and numerical modelling using continuum mechanics [85] and micromechanics [88]. These studies suggest that TDC is induced by the shear and tensile stresses generated at the edge of the tyres, but there is a lack of consensus as to which is the dominant mechanism inducing damage and the mechanism responsible for the damage propagation [[85],[88],[89]].

Although TDC is mainly attributed to fatigue failure, due to the gradual deterioration of the material's properties resulting from cyclic traffic loads that induce stresses below asphalt's strength thresholds [[86],[90]], other factors can contribute to the initiation and propagation of TDC as well. Notable among these are the properties of the asphalt mixtures, such as a high air void content or a weak mastic; construction issues including poor compaction of the mixture, segregation and stiffness gradients within the asphalt courses caused by binder hardening and thermal stresses [[86],[88]].

Longitudinal cracks

This type of asphalt cracking is located parallel to the pavement midline and is generally classified as wheel path or non-wheel path longitudinal cracking [[35],[79]]. Unlike crocodile cracking, longitudinal cracking is often not load-related and has its origins in either a deficient construction of the pavement joints or is caused by frost heaving [35].

Transverse cracks

This type of asphalt cracking is located perpendicular to the pavement midline and presents a regular spacing between the cracks, which are narrow at an early stage and then widen over time [36]. The causes and treatments of transverse cracking are similar to those for longitudinal cracking. In addition, thermal stresses induced by low temperatures can also lead to transverse cracking [35].

Map or Block cracking

Block cracking refers to a group of cracks that create square divisions in the pavement, that can sometimes arise as a result of the crossing between transverse and longitudinal cracks [[36],[79]]. Although traffic loading may affect the severity of block cracking, it is not directly responsible for this distress, which is mainly influenced by the cyclic stresses and strains induced by the daily gradient of temperatures [35].

Reflective cracks

Reflective cracking is a prevalent distress on composite pavements in which an asphalt overlay has been placed over jointed or cracked concrete, but also on pavements with discontinuities that are being covered with an HMA overlay, so that any cracks and joints are reflected in the surface course [35], as shown in Figure 2.9.

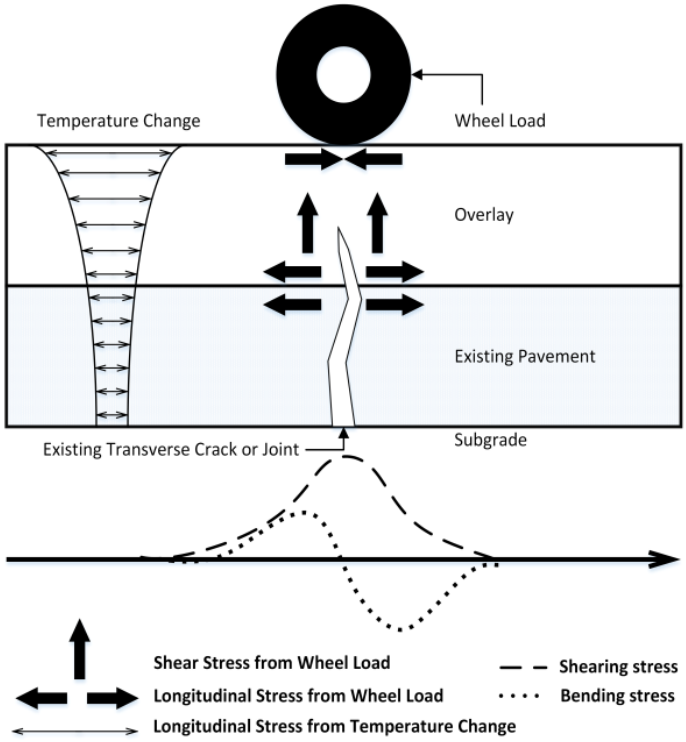


Figure 2.9. Reflective cracking mechanism. Extracted from [91].

Edge cracks

The usual pattern for recognising edge cracking consists of half-moon cracks located at or near the pavement edge of roads without paved shoulders, particularly in curved sections [[35],[84]]. Causes of edge cracking are weak materials or an excess of water in the unpaved shoulders [[36],[79],[84]].

Slippage cracks

Slippage cracking is identified as semicircle cracks with the ends pointing towards the approaching vehicles in the pavement. They emerge from horizontal forces caused by traffic on pavements with a poor binding between the wearing course and the layers underneath [36].

2.3.2.2 Surface Defects

Asphalt Fretting and Ravelling

Fretting and ravelling are two asphalt defects that imply a progressive deterioration of the asphalt surface, requiring maintenance and potentially reducing the pavement's service life [[8],[78]]. Fretting is characterised by the loss of fine material from the wearing course at an early stage, whereas ravelling, which has a high occurrence on thin overlays and high-textured materials, involves a more substantial loss of coarse aggregates [[2],[9],[36]], having as a result a rough surface that is prone to develop potholes [[79],[84]].

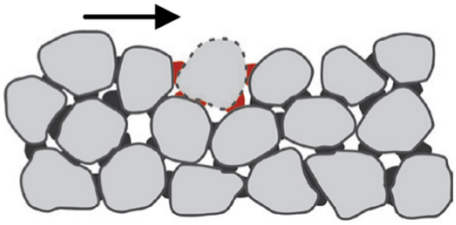


Figure 2.10. Shear stresses generated by the vehicles on the pavement surface. Extracted from [92].

The loss of aggregates is caused by the shear stresses generated by the tyres of vehicles during driving manoeuvres (e.g. braking or accelerating) on asphalt surfaces with a weak bond between the aggregates [92], as represented in Figure 2.10, prompted either by cohesive failure of the binder or adhesive failure in the bitumen-aggregate interface [[93],[94]], as shown in Figure 2.11.



Figure 2.11. Modes of failure in asphalt ravelling: (a) Cohesive damage and, (b) adhesive damage. Extracted from [94].

Diverse factors promote this lack of bonding, including a poor binder content in the mixture and a low compaction grade of the asphalt. However, asphalt ravelling is usually associated with wet weather due to the moisture that affects the bitumen's cohesive strength and adhesive bond in the interface region [95]. Also, traffic loading can induce tensile stresses in the pores saturated with water [96], as seen in Figure 2.12.

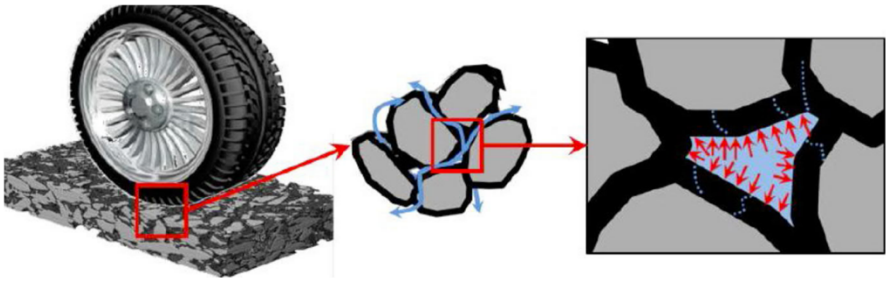


Figure 2.12. Increase of the tensile stress in the asphalt mixture due to the presence of water. Extracted from [96].

The risk of ravelling increases at low temperatures and during short loading periods [95], when the binder has a high stiffness modulus. It is possible that the lack of bond between the aggregates and the binder is caused by the presence of dust in the aggregates, thick enough for the binder to adhere to it instead of the aggregate [32]. There are also some other factors that can induce fretting and ravelling, summarised in Table 2.1, including the chemistry of the surface aggregates and the binder, the rheological characteristics of the binder or the morphological characteristics of the aggregates [[10],[11],[96]].

Lastly, the physical-chemical interaction between the aggregate and the binder can be strengthened by using biobased and chemical additives that promote wetting, improve adhesion, and reduce water susceptibility. They are also known as adhesion agents or anti-strip additives, and among the most used are fatty amines and hydrated lime [[19],[97]].

Table 2.1. Factors that can initiate and/or accelerate ravelling, based on [96].

Category	**Factor**
Presence of water	Permeability
	Surface macrotexture
Materials	Aggregate-binder affinity
	Aggregate cleanliness
Mix design	Air voids
	Binder content
	Binder grade
	Binder type
	Aggregate grading and filler content
Construction quality	Compaction
	Segregation
	Layer thickness
	Asphalt temperature
	Wet weather
	Joints
In situ conditions	Bitumen ageing
	Weather
	Substrate
	Traffic loading

Bleeding

Bleeding is caused by an excess of bituminous binder that, either because of excessive temperatures or due to an incorrect binder dosing, flows to the pavement surface creating patches that are usually located in the wheel paths. In the beginning, it can be manifested as a change of colour in the asphalt, and with time it turns into a loss of texture in the surface due to excess of mastic [[98],[99]].

Polished Aggregates

If the binder of the asphalt surface is eroded due to traffic loading, the aggregate is revealed, and it can lead to a loss of skidding resistance. The rate of polishing of the aggregates varies, and it is expressed as the Polished Stone Value (PSV), which is an index that compares the resistance to the polishing of an aggregate to a standard [[32],[36],[79]].

2.3.2.3 Surface Deformations

Rutting

Rutting is a permanent deformation located in the wheel path and arises from periodic traffic loads that generate cumulative plastic deformations. This asphalt distress is characterised by a longitudinal surface bowl, and it might have associated transverse displacements as well. Asphalt rutting can be broadly categorised into [[100],[101],[102],[103]]:

- **Instability rutting,** which is the most typical form of rutting, and involves different deformation modes: At an early development stage, the material densification that characterises the cumulative longitudinal deformation; and at an advanced stage, the transversal displacement controlled by shear-related deformations. Instability rutting is associated with the material performance, and more specifically to an incorrect design of an asphalt mixture subjected to heavy traffic and/or high temperatures. Hence, polymer-modified bituminous binders are frequently used to design rut-resistant asphalt mixtures, due to their higher softening point.
- **Structural rutting when** the deformation of the subgrade is reflected to the asphalt pavement. The structural capacity of the subgrade may be affected by an insufficient thickness to bear traffic loads, or by the presence of water, among other factors.

The most suitable measurement of the rutting profile is mean rut rate, however, this measurement does not provide enough information to determine the type of rutting [104].

Shoving

Shoving consists of longitudinal or transversal displacements in a reduced section of the pavement, usually located in areas of vehicle manoeuvring subjected to shear stresses, such as curves, hills, or intersections. The causes for shoving are similar to those of instability rutting [[78],[79]].

2.3.2.4 Potholes and Patching

Asphalt potholes are localised bowl-shaped distresses in the pavement surface, frequently generated as a result of the expansion of surface cracks that break the pavement in conjunction with the presence of water, which accelerates the pavement degradation and hence the severity of the pothole [105]. Patching is one of the most common maintenance treatments for potholes and some types of surface cracking, using hot mix asphalt or cold mixtures. The material and technique selection for patching is key to ensure the effectiveness of the repair [106].

2.3.2.5 Evaluation of the Surface Texture

Skid Resistance

Skid resistance is a measurement of the way the surface of the pavement can contribute to the friction developed between the road and the tyres of a vehicle when a driver performs manoeuvres such as spinning or accelerating and decelerating [[107],[108]]. The mechanisms that generate this friction, which are adhesion and hysteresis, depend to a great extent on the pavement microtexture in dry conditions, and the pavement macrotexture in wet conditions, see Figure 2.13 [[109],[110]]. In a road section, this parameter does not have a constant value due to the degradation caused by the traffic, but also due to the seasonal fluctuations [[111],[112]].

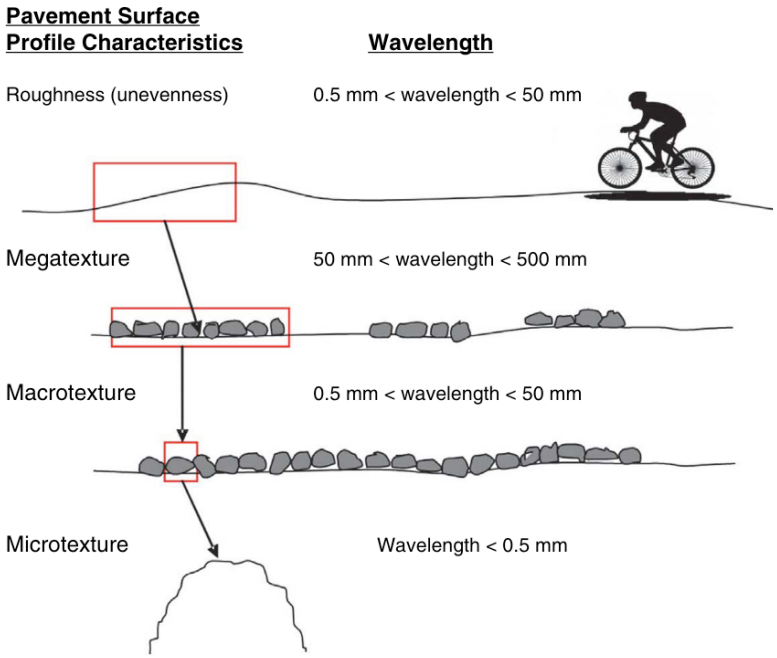


Figure 2.13. Pavement texture and wavelength. Extracted from [113].

Roughness

In order to provide skid resistance, it is essential to have a surface with texture, but it can also affect users' comfort and cause premature ageing of the pavement and tyres, as well as accelerating fatigue damage on the roads as a result of increased dynamic traffic loads [114]. Roughness is the characterization of the surface irregularity, see Figure 2.13, also defined as the vertical deviations of the pavement surface from an ideal reference plane [115].

The World Bank sponsored several research programs in the late 1970's to establish a common quantitative basis for comparing roughness measurements, which led to the development of the International Roughness Index (IRI) [116]. It consists of a roughness scale based on the response of a common vehicle to road surface roughness [117]. To calculate it, the profile of the road must be processed through software that simulates how the suspension of a common vehicle would react to roughness details [118].

2.4 Asphalt Self-Healing

2.4.1 Self-Healing Mechanism

2.4.1.1 Asphalt Ageing and Self-Healing Properties

Asphalt ageing is a complex phenomenon that involves a change in the rheological properties of the material caused by a modification in the chemical composition of the binder. There are different forms of ageing, among which hardening, volatilization and oxidation can be highlighted, and it can occur either while the asphalt mixture is produced, due to excessively high temperatures, or during its service life, caused by diverse environmental effects [119].

Due to ageing, the stiffness modulus of the binder increases, and the bitumen becomes more brittle, resulting in an asphalt with less relaxation capacity. This ageing process can be affected by extrinsic agents such as UV radiations [120], traffic, or weather conditions [121], but also by intrinsic factors such as the bitumen type and air void content [119]. As a result, asphalt ageing leads to the development of microcracks that will grow, and ultimately cause the failure of the pavement [122].

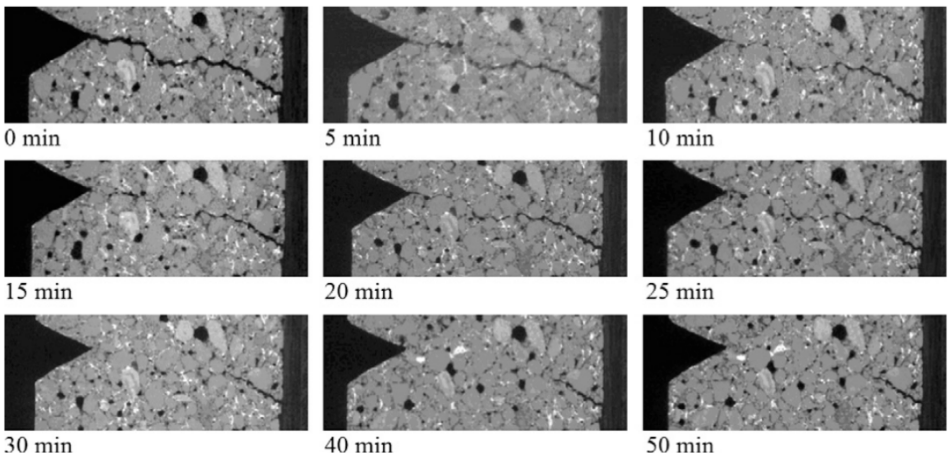


Figure 2.14. CT scans of the self-healing process of a beam made of SMA. Extracted from [123].

However, asphalt concrete is also known for its healing capacity [124], which is described as the ability of the bitumen-bound materials to recover part of the initial strength and stiffness [125], thereby decelerating the microcrack damage [126], as shown in Figure 2.14. This phenomenon is vastly influenced by high temperatures and the resting time between applied loads [125], albeit other agents must be considered as well: External factors such as traffic loading and the damage level, and internal factors including the surface energy of the material and the interdiffusion capacity of its molecules [123].

While these variables are difficult to control and asphalt's self-healing effect on retarding damage is limited, research has been conducted to investigate treatments that can trigger this self-healing capacity, including induction heating, nanoparticles, and embedded rejuvenators [126].

2.4.1.2 Functioning Principle of the Encapsulated Rejuvenators

The binder components can be broadly catalogued into two chemical groups: asphaltenes and maltenes. Asphaltenes are an insoluble component with a high polarity that constitutes the solid part, while maltenes are a soluble group constituted by saturates, aromatics and resins [[127],[128]]. Throughout the ageing process, and more specifically oxidative ageing, the fractions of saturates, aromatics, resins and asphaltenes (SARA) are altered and the ratio of asphaltenes to maltenes increases [95], as seen in Figure 2.15, inducing an increase in the binder viscosity as well, which results in a harder and more brittle material [129].

Thus, asphalt rejuvenators were developed as a product that aimed to restore the original ratio of asphaltenes and maltenes in the mixture, reconstituting the chemical composition of the asphalt by using highly aromatic oils that contain an elevated proportion of maltene components [130]. However, the main drawback of this type of treatment, which is applied to the asphalt surface at an early stage, is that it must penetrate the asphalt layers for the rejuvenators to be effective, which is almost never completely achieved [131]. Hence, the application of rejuvenators on the pavement surface can lead to a loss of skid resistance. Moreover, for the rejuvenators to be

effective, some resting time is needed after the application, leading to traffic disruptions due to road closures [26].

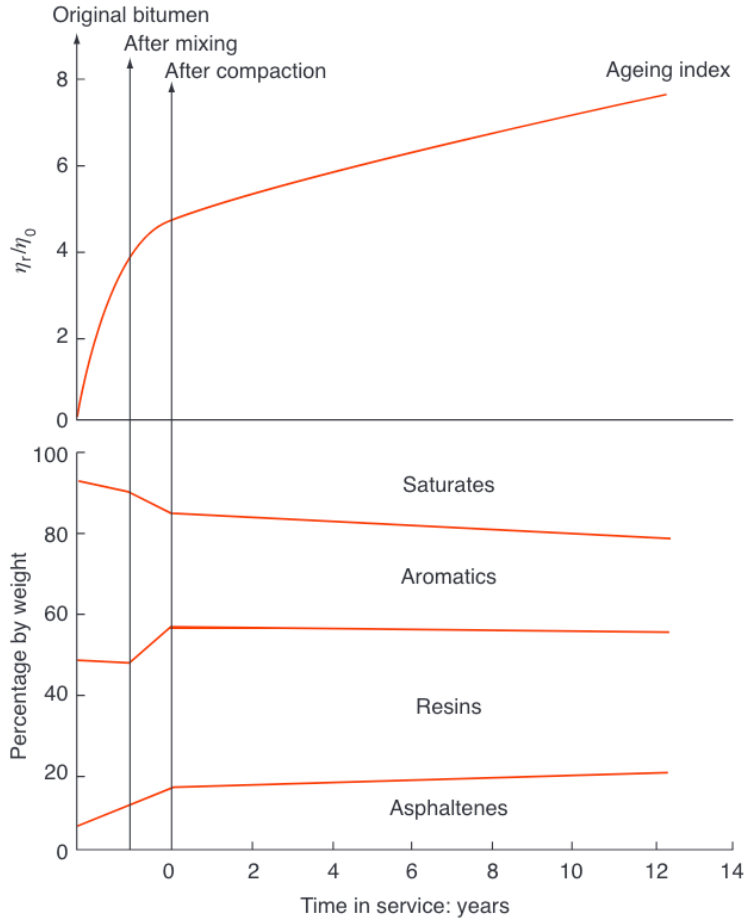


Figure 2.15. Changes in the SARA fractions over time due to oxidative ageing. Extracted from [95].

Another approach for enhancing asphalt's self-healing characteristics is by using encapsulated rejuvenators. The capsules containing the rejuvenator agents are added to the asphalt during the mixing process, therefore they must resist the stresses and high temperatures induced by the mixing and compaction processes. Then, the encapsulated rejuvenator is progressively released in response to external stimuli, enhancing the bitumen flow to delay or mitigate asphalt cracking [26]. This mechanism is shown in Figure 2.16, and requires a mechanical loading to activate the capsules, chemical interactions to restore the binder's composition and binder flow in a porous medium to seal the cracks with the restored binder. The crack healing process can be explained by a three-stage model that includes: (i) Closure of

macrocracks by cause of the consolidation stresses and flow, (ii) closure of microcracks and cohesion enhancement through wetting and, (iii) restoration of mechanical properties due to diffusion [27].

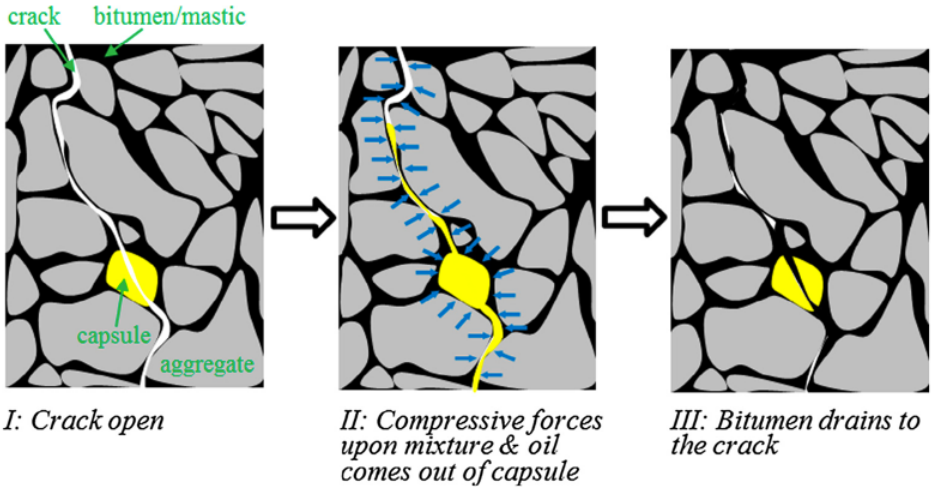


Figure 2.16. Representation of asphalt crack healing using encapsulated rejuvenators. Extracted from [26].

2.4.2 Manufacturing of Encapsulated Rejuvenators

2.4.2.1 Asphalt Rejuvenators Used

The application of asphalt rejuvenators, whether through spraying or encapsulation methods, has received significant attention within the research community due to their potential for extending the lifespan of the pavements [24]. Diverse types of rejuvenators have been evaluated over time and one of the key findings from these studies is that, although there is still some lack of knowledge as to the exact rejuvenation mechanism, the effectiveness of the rejuvenator appears to be mainly determined by its type and origin [132]. Table 2.2 provides a summary of some of the most researched rejuvenators, classified by their origin into vegetable oils, petroleum-based rejuvenators, by-products from the industry, waste oils and bio-oils derived from agricultural and animal waste.

Table 2.2. Asphalt rejuvenators classification and examples, based on [24] and [132].

Category	Rejuvenator
Vegetable oils or organic rejuvenators	Soybean oil
	Corn oil
	Rapeseed oil
	Sunflower oil
	Pongamia oil
	Castor oil
Petroleum-based rejuvenators obtained from crude oil distillation	Aromatic extract
	Paraffinic oil
	Naphthenic oil
	Fuel oil
By-products from industry	Tall oil
	Coke oven gas condensate
	Cotton seed oil
Waste oils	Waste Engine Oil (WEO)
	Recycled Engine Oil bottoms
	Waste Cooking Oil (WCO)
Bio-oils derived from agricultural products and wastes, or animal wastes	Bio-oil from wood waste
	Bio-oil from sawdust
	Bio-oil from swine manure
	Bio-oil from algae

It has been reported that vegetable oils and waste cooking oils outperformed petroleum-based and waste engine oils when studying their effect on the rheological properties of the binder [[28],[133],[134]]. Organic rejuvenators are not only rich in fatty acids but also, require a lower dosage, have enhanced temperature resistance and, waste vegetable oils may offer greater environmental sustainability.

If the rejuvenator is encapsulated, one of the main challenges to overcome is achieving a stable emulsion that ensures an efficient encapsulation [135]. To date, several types of rejuvenators have been successfully encapsulated, which include virgin cooking oils [[30],[136]], bio-oils [137] and waste oils [[138],[139]]. Moreover, virgin sunflower oil yielded the best performance among the encapsulated rejuvenators, not only meeting the stability criteria for ensuring an effective encapsulation but also showing the greatest thermal stability when subjected to asphalt's manufacturing temperatures [140]. Furthermore, although the

abovementioned rejuvenators proved to help restore the chemical composition of aged binder, sunflower oil showed the greatest rejuvenation effect [135].

2.4.2.2 Materials and Methods for the Encapsulation Process

Encapsulation is a process that has been used in many different industries, such as the food industry or pharmaceuticals, to coat or entrap one material within another material or system [141]. The most common encapsulation methods can be broadly categorised into the following [142]:

- **Physical methods**, in which mechanical actions or physical processes are used to encapsulate. Pan coating and spray drying are among the most popular physical encapsulation methods, and extrusion-based techniques are worth mentioning as well
- **Chemical methods** rely on chemical interactions that lead to the polymerisation (interfacial or in situ) of the encapsulating material
- **Physico-chemical methods** combine the use of physical methods with pre-formed polymers and include techniques such as ionic gelation and coacervation

Before reviewing the techniques used for the encapsulation of rejuvenators to enhance asphalt's self-healing properties, it is important to consider the classification of the encapsulated rejuvenators based on their size (microcapsules with an average diameter of less than 100 μm or capsules over 100 μm diameter [31]), and morphology (core-shell, multi-cavity or fibre-shaped encapsulated rejuvenators [29]). Figure 2.17 includes a schematic representation of the aforementioned morphologies and sub-categories of encapsulated rejuvenators.

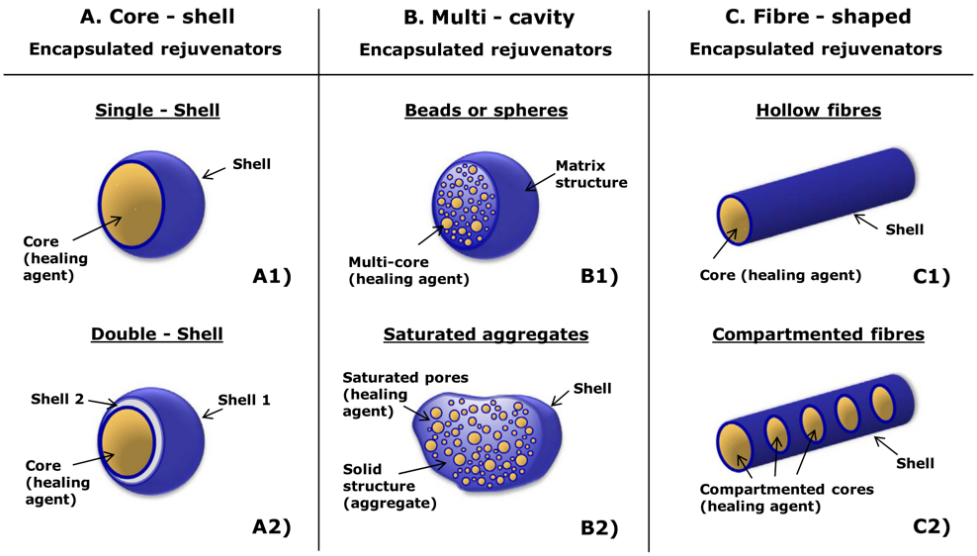


Figure 2.17. Morphologies evaluated for encapsulated asphalt rejuvenators. Extracted from [29].

Numerous efforts have been undertaken to successfully encapsulate asphalt rejuvenators that do not only withstand the temperatures and forces involved in the mixing process but also ensure a progressive and controlled release of the rejuvenator agent. The first generation of encapsulated asphalt rejuvenators were Saturated Porous Aggregates (SPAs), as shown in Figure 2.18(a) using a physical-chemical method reliant on vacuum saturating the porous medium [26]. Based on the classification from Figure 2.17(B2), the encapsulator provides a solid multi-cavity structure made of calcium-silicate aggregates, which is covered by a shell made of an epoxy–bound cement. This type of encapsulated rejuvenator was manufactured in a range of 1 to 7 mm diameter approximately [[143],[144],[145]].

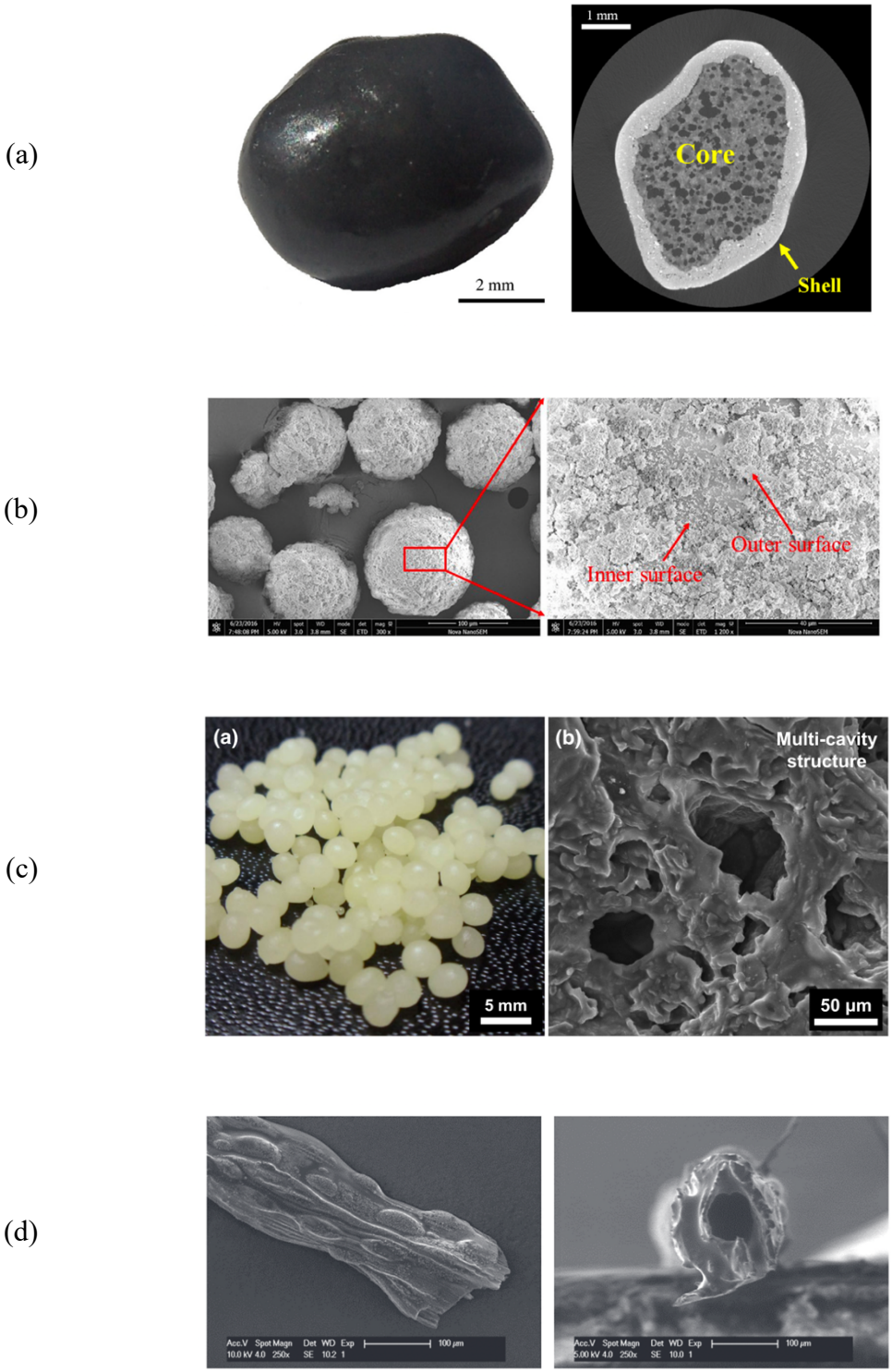


Figure 2.18. Different morphologies of encapsulated rejuvenators: (a) Saturated aggregates [143], (b) double-shell core microcapsules [146], (c) polymeric spheres [147] and, (d) compartmented fibres[148].

The succeeding set of encapsulated rejuvenators was manufactured with a core-shell morphology, either single or double shell, see Figure 2.17(A1 & A2). However, this technique yielded microcapsules with an average diameter ranging between 5 and 55 μm, primarily tested in bituminous binders rather than asphalt mixtures [29]. Single-shell microcapsules were synthesised by in-situ polymerisation, using a Melamine-Urea-Formaldehyde (MUF) copolymer for the shell [[146],[149]]. In contrast, double-shell microcapsules were produced by a combination of in-situ polymerisation (chemical) and two-step coacervation (physico-chemical), using a Melamine–Formaldehyde modified by Methanol (MMF) commercial prepolymer [[150],[151],[152]].

There were several attempts to use fibre-shaped encapsulated rejuvenators as well, see Figure 2.18(d), as porous aggregates were reported to affect asphalt's stability, and the chemical substances used for the microencapsulation, when used in large quantities, might present an environmental hazard [148]. Besides, the use of fibres instead of capsules offers several advantages, facilitating the release of the rejuvenator in cracked areas due to the vascular network they create. The main drawback, however, is the difficulty of properly distributing the fibres during asphalt manufacturing [153]

Compartmented fibres, see Figure 2.17(C2), were manufactured either by wet-spinning (physico-chemical) [154], or using a microfluid device in combination with ionic gelation (physico-chemical) [155], yielding compartmented fibres with average diameters ranging between 170 and 500 μm [29]. Hollow fibres containing rejuvenators were manufactured as well, using the same techniques as for compartmented fibres, within the same size range [156].

However, among the manufacturing techniques, the external gelation of sodium alginate in the presence of calcium emerged as the most prevalent, see Figure 2.19(c). Moreover, the polymeric encapsulated rejuvenators manufactured with this physico-chemical method, see Figure 2.17(B1), remain the subject of ongoing research for enhancing asphalt self-healing capabilities [29].

This technique requires preparing a stable emulsion of water, sodium alginate ($C_6H_7O_6Na$), and the selected rejuvenator, which in much of the research conducted is sunflower oil, as mentioned in Section 2.4.2.1. Then, this emulsion is dripped through dropping funnels or pressure pumps into a solution of water and calcium chloride ($CaCl_2$), as shown in Figure 2.19, which makes the droplets of emulsion react due to the diffusion of calcium ions in the emulsion, boosting the cross-linking of the sodium alginate. Lastly, the capsules are decanted, washed, and dried [135]. The use of an epoxy-bounded cement shell for this type of capsule was evaluated in the early stages of research and later discarded, as the capsules demonstrated the ability to withstand asphalt mixing and compaction effectively [157].

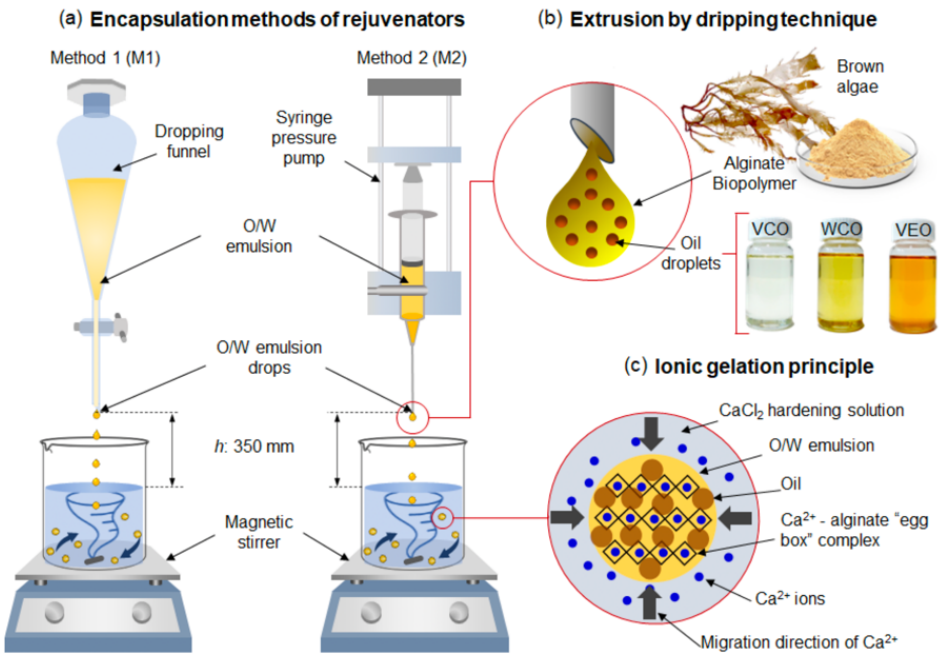


Figure 2.19. Manufacturing of encapsulated rejuvenators by external gelation of sodium alginate in the presence of calcium using a dripping technique. Extracted from [140].

Sodium alginate has been extensively used for the encapsulation of asphalt rejuvenators due to its non-toxic, biodegradable, and stable properties, as well as its low environmental impact [140]. In addition, the polymeric matrix provides more structural strength when compared to core-shell capsules, which is convenient for resisting asphalt manufacturing but also for ensuring a progressive release of the rejuvenator, promoting long-term healing [158]. Calcium-alginate capsules containing sunflower oil as the rejuvenator agent have been manufactured in a range

of 1.3 to 7 mm [29]. This type of encapsulated rejuvenator was fine-tuned in laboratory-based studies, evaluating the optimum capsule size and compressive force to maximise asphalt self-healing [30]. Based on these studies, encapsulated rejuvenators should resist an average compressive force of about 10 N [159] and have an approximate size of 1.4 mm for optimal self-healing of Stone Mastic Asphalt.

2.4.3 Characterization of Encapsulated Rejuvenators

Capsules must be characterised after manufacturing to assess their properties and verify their suitability for the intended purposes. Gray classified in [160] the methods for characterising the capsules according to their physico-chemical, structural, and mechanical characteristics. This review will be limited to the assessment of calcium alginate capsules containing sunflower oil for asphalt self-healing purposes, using the classification provided in Table 2.3 as a framework. It will not, however, be exclusive to this classification.

Table 2.3. Classification of the methodologies used to characterise capsules, based on [160].

Physicochemical properties			
Size and distribution	**Surface roughness and morphology**	**Chemical composition**	**Surface charge and zeta potential**
Dynamic Light Scattering (DLS) Laser diffraction Scanning Electron Microscopy (SEM)	Atomic Force Microscopy (AMF)	Attenuated Total Reflectance Fourier-Transform Infrared (ATR-FTIR) spectroscopy	Streaming potential technique Electrophoresis
Structural properties			
Shell thickness	**Pore size**	**Crystallinity**	**Release of core material**
Scanning Electron Microscopy (SEM) Transmission Electron Microscopy (TEM) Focused Ion Beam (FIB)	Computer Tomography (CT) scan	X-Ray Diffraction (XRD) Differential scanning calorimetry (DSC) Thermo-gravimetrical analysis (TGA)	Application of loads
Mechanical properties			
Anatomic Force Microscopy (AFM)		Compression testing using a cylindrical probe	

2.4.3.1 Particle Size

In the majority of the research studies, the particle size was determined from individual measurements using an optical microscope, measuring the average diameter from a sample set, or by processing photographs taken from the microscope to analyse the particle size and shape descriptors [[135],[140],[144],[157],[161]]. Polarised light microscopes were used as well embedding the capsules in an epoxy resin and polishing the sample for optimal results [162]. Lastly, electronic callipers were also used to determine the dimensions of the capsules in the three axes but, due to their reduced size, the measurements might lack accuracy with this method [30]. The average size of the studied capsules ranged from 7 (mm) to 1.3 mm [138], however, their size was later optimised based on the studied asphalt mixtures.

2.4.3.2 Particle Density

The volume and density of the capsules were evaluated using a Gas Pycnometer [25]. In several studies, these measurements were taken at different temperatures to simulate the gradient of temperatures to which the capsules are exposed during asphalt manufacturing. It was found that the capsule density had a slight decrease when capsules were exposed to 140 ^{o}C and 160 ^{o}C [[163],[164]], simulating asphalt manufacturing temperature conditions.

2.4.3.3 Inner Structure

Scanning Electron Microscopy (SEM) was employed as well by researchers to evaluate the inner morphology of the capsules, as this technique can reveal the multiple cavities generated by the ionic gelation of sodium alginate, as illustrated in Figure 2.18(c). The assessment focused on the inner morphology and pore size, but also SEM images from the outer structure were extracted [30]. The capsules were either: (i) embedded in an epoxy resin and then polished to expose their inner structure [157] or, (ii) directly cut and coated with gold powder to enhance electrical conductivity [158]. SEM images have been widely used in diverse studies, including [[25],[135],[147],[159],[161],[165],]. Another imaging technique used in prior

research to evaluate the multi-cavity structure of the capsules is through X-ray Computer Tomography (CT) scans [[30],[159],[162]].

2.4.3.4 Distribution within the Asphalt

The full potential of CT scans was unlocked in [[143],[147],[157],[164]], to evaluate the distribution and integrity of the capsules in asphalt samples. After the CT-scan acquisition, 2D images of the cross-sectional area were reconstructed and stacked to create a 3D visualization. Then, the capsules were isolated to be studied separately through material segmentation [163], as shown in Figure 2.20.

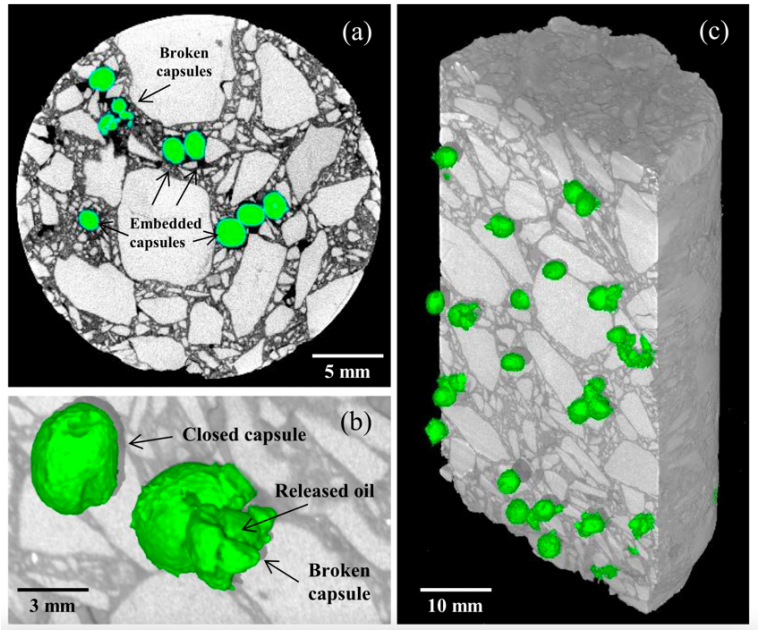


Figure 2.20. Reconstruction from CT scans of a sample containing capsules: (a) cross-sectional area of the samples, (b) detailed 3D visualisation of the capsules and, (c) 3D reconstruction of the sample. Extracted from [163].

2.4.3.5 Mechanical Properties

The mechanical strength of the capsules was determined by uniaxial compression testing until failure using a Universal Testing Machine (UTM) with parallel plates [[157],[165]], although in some studies specific equipment adapted to the micro-scale was used, such as a Micro Tensile Strength Testing Machine (TSTM) [[162],[163]]. This test was conducted to characterise the mechanical properties of the capsules and evaluate whether they would break during asphalt mixing and compaction, based on

the approximate required strength defined by [144] to prevent the capsules from breaking. Moreover, the compressive strength of the capsules was measured as well to evaluate the effect of the capsule size, emulsion proportions and testing temperature on the mechanical properties of the capsules. It was determined that at higher temperatures, the stiffness of the capsules decreased [[25],[30],[135],[164]] and the test results had a higher variability [25]. The strength of the capsules increased with the diameter [30], and decreased with the oil-to-water ratio [25].

2.4.3.6 Chemical Composition

After the image reconstruction from the raw data obtained from CT-scanning capsules, the volumes of calcium alginate and sunflower oil were estimated in [162], based on the grey-level histograms. In [30], SEM was used in conjunction with Dispersive X-ray Spectroscopy (EDS or EDX) to perform elemental mapping. The distribution of sodium and chloride elements indicated the formation of sodium chloride salts, which was then confirmed through Inductively Coupled Plasma Optical Emission Spectroscopy (ICP-OES), reinforcing the theory that the ion exchange during the capsule manufacturing stops after reaching an equilibrium.

2.4.3.7 Thermal Stability

Numerous studies evaluated the thermal stability of sodium-alginate capsules through Thermogravimetric Analysis (TGA), including [[31],[157],[158],[164],[165]] among others. These research studies concluded that within the asphalt production range of temperatures (up to 200 ^{o}C), as shown in Figure 2.21(a), the capsules experienced a minimal mass loss, of about 4% or lower, depending on the formulation of the capsule. Moreover, this mass loss was attributed to water evaporation and polymer degradation.

The thermal expansion of the capsules was evaluated as well in [[163],[164]] using a Thermomechanical Analyser (TMA). Although the changes in volume were not significant up to 170 ^{o}C (approximate asphalt manufacturing temperature), as presented in Figure 2.21(b), the reduction in the density of the capsules observed in

Section 2.4.3.2 in the range of 140 ºC to 160 ºC might be attributed to the increase of volume.

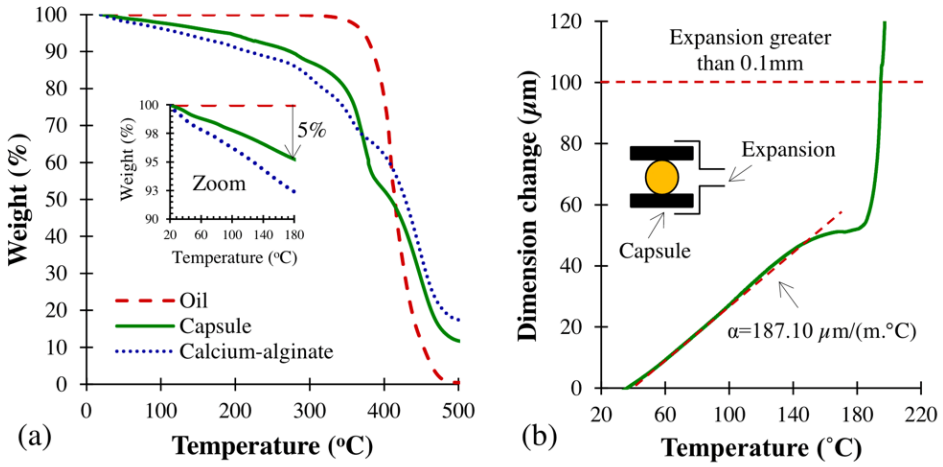


Figure 2.21. Evaluation of the thermal and volumetric stability of sodium alginate capsules containing sunflower oil: (a) TGA results and, (b) TMA results. Extracted from [164].

2.4.4 Evaluation of Asphalt Containing Encapsuled Rejuvenators

Although there has been considerable research conducted on the evaluation of the self-healing capacity of bituminous binders [[135],[140]] and asphalt mastic [[25],[162]] containing encapsulated rejuvenators, this literature review will exclusively focus on the evaluation of asphalt samples containing calcium alginate capsules with encapsulated sunflower oil.

Previous studies characterised the physical and mechanical properties of asphalt samples containing capsules and evaluated asphalt's self-healing to determine the optimal capsule dosage, size, and characteristics that maximised asphalt's self-healing capabilities without compromising its overall performance, as well as the required resting time for the oil to diffuse and promote the binder flow. Some other studies, such as [163], focused on evaluating asphalt's manufacturing process to determine the optimum procedure to add the capsules. It was concluded that the capsules do not require any pre-heating and the author's recommendation was to add the capsules at the end of the mixing process. Later research [147] verified as well through CT scans that the capsules can resist both mixing and compaction.

2.4.4.1 Conventional Test Methods

In early research, cyclic uniaxial compression of unconfined samples was used to compare the effect of different types of capsules and the resting time required for the oil to act on dense asphalt mixtures [[157],[161]]. Samples were subjected to a certain number of cycles, the test was stopped and then, after a resting time, cyclic loading restarted until completing the testing. Results showed that samples required a minimum resting time of 24 to 48 hours for the oil to diffuse and repair part of the damage. Compared to samples without capsules, samples containing capsules showed a higher increase in their stiffness after this resting period, but a reduced deformation resistance.

The risk of rehydration of the capsules [166] and its potential impact on asphalt's performance was studied in [[167],[168]] with the Indirect Tensile Strength (ITS) test on dry and wet samples. This testing campaign showed that moisture damage on dense asphalt and SMA containing capsules did not influence ITS results. The Indirect Tensile Strength was evaluated as well in [147], on samples containing different percentages of capsules. It was observed that the increase in ITS on samples containing 0.5% capsules might be related to the decrease in asphalt's air void content. As to asphalt's physical properties, changes in the air void content due to the presence of capsules variated on different types of asphalt based on the capsule size and dosage [[147],[163],[167],[168]].

Indirect Tensile testing was also employed to calculate the Indirect Tensile Stiffness Modulus (ITSM) and the number of cycles until failure on AC 20 base 40/60 [167] and SMA 14 surf 40/60 [168] samples containing 0.5% of capsules. In [167], the stiffness modulus and number of cycles until failure were lower on asphalt with capsules, which was attributed to the capsule size (2.9 mm) and the test conditions, which made the capsules act as soft aggregates under high temperatures. Hence, the authors recommended reducing their size and, in later research [168], the size of the capsules was adjusted to the asphalt mixture, obtaining equivalent stiffness and fatigue life in samples with and without capsules.

Moreover, several studies included in their experimental program additional testing. For instance, the release of oil from the capsules was evaluated using Fourier Transform Infrared spectroscopy (FTIR) on samples of bitumen extracted at different stages of asphalt manufacturing and testing [[135],[140],[147],[157],[168],]. The Cantabro test was performed on dense asphalt mixtures, reporting a reduction in particle loss on samples containing 0.1 to 0.5% of capsules [167], while in [147] the addition of 0.5% of capsules had no impact on the particle loss and higher percentages resulted in higher mass loss. In [[159],[168]], the dynamic pendulum test was used to determine whether the use of capsules on SMA surface mixtures could affect their skid resistance, and results showed the measurements were not affected by the addition of capsules.

2.4.4.2 Test Methods Designed to Evaluate Crack Healing

In [167], a new test method was developed to quantify the effect of the capsules on asphalt self-healing capabilities, using the three-point bending test (3-PB) to evaluate the strength recovery of samples with induced damage. This new methodology, which was replicated in later research studies, is divided into three steps, as presented in Figure 2.22:

- **Step A:** Crack generation in asphalt samples, by means of 3-PB testing. Sample preparation includes cutting a notch in the middle of the bottom face and conditioning the specimen at -20 ºC to facilitate the generation of a crack at the midpoint.
- **Step B:** Capsule activation by simulating traffic conditions. After cracking, both halves of the sample are confined in a mould and a compressive load is applied to release the rejuvenator from the capsules. A plastic membrane separates both halves during compression testing, to prevent any crack-healing due to the confinement pressure.
- **Step C:** Asphalt crack healing. After the compressive load is applied, the membrane is removed, and samples are stored for a certain resting period in temperature-controlled rooms, to let the oil diffuse and make the bitumen flow, boosting asphalt crack-healing. Then, step A is repeated.

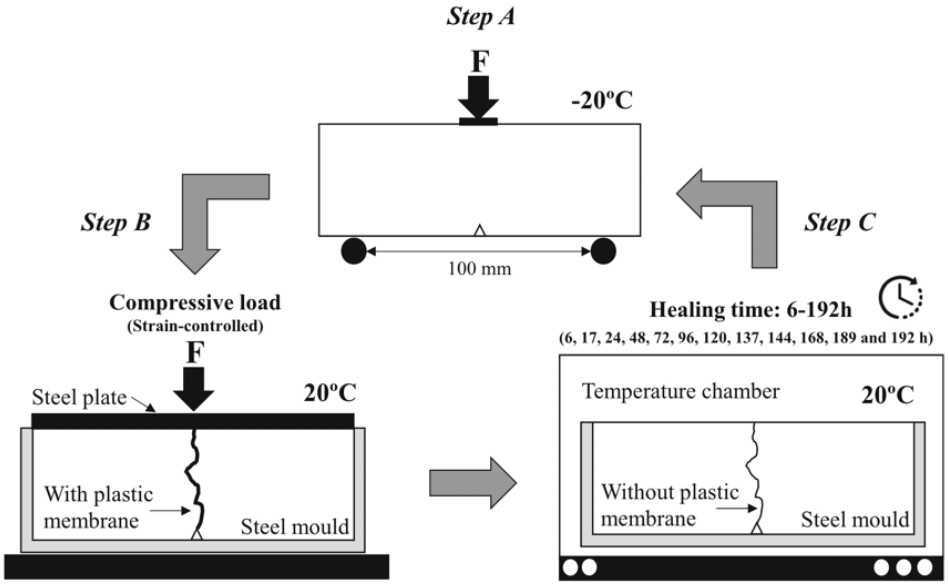


Figure 2.22. Schematic representation of the test method developed to evaluate asphalt crack healing by 3PB testing. Extracted from [31].

Lastly, the Healing Level (HL) is calculated as the ratio between the maximum load applied after the crack-healing process and the maximum load originally applied to the sample. In [167], this method was used to evaluate the effect of the capsule content and identify the optimum resting time that maximises asphalt crack healing. This research concluded that, in dense asphalt mixtures, the maximum healing level was reached within 72 hours of resting time. Also, the healing level increased with the capsule content, although 0.5% of capsules was determined as the optimum dosage for maximising asphalt self-healing without compromising the overall performance of the mixture. Similar conclusions were reached in [147] and in [168], that identified constant healing levels after 96 hours of resting time on dense asphalt, and SMA, respectively.

This novel methodology was used as well in [31] to evaluate the effect of the healing temperature on the capsule's performance. The results were consistent with prior research as to the healing time and the effect of the capsule content on the healing level. Moreover, this research study found that for temperatures up to 30 ºC, the addition of capsules to the asphalt increased its healing level. However, samples without capsules reached higher healing levels than those with capsules at 50 ºC,

which might be explained due to the changes in the bitumen viscosity and flow characteristics induced by the higher healing temperature.

Based on this testing method, in [159] another methodology was proposed to determine the healing index of SMA samples containing capsules by reflective cracking fatigue testing. The test setup to simulate reflective cracking is summarised in Figure 2.23, and consists of a wheel tracker that applies a cyclic load on an asphalt sample supported by a concrete plate with a gap in the middle, that is resting on the top of a neoprene layer. This novel methodology includes the following steps:

- **Step A:** Determination of the median number of cycles resisted by samples with and without capsules until failure.
- **Step B:** Reflective cracking generation, by applying a percentage of the total median number of cycles resisted by the samples.
- **Step C:** Asphalt crack healing, stopping the test for 24 hours at 20 ºC to let the oil diffuse and make the bitumen flow, boosting asphalt crack healing. Then, samples are subjected again to cyclic testing until failure under the test conditions of Step A.

Lastly, the Healing Level (HL) of the sample is calculated as the total number of cycles applied on the sample minus the median number of cycles resisted, divided by the median number of cycles resisted.

In [159], this test method was used to compare the HL of different types of capsules and determine the optimum timing for the application of the resting period. The authors concluded that asphalt crack healing on samples with capsules is maximised when the resting period is implemented after subjecting the sample to 30% of the median number of cycles until failure. Besides, the Healing Level increased on asphalt containing capsules, directly proportional to the amount of oil released. Moreover, the capsules that optimised asphalt self-healing on SMA mixtures, without compromising its overall performance, had an average diameter of 1.4 mm and a compressive strength of 11.3 N.

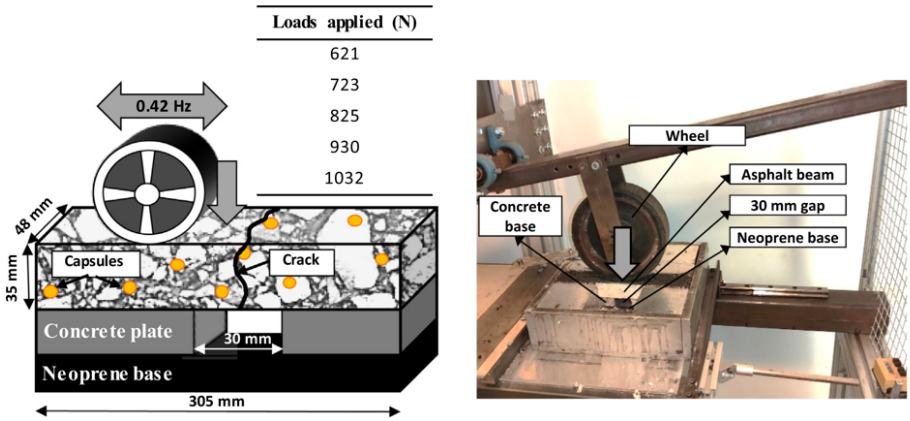


Figure 2.23. Test method developed to evaluate asphalt crack healing by reflective cracking fatigue testing: (a) Schematic representation and (b) testing equipment. Extracted from [159].

2.4.5 Numerical Models

Literature on the use of numerical models to evaluate encapsulated rejuvenators or asphalt containing encapsulated rejuvenators is limited. In [169], a Discrete Multi-Physics model (DMF) was proposed to simulate the performance of encapsulated rejuvenators under uniaxial compression testing. This model was validated with experimental data and could accurately reproduce the capsule breakage of core-shell capsules, see Figure 2.17(A1), and the release of the rejuvenator. This assessment was completed with a parametric study, to evaluate the effect of the material properties on the mechanical performance of the capsules.

However, DMF is a relatively new modelling and simulation tool and, in pavement engineering, micromechanical two-dimensional (2D) or three-dimensional (3D) Finite Element Modelling (FEM) is the prevalent choice. Most asphalt geometries for FEM are generated by processing CT scans of laboratory samples, using digital catalogues of aggregates, or directly discretizing both the aggregates and air voids as spheres. Then, asphalt mastic or bitumen is modelled as a viscoelastic material, while aggregates are assigned elastic properties or evaluated as rigid body particles for computational simplicity. Lastly, the accuracy of these models and the hypothesis considered are validated by comparing numerical and experimental results.

FEM has been used for evaluating preventive maintenance treatments in Porous Asphalt mixtures [170], assessing the impact of the aggregate embedding on chip seal treatments [171], predicting the viscoelastic properties [172] and mechanical performance [173] of asphalt mixtures, studying the micro damage initiation on asphalt mixture due to thermal stresses [174], and analysing the effect of the aggregate morphology on the compressive behaviour of SMA asphalt [175], among other examples.

In fact, FEM has been used as well for the evaluation of asphalt containing capsules. In [48], the capsules were modelled as viscoelastic particles in a 2D micromechanical model, using MATLAB for a more realistic discretization of the asphalt mixture. Then, a parametric study was conducted to evaluate the impact of the capsule size and dosing on the capsule activation and asphalt's viscoelastic properties under loading conditions. In [176], cylindrical asphalt samples containing capsules were evaluated using a 3D FE model, in which asphalt was modelled as a homogeneous material and the capsules, which were discretized as spheres randomly located within the cylindrical sample, were assigned elastic properties. This study evaluated the correlation between the capsule content and asphalt's response to creep tests. Lastly, in [177], a 3D micromechanical FE model was used to simulate different loading cases on a specimen of SMA containing capsules, to evaluate the stress field in the capsules.

2.5 Lattice Metamaterials

2.5.1 Metamaterials

Metamaterials, which are characterised by their microstructural geometry rather than the material composition, can acquire qualities that are normally not present in nature [178], providing a smart and adaptive alternative to conventional materials [179]. There are different types that are worth mentioning, such as acoustic, thermal and mechanical metamaterials. The latter is a type of architected structure designed to enhance the mechanical response, and the existing studies in this field can be categorised into [178]:

- **Material design at the physical level:** Investigating functioning materials and their mechanisms.
- **Structural design at the local level:** Designing periodic patterns that are going to comprise the microstructure, using digital tools such as topological design or biometric optimization.
- **Structural design at the global level:** Manufacture mechanical metamaterials by fabricating and assembling the designed microstructures
- **Inverse design and application at the industrial level:** To implement the use of metamaterials at an industrial level, not only affordable and efficient manufacturing must be achieved, but also inverse design to attain the required properties.

Mechanical metamaterials have promising applications in civil engineering, such as improving structural and material performance [[180],[181],[182]], protecting infrastructures from impact [[183],[184],[185]] and seismic damage [[186],[187],[188],[189]], or reducing noise and vibration pollution [190], as summarised in Figure 2.24.

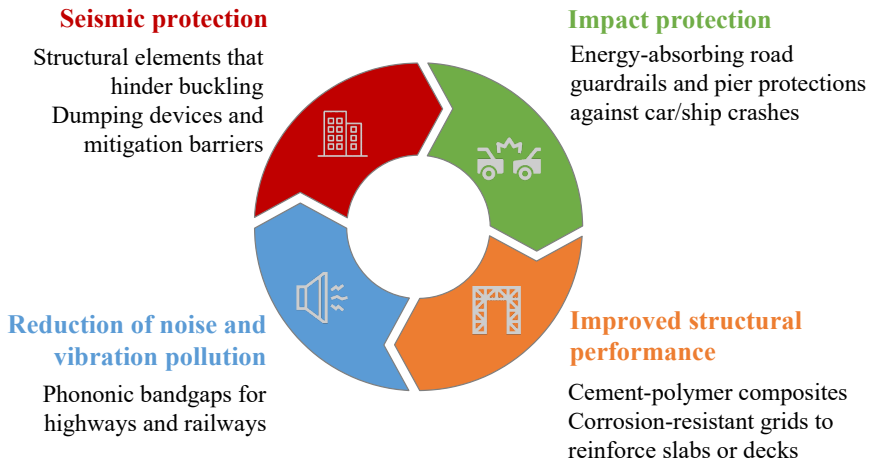


Figure 2.24. Potential applications of metamaterials in civil engineering.

2.5.2 Lattice Metamaterials

2.5.2.1 Lattice Structures

The distinctive properties of porous structures were initially studied by Gibson & Ashby, who referred to them as “cellular solids” after using the term "cell" to describe their structure, composed of interconnected beams or surface elements that conform the edges and faces of the unit cells [191]. Among other outstanding properties, these lightweight structures can withstand significant deformations at an almost constant stress under compression loading, exhibiting an excellent energy-absorption performance; their porous structure made of multiple unit cells makes them suitable for acoustic and thermal insulation; and their vast surface area and pore connectivity can be used in multiple fluid and biomedical applications [[191],[192],[193]]. Although several classifications have been proposed over time, they can be broadly categorised into:

- **Foams.** They have a random cell formation and distribution, and they are frequently classified into open-cell foams and closed-cell foams. They can be easily identified in natural materials such as cork or bones, but also polymers can be foamed [191].
- **Honeycomb panels or 2D lattice structures.** They can be described as prismatic cellular structures formed by the extrusion of a 2D arrangement, in which the shape and size of the unit cells are regular. Some studied shapes for the unit cells include triangular, square, or hexagonal prisms, and tetrahedrons. There is a current interest in re-entrant auxetic honeycombs and chiral honeycombs that exhibit a negative Poisson ratio [[194],[195],[196]].
- **3D lattice structures**. They are generated by the array of unit cells with edges and faces that can be uniform or non-uniform in shape, size and distribution [[193],[197]]

Honeycomb and foams, which can be commonly found in nature, (e.g. cork or trabecular bone) were among the first cellular materials to be studied, and then, in light of the recent advances in Additive Manufacturing (AM), the focus changed

towards architecting lattice structures with more complex geometries [[198],[199]]. Hence, lattice structures are commonly employed in the design of mechanical metamaterials [200] to obtain enhanced mechanical properties that are optimised through their microstructure (type, size and arrangements of unit cells), providing high deformation resistance, or enhancing the energy absorption and damping properties [201]. Moreover, numerical modelling can be used to optimize the internal structure of the lattices to attain the required mechanical properties, becoming an effective alternative to conventional experimental optimizations [[178],[197],[198]].

2.5.2.2 Classification of Lattice Structures

There have been numerous attempts to classify lattice structures according to the characteristics of their microstructure, including the geometry of the unit cell and the assembly approach. In [192], Bhate attempted to synthesize and unify various criteria and nomenclatures, establishing three levels for categorising lattice structures based on the decisions taken during the design stage, as summarised in Figure 2.25.

- **Tessellation,** which is the division of space into independent, volumes of a certain shape. During the design stage, a tessellation pattern must be selected. They can be broadly categorised into periodic tessellations, in which both the elements and their connectivity are prescribed; stochastic tessellations that emerge from a function, such as the Voronoi tessellation; and hierarchical tessellations, that are commonly found in nature.
- **Elements.** The type of elements inside the spaces defined by the tessellation pattern must be specified, which can be beam-based or surface-based. In beam-based lattices, the cross-section of the beam is defined, while its length depends on the tessellation pattern and connectivity. Flat surface elements can be used as well, but curved surface elements such as Triply Periodic Minimal Surfaces (TPMS) have been more extensively studied.
- **Connectivity.** Tessellated spaces must also be connected through the edges, faces or vertices of the elements during the design stage.

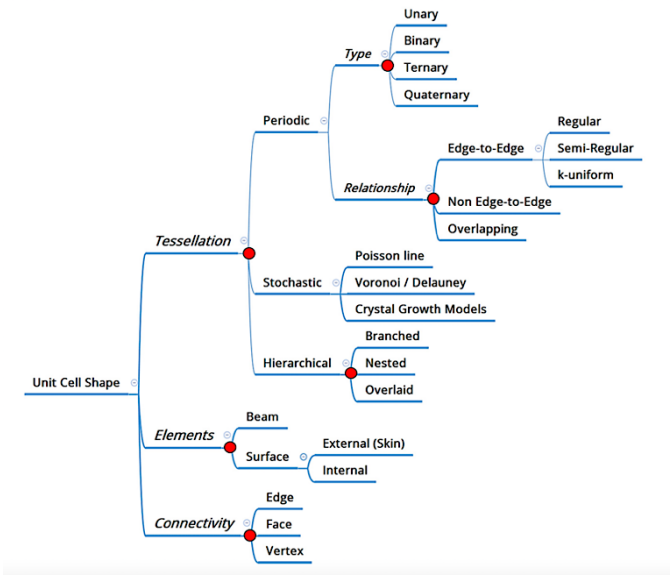


Figure 2.25. Lattice classification made by Bhate et al. Extracted from [192]

2.5.3 Lattice Manufacturing

Additive Manufacturing (AM) or 3D printing refers to a group of manufacturing techniques that create three-dimensional objects by a progressive layering of a specific material, which could be a polymer, concrete, metal, or composite. An AM process includes Computer Aided Design (CAD) tools to generate 3D models, slicing software to transform the designed structure into a layered model, and an additive manufacturing machine to convert the model into a real structure [202].

As to the manufacturing methods, according to the American Society for Testing and Materials (ASTM), they can be classified as material extrusion techniques, powder bed fusion techniques, vat photopolymerization methods, material jetting techniques, binder jetting techniques, sheet lamination techniques and direct energy deposition techniques [203]. Some of the additive manufacturing methods that are worthwhile mentioning include:

- **Fused Deposition Modelling (FDM)**. It is a material extrusion technique that uses a polymer as the raw material (thermoplastic filament), often heated before being extruded through the nozzle of the 3D printer. Polylactic acid

(PLA) is the most used thermoplastic, and typically the only type supported by small or affordable 3D printers [202].

- **Stereolithography (SLA).** It is a Vat Photopolymerization technology, in which layers of a liquid precursor are successively subjected to UV light and therefore deliberately solidified [[204],[205]].
- **Direct Metal Laser Sintering (DMLS).** It is a Powder Bed Fusion (PBF) technique, that uses a high-power laser beam to melt and fuse areas of powdered metal. There are currently just two powders being commercialised [206].
- **Selective Laser Sintering (SLS).** It is a PBF technique with the same principle as DMLS but designed to work with a variety of metallic and non-metallic materials, such as amorphous polymers (e.g., polycarbonate), semi-crystalline polymers (e.g., polyamide PA), reinforced and filled polymers (e.g., PA coated copper powder), metals, hard metals, ceramics and foundry sand [207].
- **Electron Beam Melting (EBM).** It is a PBF technique that, unlike laser-based technologies (DMLS and SLS), melts metallic powders using an electron beam, resulting in reduced residual stresses but also a lower surface finishing quality. Even though several types of metallic powders can be used, the current research is focused on titanium and titanium alloys [208].
- **Multi Jet Fusion (MJF).** It is, along with SLS, one of the most industrialised PBF technologies. However, instead of high-power laser beams, MJF uses infrared heating to fuse the powered thermoplastic material. The areas to be fused are marked with a fusing agent that is jetted, while the contours are jetted with a detailing agent for enhanced accuracy and surface finish [209].

2.5.4 Lattice Characterization

Multiple analyses can be conducted on the compressive stress-strain curves of lattice structures to reveal key properties of their energy absorption (W), and both loading and unloading characteristics have a major impact on the lattices' performance in most applications. The energy absorbed by a cellular structure up to a certain strain

(ε_m) is represented by the area underneath the compressive stress-strain curve (ε_m), see Equation (1), and the efficiency in the energy absorption ($\eta(\varepsilon)$) can also be calculated from the stress-strain curves, as the ratio of energy absorbed up to a certain strain divided by the stress itself [[210],[211]], see Equation (2).

$$W = \int_0^{\varepsilon_m} \sigma(\varepsilon) d\varepsilon \tag{1}$$

$$\eta(\varepsilon) = \frac{1}{\sigma(\varepsilon)} \int_0^{\varepsilon_m} \sigma(\varepsilon) d\varepsilon \tag{2}$$

When subjected to uniaxial compression, an ideal energy absorber will present a rigid behaviour, showing no strain until a certain level of stress is reached, to then reveal an increasing strain at a relatively constant stress, exhibiting a linear relationship between the strain and the energy absorption efficiency, as presented Figure 2.26(a), reaching 100% of efficiency at 100% of strain (ε_1) [212].

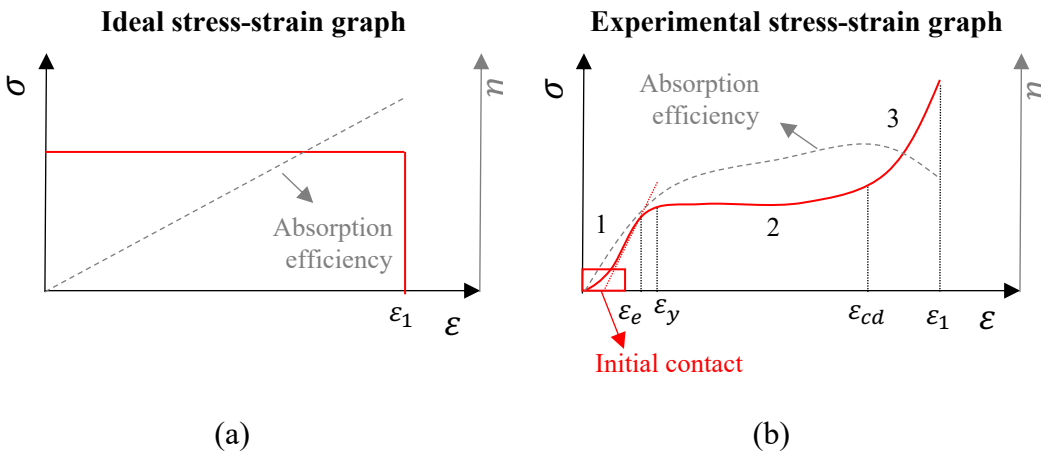


Figure 2.26. Stress-strain and efficiency-strain graphs of: (a) An ideal energy absorber and, (b) an experimental energy absorber.

Lattice structures, however, often present three regimens [213], as shown Figure 2.26(b):

- **A linear elastic region** due to the initial bending of the cell edges,
- **A stress plateau** in which the cell edges collapse by elastic buckling, plastic yielding, or brittle fracture at a relatively constant stress and,

- **A densification region** caused by the contact between the cell edges in which the stress has a steep rise while the energy absorption barely increases.

Although the exact boundaries between those regions remain ambiguous, the efficiency in the energy absorption is frequently used to determine the onset densification strain (ε_{cd}) by identifying the maximum of the efficiency-strain graph [212], as shown in Equation (3) .

$$\left.\frac{d\eta(\varepsilon)}{d\varepsilon}\right|_{\varepsilon=\varepsilon_{cd}} = 0 \tag{3}$$

Chapter 3. Materials and Methods

3.1 Introduction

This chapter presents the materials and methods used in this research and has been divided into two parts. The first part provides an overview of the raw materials and manufacturing process to produce cellular capsules, asphalt mixtures and 3D-printed lattices; and the second part summarises the test methods adopted to accomplish the research objectives. The testing procedures include the physical and mechanical characterization of the cellular capsules and the evaluation of their influence on asphalt's physical properties and mechanical performance. The experimental testing and numerical modelling used to assess the deformation of the cellular capsules embedded in asphalt when subjected to external loads are presented as well in the test methods. Moreover, the characterization of lattice structures and evaluation of energy absorbing particles in an unbound granular medium are also included. A summary of the sections of Chapter 3 is provided in Table 3.1

Table 3.1. Summary of materials and methods from Chapter 3.

Sections	**Chapter 4**	**Chapter 5**	**Chapter 6**
Raw materials and manufacturing methods	3.2.1, 3.3	3.2.2, 3.3	3.2.2, 3.4
Characterization / evaluation of cellular capsules	3.5.1, 3.5.2, 3.5.5, 3.5.6	3.5.1, 3.5.2, 3.5.3, 3.5.4, 3.5.5, 3.5.6	3.5.1, 3.5.3,
Characterization / evaluation of asphalt	3.5.7, 3.5.8, 3.5.9, 3.5.11, 3.5.12	3.5.7, 3.5.8, 3.5.9, 3.5.10, 3.5.13, 3.5.14, 3.5.15	
Characterization / evaluation of lattices			3.5.16, 3.5.17, 3.5.18
Evaluation of energy absorbing particles in a granular unbound medium			3.5.19
Numerical modelling		3.6	

3.2 Capsule Manufacturing

Encapsulated rejuvenators, also referred to as polymeric capsules, cellular capsules, or architected cellular particles, were produced by external gelation of sodium alginate in the presence of calcium chloride. For Chapter 4, they were manufactured with the procedure used in previous research (Section 3.2.1) and, for the following chapters, an upscaled procedure (Section 3.2.2) was proposed to attain the required amount of capsules for their use in an asphalt plant.

3.2.1 Capsule Production in the Laboratory

Commercial sunflower oil (relative density of 0.92 g/cm^3, smoke point of 230 ºC) was used as the rejuvenator agent. This healing agent was enclosed in cavities of a polymeric structure formed by ionotropic gelation of sodium alginate ($C_6H_7O_6Na$ in powder). Calcium chloride ($CaCl_2$ in pellets) with 95% purity was employed to cross-link sodium alginate ionically. Both sodium alginate and calcium chloride were supplied by Sigma Aldrich.

The encapsulation procedure is described in Figure 3.1, based on the methods adopted in [30] and the capsule optimization performed in [159]. A stable emulsion of oil and water was prepared by stirring 1500 ml of water and 150 ml of oil in a 2000 ml lab beaker glass at 400 rpm for 1 minute. Then, 47 g of sodium alginate were added to the emulsion (ratio o/w 0.1, a/o 0.3), and the overhead stirrer continued operating for 10 minutes. Concurrently, a solution of 1800 ml of water and 36 g of calcium chloride was prepared in a 5000 ml glass container using a magnetic stirrer at 60 rpm.

Magnets continued agitating the solution while the capsules were manufactured with the set-up described in Figure 3.1. First, 60 ml syringes filled with emulsion were connected to needles of 40 mm length and 0.8 mm gauge through elastic PVC tubing of 3 mm inner diameter. Then, a laboratory syringe pump was used to make the compound flow through the system at a rate of 7.5 ml/min. Capsules were formed when the oil-alginate emulsion was dropped into the calcium chloride solution. After the manufacturing process, capsules were collected, washed, and dried in a

dehydrator at 40 ºC for 24 h. The density of these cellular particles after the drying process was 1.13 g/cm^3. While not being used, capsules were stored at -15 ºC to prevent sunflower oil oxidation.

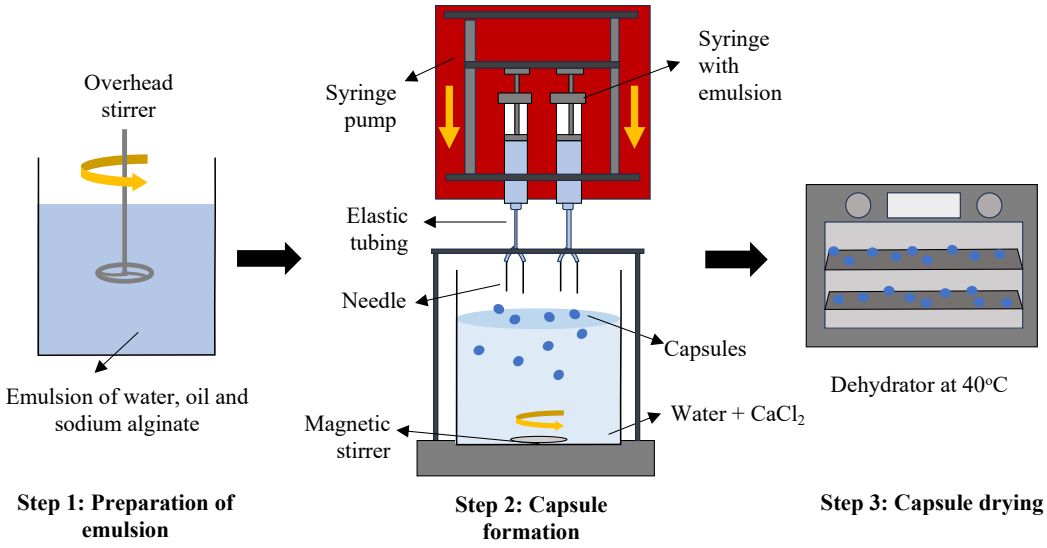


Figure 3.1. Steps for manufacturing capsules in the laboratory.

3.2.2 Upscaled Methodology for Capsule Production

The manufacturing process of the capsules was upscaled to attain the required amount of capsules for Chapter 5 (approximately 23 kg), as well as to provide an efficient methodology for future research focused on the construction and evaluation of road sections with asphalt containing capsules. The materials employed to obtain the crosslinked calcium-alginate polymer that comprises the capsules' cellular structure were sodium alginate ($C_6H_7O_6Na$ in powder), supplied by Ingredients UK, and calcium chloride ($CaCl_2$ in pellets) with 95% purity, supplied by RS Minerals. The cavities formed by the external ionotropic gelation technique contained commercial sunflower oil (relative density of 0.92 g/cm^3, smoke point of 230 ºC).

The manufacturing process comprised the same stages as the methodology used in Section 3.2.1, and details of the upscaled methodology are provided in Appendix 1. First, a stable emulsion of water and sunflower oil was prepared using a high-shear disperser of 40 l capacity with a serrated impeller, in which 17 l of water and 2 l of oil were mixed at 1000 rpm for 1 minute. Then, sodium alginate (360 g) was added

to the emulsion (ratio o/w 0.12, a/o 0.18), and the high-shear disperser continued operating for 10 minutes. Concurrently, 100 l of calcium chloride solution at 2%$_w$ were prepared in a tank of 400 l capacity, using a water pump (24 v motor) to dissolve the pellets of calcium chloride.

Emulsion droplets were generated with the set-up described in Figure 3.2, after transferring the emulsion to a smaller container of 25 l capacity connected through flexible PVC piping (25 mm inner diameter) to a pump (230 V motor), to make the emulsion flow through the capsule dripper pipework (stainless steel pipes of 25 mm inner diameter), generating emulsion droplets using nozzles of 0.8 mm. The emulsion flow was regulated with three needle valves and an additional outlet was included to return the excess emulsion to the main vessel, as presented in Figure 3.2.

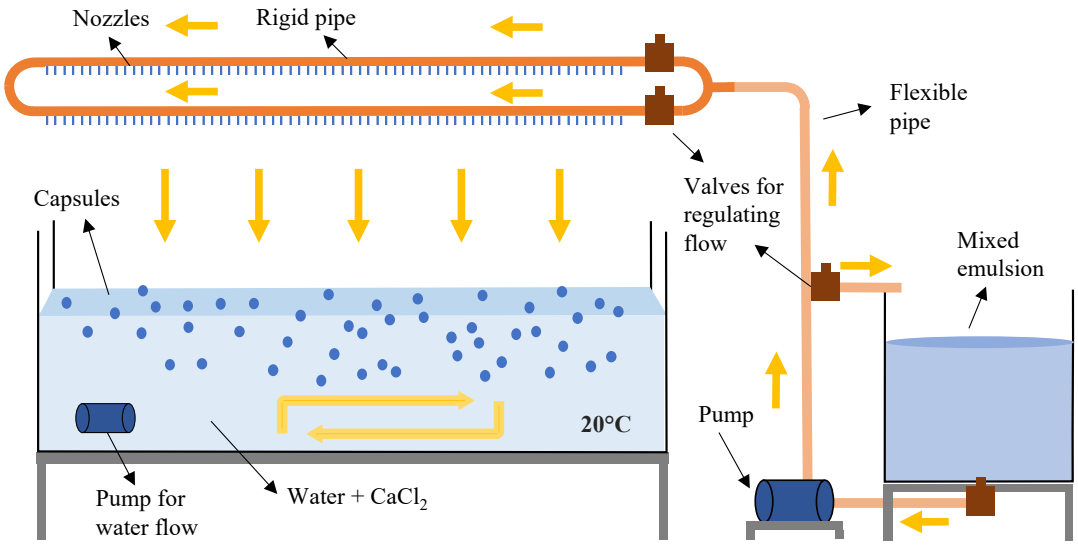


Figure 3.2. Capsule formation step with the upscaled methodology for capsule manufacturing.

The capsules were collected from the calcium chloride solution with a basket filter of 12 l capacity (Figure 3.3(a)), and the final step required coating the capsules with limestone filler (<63 µm) to aid drying (Figure 3.3(b)). After drying for 24 h at 50 °C using an industrial dehydrator, the capsules were sieved (1.8 mm sieve) to remove any excess filler or alginate remains (Figure 3.3(c)). Lastly, the capsules were packed in melting bags of 5 kg and stored in a temperature-controlled room at 5 °C.

Table 3.2. Cellular capsule composition.

Composition	**Weight (%)**
Sunflower oil	67.0%
Limestone filler	15.4%
Sodium alginate	13.1%
Water	4.5%

The density of the cellular particles after the drying process was 1.07 g/cm^3, and the capsule composition is detailed in Table 3.2. Cubes of the same composition and approximate dimensions of 20 × 20 × 20 mm^3 were also produced with an analogous manufacturing technique that did not require the drop formation step, to determine the Poisson ratio of the calcium-alginate polymer containing sunflower oil.



(a) (b) (c)

Figure 3.3. Capsules at different steps of the manufacturing process: (a) After collection from the calcium chloride solution, (b) before drying with the filler coating and, (c) after drying and sieving.

3.3 Asphalt Manufacturing

3.3.1 Raw Materials

This research used granite aggregates (Bardon Hill quarry) and limestone filler (Tunstead quarry) to manufacture asphalt at NTEC laboratory. The gradations of the nominal sizes used in Chapter 4 and Chapter 5 are presented in Table 3.3, including: 10 mm (2.82 g/cm^3), 6 mm (2.83 g/cm^3), dust (2.80 g/cm^3) and filler (2.70 g/cm^3).

Table 3.3. Aggregate gradations of the nominal sizes used for asphalt manufacturing.

	Chapter 4			**Chapter 5**		
Sieve Size (mm)	**10 mm** Pass. (%)	**6 mm** Pass. (%)	**Dust** Pass. (%)	**10 mm** Pass. (%)	**6 mm** Pass. (%)	**Dust** Pass. (%)
12.5	100.00	100.00	100.00	100.00	100.00	100.00
10	94.87	100.00	100.00	93.26	100.00	100.00
8	69.93	100.00	100.00	65.03	100.00	100.00
6.3	35.62	91.96	100.00	36.01	91.96	99.76
4	5.63	32.55	100.00	7.73	32.55	96.49
2.8	2.30	10.84	97.47	3.61	10.84	77.87
2.0	1.43	4.00	81.87	1.47	4.00	35.85
1.0	1.22	2.09	52.92	0.65	2.09	12.88
0.500	1.14	1.75	35.37	0.54	1.75	9.37
0.250	1.10	1.57	24.06	0.48	1.57	8.42
0.125	1.03	1.45	16.05	0.43	1.45	7.57
0.063	0.90	1.31	10.89	0.37	1.31	6.53

Bitumen 40/60 pen was supplied by Shell (1.027 g/cm^3, penetration at 25 ºC of 52 × 10^{-1} mm, softening point of 51.3 ºC), and Arbocel cellulose fibres (0.095 g/cm^3) were used to prevent bitumen drain drown. The cellular capsules were manufactured according to the methodologies described in Section 3.2.

In addition, asphalt was also produced at Mountsorrel Tarmac Asphalt Plant (Loughborough, UK) for Chapter 5, using Gritstone aggregates (2.78 g/cm^3) from Bayston Hill quarry, Puma bitumen 40/60 pen (1.027 g/cm^3, penetration at 25 ºC of 54 × 10^{-1} mm, softening point of 50.6 ºC) and Arbocel cellulose fibres (0.095 g/cm^3).

3.3.2 Asphalt Mixtures Composition

The composition of the asphalt mixtures used in Chapter 4 is summarised in Table 3.4. Aggregate gradations M1 to M3 comply with the grading requirements of Stone Mastic Asphalt (BS EN 13108–5 [214]), and M4 to M6 with those of Porous Asphalt (BS EN 13108–7 [215]). A range of percentages of cellular capsules was added to the asphalt mixtures in Chapter 4, varying from 0% to 2% (by total weight) in M1 for the first phase of the research plan, whilst mixtures M2 to M6 were manufactured with 0% and 1% of capsule content, based on the results from the first phase.

Table 3.4. Asphalt mixture compositions used in Chapter 4 and Chapter 5.

Sieve size (mm)	**M1** Pass. (%)	**M2** Pass. (%)	**M3** Pass. (%)	**M4** Pass. (%)	**M5** Pass. (%)	**M6** Pass. (%)	**M7** Pass. (%)
12.5	100.0	100.0	100.0	100.0	100.0	100.0	100.0
10	97.7	96.4	95.7	95.0	94.3	93.7	97.0
8	86.5	81.1	77.6	74.1	70.6	67.1	84.1
6.3	69.5	65.3	59.0	52.6	46.2	39.8	69.5
4	44.4	48.8	39.9	31.0	22.1	13.3	45.7
2.8	38.0	37.7	30.6	23.5	16.5	9.4	33.5
2.0	32.2	21.1	17.7	14.3	10.8	7.4	20.8
1.0	24.2	11.5	10.3	9.1	7.8	6.6	13.8
0.500	19.6	10.0	9.2	8.3	7.4	6.5	12.7
0.250	16.6	9.6	8.8	8.0	7.2	6.5	12.4
0.125	14.4	9.3	8.5	7.8	7.1	6.4	12.1
0.063	13.0	8.8	8.2	7.6	7.0	6.3	11.8
Binder	6.0%	6.0%	6.0%	6.0%	6.0%	6.0%	6.0%
Fibres	0.3%	0.3%	0.3%	0.3%	0.3%	0.3%	0.3%

For Chapter 5, SMA 10 surf 40/60 (BS EN 13108-5 [214]) was produced at both Mountsorrel Tarmac Asphalt Plant (Loughborough, UK) and NTEC laboratory, containing 0.0% and 0.5% capsule content by total weight. At the Mountsorrel plant, asphalt composition by weight was: Nominal size 14 mm, 5.0%; size 10 mm, 48.4%; size 6 mm, 106-%; dust, 15.4%; filler, 8.5%; bitumen, 6.4%; fibres, 0.3%. At the NTEC laboratory an analogous SMA mixture, M7 from Table 3.4, was produced under controlled conditions, to validate results obtained from testing plant-produced asphalt.

3.3.3 Sample Manufacturing

3.3.3.1 Sample Manufacturing for Chapter 4

Thirty-nine sample sets of asphalt cores were manufactured for Chapter 4, with varying aggregate gradation (Table 3.4) and compaction type (Table 3.5). Prior to asphalt manufacturing, aggregates and metallic compaction moulds were preheated at 165 ºC for 8 hours. Bitumen was also preheated at 165 ºC for 4 hours, and the cellular capsules were conditioned for 24 hours at room temperature.

Asphalt cores were produced in sets of five specimens (asphalt batches of approximately 10 kg), using a lab mixer armed with two shafts for the mixing process (BS EN 13108-35 [216]). First, aggregates and fibres were mixed for 30 seconds at 165 ºC and 135 rpm, then bitumen was poured into the mixture, and the lab mixer continued mixing for 3 minutes. The capsules were added at the end of the mixing process, in the last 30 seconds, to ensure an adequate dispersion in the mixture [163]. Afterwards, asphalt was poured into 105 mm diameter moulds and was compacted using a Marshall hammer (BS EN 12697–30 [217]), applying the number of blows per face specified in Table 3.5. The average weight of the asphalt cores was 1162 g and the sample average height ranged from 60 to 74 mm, as presented in Table 3.5.

An analogous mixing procedure was followed for manufacturing slabs with the mixture composition M1, containing 0.0%, 0.5%, 1.0%, 1.5% and 2.0% capsules by total weight. Slabs with approximate dimensions of 305×305×40 mm^3 (8.562 ± 5 kg) were produced in sets of two specimens (asphalt batches of approximately 17 kg). After mixing (BS EN 13108-35 [216]), asphalt was poured into square metallic moulds of 305×305 mm^2 and compacted using a roller compactor (BS EN 12697–33 [218]) to attain the same bulk density and air void content as the asphalt cores, see Table 3.5. Slabs of 305×305×40 mm^3 were used for rutting testing with the Hamburg Wheel tracker, while specimens of 90×90×40 mm^3 were cut from the slabs for the evaluation of asphalt's energy absorption under compression testing.

Table 3.5. Details of the core manufacturing for Chapter 4.

Mixture composition	Capsule content (%)	Compaction (Nb blows)	Sample height (mm)	Bulk density (g/cm^3)	AVC (%)
M1	0.0	40.0	65.3	2252.0	11.4
M1	0.5	40.0	65.9	2247.0	11.6
M1	1.0	40.0	64.3	2301.6	9.5
M1	1.5	40.0	65.4	2264.8	10.9
M1	2.0	40.0	65.1	2263.0	11.0
M1	0.0	20.0	63.6	2271.0	10.7
M1	1.0	20.0	63.6	2257.0	11.2
M1	0.0	30.0	61.7	2319.0	8.8
M1	1.0	30.0	62.7	2278.0	10.4
M1	0.0	40.0	61.2	2340.0	7.9
M1	1.0	40.0	62.4	2296.0	9.7
M1	0.0	50.0	60.9	2353.0	7.4
M1	1.0	50.0	61.3	2335.0	8.1
M1	0.0	60.0	60.4	2376.0	6.5
M1	1.0	60.0	60.8	2359.0	7.2
M1	0.0	70.0	60.1	2388.0	6.0
M1	1.0	70.0	60.6	2363.0	7.0
M1	0.0	80.0	60.0	2388.0	6.0
M1	1.0	80.0	60.3	2370.0	6.8
M1	0.0	100.0	59.6	2397.0	5.7
M1	1.0	100.0	60.0	2386.0	6.1
M2	0.0	50.0	65.7	2174.0	14.5
M2	1.0	50.0	66.0	2178.0	14.3
M3	0.0	50.0	66.9	2137.0	16.0
M3	1.0	50.0	67.7	2121.0	16.6
M4	0.0	50.0	68.9	2086.0	18.0
M4	1.0	50.0	69.4	2069.0	18.7
M5	0.0	50.0	71.2	2021.0	20.6
M5	1.0	50.0	70.4	2042.0	19.8
M6	0.0	50.0	73.0	1959.0	23.1
M6	1.0	50.0	74.1	1940.0	23.9
M4	0.0	100.0	66.7	2170.0	14.7
M4	1.0	100.0	66.0	2193.0	15.0
M4	0.0	70.0	68.0	2153.0	15.4
M4	1.0	70.0	67.7	2115.0	16.9
M4	0.0	40.0	68.2	2104.0	17.3
M4	1.0	40.0	68.2	2063.0	19.0
M4	0.0	30.0	69.0	2063.0	19.0
M4	1.0	30.0	68.8	2080.0	18.3

3.3.3.2 Sample Manufacturing for Chapter 5

At Mountsorrel Tarmac Asphalt Plant, asphalt was produced using a drum-mix facility, with a total mixing period of 27 s at 180 °C. The production was divided into 4 batches of 0.5 tonnes each. The first batch (B1) did not contain cellular capsules, whereas the subsequent batches contained 0.5% capsules by total weight. As no prior research used industrial facilities to produce asphalt containing cellular capsules, they were incorporated at different stages of the mixing process in melting bags of 5 kg: With the aggregates in the second batch (B2); at second 5/27 of mixing in the third batch (B3), to evaluate whether the maximum mixing time could damage the capsules; and at second 20/27 in the fourth batch (B4), to evaluate if the minimum mixing time could affect the distribution of the capsules; as summarised in Table 3.6. A total of 800 kg of loose asphalt was packed into boxes of approximately 10 kg and transported to the NTEC laboratory for asphalt specimen preparation. Additionally, the composition of the four batches was analysed following BS EN 13108-1 (Annex B.3.1) [219], using methylene chloride as solvent, and BS EN 13108-2 [220].

Table 3.6. Times for adding cellular capsules into the asphalt during the mixing stage in Chapter 5.

Mixing Achieved (%)		**Mixing Time (min)**	
Asphalt plant	**NTEC Laboratory**	**Asphalt plant**	**NTEC Laboratory**
0%	0%	00:00	00:00
19%	20%	00:05	00:36
-	50%	-	01:30
74%	75%	00:20	02:15
Total mixing time (min:sec)		00:27	03:00

At the NTEC laboratory, an analogous SMA mixture was produced under controlled conditions with 0.0% and 0.5% of cellular capsule content (Mixture M7 from Table 3.4), to validate results obtained from testing plant-produced asphalt. Cellular capsules were added during asphalt mixing as presented in Table 3.6. Besides, as the binder dosing in the plant is prone to undergo certain variations, four additional SMA mixtures were manufactured with the following binder contents: 4.5%, 5.0%, 5.5%, and 6.5%. Cellular capsules were added in the last 30 seconds of mixing when

modifying the bitumen content, based on previous research at a laboratory scale [163].

SMA mixtures from the Mountsorrel plant were preheated at 170 ºC for 4 hours before being transferred to metallic moulds of 305×305 mm^2 and compacted with a roller slab compactor (BS EN 12697-33 [218]) to achieve the target air void content (4%). SMA mixtures from NTEC were directly transferred to the moulds after mixing (BS EN 13108-35 [216]) for compaction under the same conditions. The slabs' target height for rutting testing was 50 mm, whereas 100 mm diameter cores for semi-circular bending and particle loss testing were extracted from 45 mm and 60 mm slabs, respectively. Semi-circular cores required trimming the top and bottom surfaces of the specimen and adjusting the thickness to 40 mm, and a notch of 4×8 mm^2 was also made at the mid-point of the semi-core base. Cylinders of 35 mm diameter were cored as well from slabs (305×305×30 mm^2) of asphalt from the Mountsorrel plant for CT scanning.

Lastly, based on the mixture composition of the SMA produced at the NTEC laboratory (mixture composition M7 from Table 3.4), asphalt mastic samples were prepared for the Dynamic Shear Rheometer. Bitumen and aggregates up to 1 mm were preheated at 165 ºC for 4 hours, and then the aggregates were progressively mixed in the bitumen until a homogeneous mixture was obtained. Then, asphalt mastic was poured into moulds of 8 mm and 25 mm diameter and stored in a temperature-controlled refrigerator at 5 ºC until testing.

3.4 Lattice Manufacturing

3.4.1 Materials and Advanced Manufacturing

The lattices were 3D-printed by Multi Jet Fusion (MJF) using polyamides PA11 (particle size of 50 μm, powder melting point of 200 ºC) and PA12 (particle size of 60 μm, powder melting point of 187 ºC). PA12 is an oil-based polyamide obtained from petrochemical sources, whereas PA11 is a bio-based polyamide with a lower carbon footprint, usually synthesised from castor plants or other renewable sources. However, both thermoplastics possess a similar chemical structure, composed of

amide groups (CO-NH) separated by 10 (PA11) or 11 (PA12) methylene groups (CH_2) [221].

They present a remarkable performance in terms of mechanical strength, fatigue, impact resistance, and abrasion resistance. Notably, PA11 stands out due to its enhanced elongation at break, superior chemical and ageing resistance and lower moisture absorption [222]. Both polyamides are heat-resistant and show an adhesion to bituminous binders similar to that of granite aggregates [223]. Furthermore, due to the wide range of temperatures between their melting and crystallisation points during manufacturing, PA11 and PA12 are excellent for printing parts with geometric complexity [221].

As to the selected Additive Manufacturing (AM) technique, MJF provides fast printing with great accuracy and does not require any support. Moreover, the parts 3D-printed using MJF are practically isotropic and, therefore, their mechanical properties are not affected by the orientation of the part during the 3D-printing process [212].

3.4.2 Lattice Design

The lattice design was restrained by the tolerance of the additive manufacturing technique, approximately 1 mm, and the maximum size of the aggregates used in Stone Mastic Asphalt (SMA) mixtures that contain cellular capsules, which is 10 mm. Hence, the minimum thickness of the beams and surfaces was limited to approximately 1 mm and the enclosing volume of the lattice to a cube of 10x10x10 mm^3, as the preferred geometries for compressive testing are right prisms or specimens with a square or circular cross-section [224]. The generation process of periodic lattices is summarised in Figure 3.4 and started with the selection of different beam-based or walled Triply Periodic Minimal Surface (TPMS) unit cells.

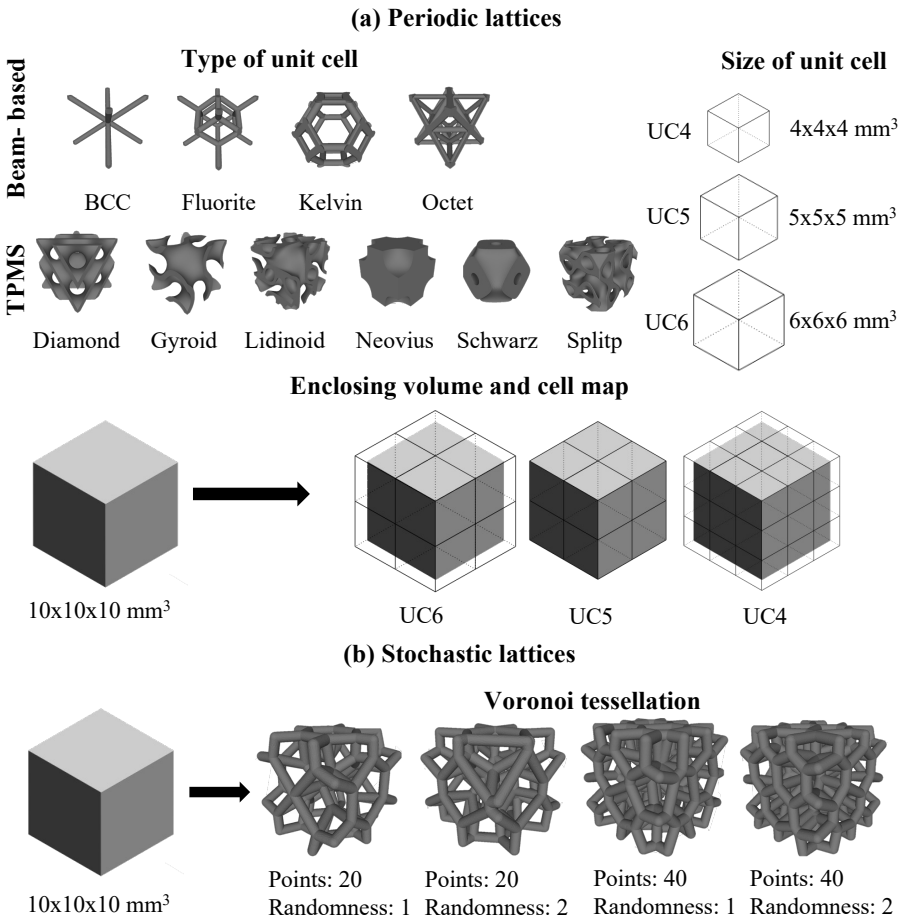


Figure 3.4. Generation of: (a) Periodic metamaterials (beam-based lattices and walled TPMS) and (b) non-periodic metamaterials (Voronoi tessellation).

Then, to generate lattices with the same microstructure and different relative densities, three sizes were considered for the unit cells. Lastly, these arrangements of cubic unit cells were centred in the previously defined enclosing volume, see Figure 3.4. Stochastic lattices, on the other hand, were generated using Voronoi tessellations and required defining the number of points and randomness of the points in the enclosing volume to generate the inner polygons, see Figure 3.4 and Figure 3.5.

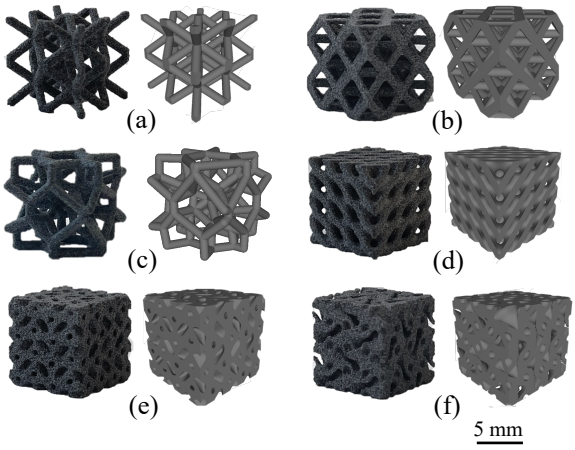


Figure 3.5. Examples of 3D-printed lattices (left) and, lattice design from which they were 3D-printed (right): (a) BCC, (b) Octet, (c) Voronoi, (d) Diamond, (e) Splitp and, (f) Lidinoid.

Lastly, the thirty-four geometries generated were discretized to obtain closed, oriented, manifold, and not self-intersecting triangular meshes for the manufacturing process. The relative density of the lattices ρ^*, was also calculated from the generated meshes, see Equation (4). The two lattices selected for the fundamental study in a granular unbound medium (see section 3.5.19) were generated and 3D-printed following the same steps but using a spherical enclosing volume instead, obtaining therefore spherical particles.

$$\rho^* = \frac{Volume\ of\ the\ lattice}{Enclosing\ volume} \tag{4}$$

To characterise the parent materials PA11 and PA12 by tensile testing, dumb-bell-shaped type 1B specimens from BS EN ISO 527-2 [225] were 3D-printed as well.

3.5 Testing Methods

3.5.1 Evaluation of the Capsule Size and Morphology

The size and morphology of the cellular capsules were examined through ImageJ software (Version 2.3.0), a digital image analysis tool. First, plan-view images of capsules in their resting position were taken to generate threshold images from which measurements of individual particles were extracted, including the area (in mm^2) and the major and minor axis of the fitted ellipse (in mm), as shown in Figure 3.6. Then, the equivalent circular area diameter (D), circularity, and Aspect Ratio (AR) were calculated through Equations (5), (6) and (7), respectively. In addition, in Chapter 5, the cellular capsules' volume was estimated as the volume of the equivalent ellipsoid, using front-view images to determine the length of the third axis.

$$D = 2 \cdot \sqrt{\frac{Area}{\pi}} \tag{5}$$

$$Circularity = \frac{4 \cdot \pi \cdot Area}{Perimeter^2} \tag{6}$$

$$Aspect\ Ratio = \frac{Major\ axis}{Minor\ axis} \tag{7}$$

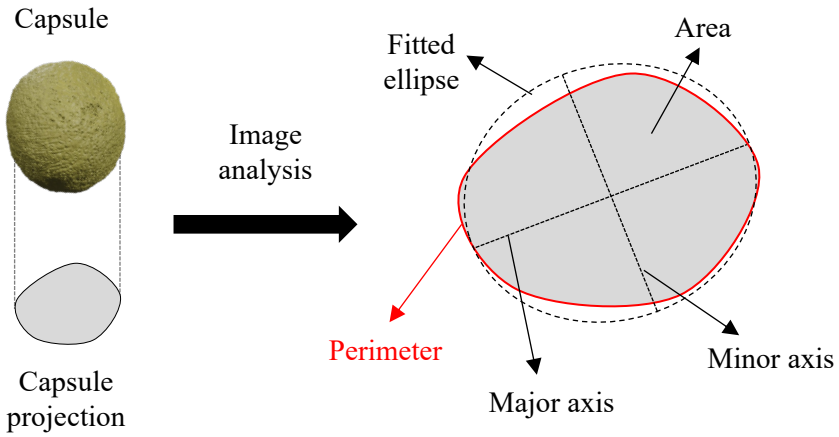


Figure 3.6. Shape descriptors of the cellular capsules.

Images from asphalt slabs containing cellular capsules after rutting testing were also processed with this tool in Chapter 4, to calculate their shape descriptors. A cut was made on the slab to obtain a photograph of the cross-section of both tested (wheel-path) and untested regions (sides) of the asphalt samples. Then, the cellular capsules were manually identified as Regions Of Interest (ROI) and measured as shown in Figure 3.6, using Equations (5), (6) and (7).

3.5.2 Capsule Imaging Through Computer Tomography Scanning

X-ray Computer Tomography scanning was used to characterise the cavities of the capsules manufactured with both methodologies defined in Section 3.2 (capsule production in the laboratory and upscaled methodology for capsule production) in Chapter 4 and Chapter 5. The equipment used was a Phoenix Nanotrom S, operating at 190 kV and 1.25 μm of spatial resolution, and image stacks (approximately 1700 cross-sectional images) were obtained from reconstructing scans with VG Studio Max (Version 2.2.6). Then, the size of the cavities in which the oil is located was determined using ImageJ on the cross-sectional images, and their equivalent diameter was calculated with the methodology defined in Section 3.5.1, through Equation (5).

In addition, in Chapter 4, cellular capsules were extracted from an asphalt core after the Cantabro test, and CT scanning was used to assess changes in the internal and external structures of the cellular capsules after testing. Cross-sectional images were used to re-evaluate the cavities of the cellular capsules and generate a 3D reconstruction using VG Studio Max.

3.5.3 Capsule Imaging Through Scanning Electron Microscope

The inner and outer structures of the capsules manufactured with the upscaled methodology (Section 3.2.2) were documented using an FEI Quanta 600 Scanning Electron Microscope (SEM). Beam settings were adjusted to a high accelerating voltage of 2 kV and spot size of 3. Sample preparation for SEM analysis required: (i) Razor-cutting samples to expose the inner structure, (ii) individual particle embedding into an epoxy resin using a vacuum system to eliminate air, (iii) specimen polishing, (iv) plasma cleaning to remove any organic contamination from the sample

and, (v) specimen platinum sputter coating for high-resolution imaging in the SEM microscopy.

In Chapter 6, an Environmental Scanning Electron Microscope (Thermo Fisher FEI Quanta 650 ESEM), was used to obtain detailed views of the cellular capsules before and after testing in a granular unbound medium. This technique was selected to document the deformation of the capsules' shape due to: i) its greater depth of field when compared against an optical microscope and, ii) lack of conductive coating on the samples. The sample preparation only required fixing the particles to the sample holders with conductive carbon adhesive tape. Then, the equipment was operated with a vacuum level of 50 Pa, a beam voltage of 10 kV and a spot size of 5.

3.5.4 Evaluation of the Capsule's Distribution and Morphology in Asphalt

X-ray Computer Tomography scanning was used to evaluate the cellular capsule distribution and morphology on asphalt manufactured at the Mountsorrel plant and compacted at NTEC laboratory. The equipment used was a Phoenix Vtomex M, operating at 200 kV and 68 μm of spatial resolution. For each sample set, 3 cores of 35 mm diameter and 30 mm height were vertically stacked using foam sheets to prevent any damage and scanned. Image stacks (approximately 550 cross-sectional images per asphalt core) were obtained from reconstructing scans with VG Studio Max (Version 2.2.6).

VG Studio Max was used as well to identify the cellular capsules as Regions of Interest (ROI) and generate coloured 3D reconstructions of asphalt samples. Then, stacks containing the capsules as ROI were exported for individual analysis of the capsules on ImageJ (Version 2.3.0), using the particle analyser of BoneJ. As the volume of loose capsules presented a normal distribution, undamaged capsules were identified in the CT scans as those whose volume was within the estimated average volume ± 2 standard deviations [226]. Lastly, the total percentage of undamaged capsules was calculated as the ratio between the volume of undamaged capsules to the total volume of the capsules in the mixture.

3.5.5 Evaluation of the Capsule Density

The density of the cellular capsules after drying and sieving was analysed using a gas displacement pycnometer, model Micromeritics AccuPyc II 1340, at room temperature (20 ºC), testing a sample size of approximately 2 g. The density (g/cm^3) was then calculated as the average of five measurements.

3.5.6 Uniaxial Compression Testing of Capsules

Compression testing was performed on cellular capsules after preconditioning the samples for 24 hours at 20 °C. The equipment used was an Instron 5969 at 20 °C and 50% humidity, operating at a displacement rate of 0.3 mm/min. In addition, an optical extensometer was coupled to the equipment to obtain accurate readings of the contact area between the steel plate and the capsule, to determine the corresponding stress–strain curves of the capsules manufactured with the upscaled methodology from Section 3.2.2. Due to the size and morphology limitations of the capsules, cubic samples of 20×20×20 mm^3 with identical composition were tested under the same conditions to estimate the average Poisson ratio (ν) using an optical extensometer.

3.5.7 Evaluation of Asphalt's Bulk Density and Air Void Content

The test specimens' maximum density (ρ_m) was determined through the mathematical procedure described in BS EN 12697–5 [227]. Then, the sealed specimen procedure from BS EN 12697-6 [228] was used to calculate the bulk density (ρ_b) of the asphalt cores, as follows: (i) Weigh dry asphalt samples, (ii) seal asphalt samples in foil, (iii) weigh sealed specimens, (iv) determine water density of the water bath, (v) submerge samples in the water bath, and (vi) weigh them underwater while avoiding any air bubbles. The asphalt slab bulk density was also determined through the Saturated Surface Dry (SSD) procedure from BS EN 12697-6 [228]. Lastly, each specimen Air Void Content (AVC) was calculated using Equation (8), from BS EN 12697-8 [229], where ρ_m is the maximum density of the mixture and ρ_b is the bulk density. The Air Void Content (AVC) of each sample set was expressed as the average of 5 specimens.

$$AVC\ (\%) = \frac{\rho_m - \rho_b}{\rho_m} \cdot 100 \quad (8)$$

3.5.8 Aggregate Loss Test

The Cantabro test was selected to characterise the mass loss of asphalt cores and assess and quantify any potential ravelling retardation due to the cellular capsules and their deformation under impact loading. It is important to highlight that the results from the Cantabro test and other devices for assessing asphalt ravelling, such as the Aachen ravelling tester, the Darmstadt Scuffing Device (DSD), or the Rotating Surface Abrasion Test (RSAT) should only be regarded as indicative of the relative resistance to ravelling of the evaluated sample tests [10].

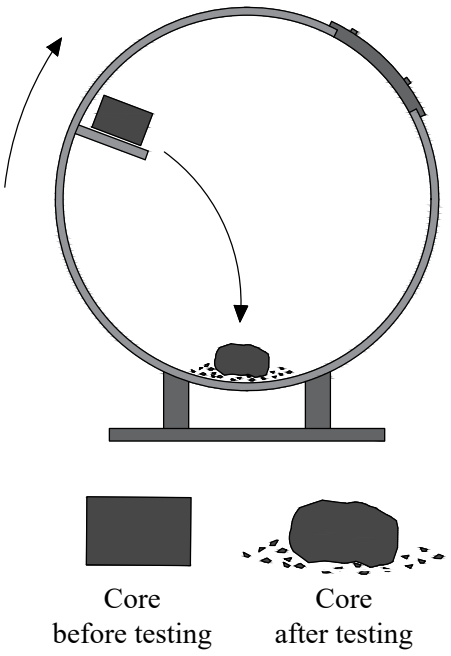


Figure 3.7. Schematic representation depicting the interior of Los Angeles abrasion machine during the Cantabro test.

The Cantabro test was performed in the Los Angeles machine without abrasive charges, which encompasses a steel cylinder with approximate inner dimensions of 700 mm diameter and 500 mm length that rotates at 31 to 33 rpm, see Figure 3.7. Following standards (BS EN 12697-17 [230]), sets of five cylindric specimens of 100 mm diameter (mass of 1.0 ± 0.2 kg) were individually tested in the Los Angeles

drum without steel balls after sample conditioning at room temperature for 4 hours. The samples' mass was recorded before and after the test, and the Mass Loss (ML) was calculated through Equation (9), where M_i is the specimen's mass before testing and M_f is the mass of the sample after 300 cycles.

$$ML\ (\%) = 100 \cdot \frac{M_i - M_f}{M_i} \tag{9}$$

Before calculating the average Mass Loss (ML) of each population, a preliminary statistical analysis of data gathered from the Cantabro test was undertaken to discard any outliers obtained from random variations. The modified Z-score (MZ_i), which utilises the Median Absolute Deviation (MAD) as an estimator, was selected for unbiased labelling of the values. It was calculated for every set of five samples, see Equation (10), where x_i is a single value from a dataset and $\tilde{x}$ is the median of the dataset. Results with MZ_i greater than 3.5 were removed as outliers from the total of five results that comprise each dataset, according to [231]. Hence, 8 outliers were removed from the total of 195 samples in Chapter 4, and 4 outliers were removed from the total of 95 samples in Chapter 5.

$$MZ_i = \frac{0.6745 \cdot (x_i - \tilde{x})}{median_i\ \{|x_i - \tilde{x}|\}} \tag{10}$$

In Chapter 4, samples containing different percentages of capsules (0.0%, 0.5%, 1.0%, 1.5% and 2.0% by total weight) were photographed before and after the Cantabro test, and RGB colour values were calculated through an image editor. An Efficiency Index (EI) was also defined to compare in Chapter 4 data from sample sets with and without cellular capsules and evaluate their performance, see Equation (11). ML_0 is the average mass loss of a sample set without cellular capsules, and ML_1 is the average mass loss of the corresponding sample set containing cellular capsules. Lastly, the determination coefficient (R^2) was calculated to assess the dependence of average Mass Loss (ML) and Efficiency Index (EI) on the compaction energy and asphalt gradation. The closer the value to 1, the higher the strength of the relationship.

$$EI = 1 - \frac{ML_1}{ML_0} \quad (11)$$

3.5.9 Rutting Resistance Test

Asphalt's stability was studied with the Hamburg wheel tracker following BS EN 12697-22 [232], to evaluate whether asphalt's permanent deformation could be affected by the cellular capsules and their deformation under cyclic loading. Sets of two specimens of 305×305 mm^2 were tested per population and, in Chapter 4, metallic packing plates of 10 mm thickness were used to adapt samples to the height of the moulds (50 mm). The test was performed with the samples fully submerged in water at 45 ± 1 ºC, and asphalt slabs were preconditioned for 4 hours at the specified temperature. Specimens were tracked by a 55 mm wide wheel at a speed of 26.6 rpm and a load of 705.0 ± 4.5 N, until 10,000 cycles or 20 mm rut depth were achieved.

$$PRD_n = 100 \cdot \frac{r_n - r_0}{t} \quad (12)$$

$$WTS = \frac{r_{10000} - r_{5000}}{5} \quad (13)$$

Every 200 cycles, readings of the vertical position of the wheel were taken at 100 points, equally distributed at ± 50 mm from the centre of the loading area of the slab. The rut depth at cycle n was then calculated as the average reading at that cycle. The proportional rut depth (%) at cycle n (PRD_n) was obtained from Equation (12), where t is specimen thickness in millimetres, r_n the vertical displacement after n cycles (mm) and r_0 the initial displacement (mm). The wheel track slope (WTS) (mm/1000 cycles) was also calculated for each specimen using Equation (13), where r_{10000} is the vertical displacement after 10000 cycles (mm) and r_{5000} the displacement after 5000 cycles (mm). Lastly, the average of the two specimens for each sample set was calculated.

3.5.10 Semi-Circular Bending Test

The semi-circular bending test was used for quality control of asphalt manufactured at the Mountsorrel plant [233]. The equipment used was an Instron 1332, operating at a mm/min. Samples (semi-circular cores of 100 mm diameter and 40 mm

thickness, with both faces trimmed and a notch of 4×8 mm^2 on the mid-point of the semi-core base) were preconditioned at -10 ^{o}C for 24 h.

The test setup entailed a pair of 20 mm diameter rollers with a span of 80 mm to support the sample base and a plate of 8 mm thickness to load the top of the semi-cores. Calculations of the maximum stress at failure (σ_{max}) and the fracture toughness (K) followed BS EN 12697-44 [234], using Equation (14) and Equation (15), respectively. F_{max} is the maximum force, D and t are the diameter and thickness of the sample, I_1 is the normalized mode I stress intensity factor, and a is the notch depth of the specimen. A total of 10 samples were tested for each batch of asphalt.

$$\sigma_{max} = F_{max}/(Dt) \quad (14)$$

$$K = \sigma_{max} \cdot I_1\sqrt{\mu a} \quad (15)$$

3.5.11 Evaluation of Asphalt Energy Absorption Under Compression Testing

The energy absorption of asphalt samples containing different percentages of capsules (0.0%, 0.5%, 1.0%, 1.5% and 2.0%) was determined using an Istron 5985 at 20°C and 50% humidity, compressing at a displacement rate of 10 mm/min. The approximate dimensions of the asphalt samples were 90×90x×40 mm^3, and 9 specimens were tested per sample set after preconditioning the samples for 24 hours. The compression stopped after reaching an approximate vertical strain of 30%. The minimum peak load of the tested specimens was determined, 69 kN, and the energy absorbed up to the corresponding strain ε_{69kN} was calculated as the area underneath the stress-strain curve (σ-ε) obtained from compression testing, following Equation (16).

$$E_{abs} = \int_0^{\varepsilon_{69kN}} \sigma(\varepsilon)d\varepsilon \quad (16)$$

3.5.12 Evaluation of Asphalt Skid Resistance

The skid resistance of asphalt slabs containing different percentages of capsules (0.0%, 0.5%, 1.0%, 1.5% and 2.0%) was determined using the Pendulum Test Value

(PTV) following BS EN 13036-4 [235], to evaluate any loss of skid resistance in the surface of the asphalt due to the oil contained in the capsules.

First, the pendulum tester and slider, as well as asphalt specimens and water, were preconditioned at 20 ± 2 ºC for 30 minutes. Then, the standardised test was performed on a rigid horizontal surface after calibrating friction in the pointer of the pendulum and adjusting the height of its arm with a marked gauge. A total of 10 readings were taken per sample, wetting specimens each time the operation was performed. Lastly, the PTV was calculated as the constant value achieved in the last three readings, as described in BS EN 13036-4 [235].

3.5.13 Evaluation of Asphalt Texture

A laser texture scanner, Ames model 9400, was used to evaluate whether asphalt's macrotexture was affected by the capsules' deformation after wheel tracking on lab-produced and plant-produced asphalt. Regions of 100×70 mm^2 were analysed on asphalt slabs before and after being tested in the Hamburg Wheel tracker, scanning 150 segments in each region to calculate the Mean Profile Depth (MPD). The generated data were filtered using a 3 mm Butterworth second-order filter before processing. The data was collected and processed under BS EN ISO 13473-1 [236].

3.5.14 Evaluation of Oil Released from the Capsules After Testing

The volume of oil released by the cellular capsules after the Cantabro test on plant-produced asphalt was calculated through Fourier Transform Infrared Spectroscopy (FTIR), following the methodology defined in [[159],[163]]. The equipment used was a Bruker Optics IFS66 spectrometer with an ATR attachment, operated in the absorption mode in the wavenumber range of 400 to 4000 cm^{-1} with 4 cm^{-1} of resolution. Sample preparation required: (i) heating tested asphalt samples for 20 minutes at 160 °C, (ii) extracting bitumen samples, (iii) homogenizing the samples. To determine reference values, virgin bitumen was blended with sunflower oil, based on the material dosing in Section 3.3.2 and the capsule composition in Table 3.2.

The absorption spectra were normalized in the range of 1720 to 1770 cm^{-1}, as seed oils can be identified due to an intensification at approximately 1745 cm^{-1} (C=O stretching vibration). The absorbance area between curves with and without capsules was calculated using numerical integration. Then, the percentage of oil released was determined by Equation (17), where $Abs.area\ capsules$ is the absorbance area of bitumen from tested samples containing capsules, and $Abs.area\ oil$ is the reference absorbance area of virgin bitumen blended with oil. An analogous procedure was followed to identify traces of the calcium alginate polymer after asphalt manufacturing with a distinct peak at 3320 cm^{-1} (-OH stretching vibration [237]).

$$Oil\ released\ (\%) = \frac{Abs.area\ capsules}{Abs.area\ oil} \quad (17)$$

3.5.15 Characterization of Asphalt Mastic Rheological Properties

The rheological properties of asphalt mastic from the SMA produced at the NTEC laboratory were characterised using a Gemini 200 Dynamic Shear Rheometer (DSR). First, an amplitude sweep test was conducted to determine the strain for the frequency sweep test, ensuring that the mastic was tested in the linear viscoelastic region. Then, a frequency sweep test was performed to determine the complex shear modulus (G^*) and phase angle (ρ) of the mastic over a range of temperatures and frequencies. Both tests were performed following BS EN 14770 [238].

The test parameters for the amplitude sweep test were set to a frequency of 1 Hz, a strain range between 0.1% and 1%, and a sample number of 300. The testing gap was set to 1 mm for the 25 mm spindle and 2 mm for the 8 mm spindle, removing any sample excess with a spatula. The temperature was set to 40 ºC for the 25 mm geometry and 10 ºC for the 8 mm geometry, in accordance with the operational procedure established by the technicians at NTEC. To remain in the linear viscoelastic region, the shear storage modulus (G') and the shear loss modulus (G'') should not differ more than 5% from the initial value. Based on the results from the amplitude sweep tests, the strain for the 25 mm geometry was set to 0.4%, and 0.2% for the 8 mm geometry for the frequency sweep test.

In addition, the following test parameters were set for the frequency sweep test: A minimum frequency of 0.1 Hz, a maximum frequency of 10 Hz, and a sample number of 11. For the 8 mm geometry, the start and end temperatures were 30 ºC and 5 ºC, respectively (6 samples). For the 25 mm geometry, the start and end temperatures were 25 ºC and 75 ºC, respectively (11 samples). Then, a master curve was constructed at a reference temperature of 20 ºC with the time-temperature superposition principle using the Williams-Landel-Ferry (WLF) equation, see Equation (18), combined with a sigmoidal fit function, see Equation (19) [[175],[239]]. ω and ω_r are the test and reduced frequencies (in rad/s), T and T_r the test and reference temperatures (in ºC), $G^*$is the complex shear modulus obtained from the test (in MPa), and C_1, C_2, δ, λ, κ, γ are the fitting parameters.

$$log(\omega_r) = log(\omega) - \frac{C_1(T_r - T)}{C_2(T_r - T)} \tag{18}$$

$$log(G^*) = \delta + \frac{\lambda}{1 + e^{(\kappa + \gamma\, log(\omega_r))}} \tag{19}$$

3.5.16 Characterization of Materials Used for MJF

The base materials used for lattice manufacturing using Multi jet Fusion (MJF) were characterised through tensile testing following BS EN ISO 527-1 [240]. Five specimens of each type were tested in an Instron 5969 with a 50 kN load cell at 20 ºC, at a loading rate of 0.5 mm/min (10% gauge length/min), and an optical extensometer was coupled to the equipment to evaluate the strain, expressed as the relative increase of the gauge length. Then, based on the measured stress-strain curve, the maximum stress and strain were calculated, as well as the Young's modulus, E.

3.5.17 Mechanical Characterization of Lattice Structures

As to the designed lattice structures, several analyses were conducted on the compressive stress-strain (σ-ε) curves to characterise key properties of their energy absorption (W). The energy absorbed by a cellular structure up to a certain strain (ε_m) is represented by the area underneath the compressive stress-strain curve (σ-ε) [213], see Equation (20), and the efficiency in the energy absorption ($\eta(\varepsilon)$) is

expressed as the ratio of energy absorbed up to a certain strain divided by the stress itself, see Equation (21) [210].

$$W = \int_0^{\varepsilon_m} \sigma(\varepsilon) d\varepsilon \tag{20}$$

$$\eta(\varepsilon) = \frac{1}{\sigma(\varepsilon)} \int_0^{\varepsilon_m} \sigma(\varepsilon) d\varepsilon \tag{21}$$

When subjected to uniaxial compression, lattice structures often present three regimens: i) A linear elastic region due to the initial bending of the cell edges, ii) a stress plateau in which the cell edges collapse by elastic buckling, plastic yielding, or brittle fracture at a relatively constant stress and, iii) a densification region caused by the contact between the cell edges in which the stress has a steep rise while the energy absorption barely increases. Although the exact boundaries between those regions remain ambiguous, the efficiency in the energy absorption is frequently used to determine the onset densification strain (ε_{cd}) by identifying the maximum of the efficiency-strain graph, as shown in Equation (22) [212].

$$\left.\frac{d\eta(\varepsilon)}{d\varepsilon}\right|_{\varepsilon=\varepsilon_{cd}} = 0 \tag{22}$$

Therefore, the designed lattices were characterised by uniaxial compression on three cubic specimens for each type as recommended in [224]. The test was performed on the same equipment used for tensile testing, with a loading rate of 0.5 mm/min up to 70% of their initial height, followed by unloading at the same rate. The stress was then calculated by dividing the compressive load by the original cross-sectional area, while the strain was computed as the relative decrease in lattice height.

The Young's modulus was estimated from the stress-strain diagram using the least square fit method in the steepest linear region, and the average strain in the plateau region (σ_{pl}) was calculated using Equation (23), where ε_y was assumed to be 0.1 [212], and ε_{cd} was determined by the maximum efficiency method. The peak stress and total energy absorption at $\varepsilon_{0.7}$ (end of loading) were also calculated, as well as the recovered strain (expressed as a percentage) after the unloading phase, measured 24 hours after the test was concluded. Lastly, the Pearson correlation coefficient was

used to identify any correlation between the relative density of the lattices and the mechanical parameters obtained from their stress-strain graphs.

$$\sigma_{pl} = \frac{\int_{\varepsilon_y}^{\varepsilon_{cd}} \sigma(\varepsilon) d\varepsilon}{\varepsilon_{cd} - \varepsilon_y} \quad (23)$$

3.5.18 Evaluation of the Manufacturability of the Proposed Lattice Structures

Before mechanical testing, the manufacturability of the designed lattices was evaluated to identify any printing irregularities that could compromise their performance, such as local printing inaccuracies in beam-based lattices or inaccurate geometries due the wall thickness of the TPMS lattices. The equipment used was a digital inspection microscope (Inspectis HD-12) to obtain detailed views of the faces of the lattice structures, and then an optical microscope (Nikon eclipse LV100ND) was used for a further evaluation of the printing irregularities. Regarding the structural integrity of the lattices, those that broke into several parts during compression testing, instead of experiencing a local collapse of the unit cells, were discarded from further testing to reduce the likelihood of particle breakage within the asphalt mixture and ensure a resilient granular medium.

3.5.19 Mechanical Response of a Composite Granular Medium Containing Energy-absorbing Particles

A fundamental study was conducted to evaluate the deformation behaviour of 3D-printed lattice structures and cellular capsules in a granular unbound medium subjected to uniaxial compression testing, to reduce the variability associated with the presence of the binder on the lattice's deformation behaviour, as well as the potential challenges that may arise during the mixing process.

In addition, to further minimise gradation inconsistencies, single-size granite stones of 1-2 mm (bulk density: 1.22 g/cm^3) and 8-10 mm (bulk density: 1.32 g/cm^3) were used to evaluate the cellular capsules (bulk density: 0.63 g/cm^3) and the selected 3D-printed lattices (bulk densities of 0.24 g/cm^3 and 0.51 g/cm^3) respectively, ensuring

that both granular media were geometrically similar [241]. Moreover, to discard the effect of introducing spherical particles on the granite granular medium, additional testing was performed using solid Nylon spheres made of PA66 (bulk density: 0.71 g/cm^3).

3.5.19.1 Sample Preparation

Uniaxial compression testing was performed on 75 mm height specimens enclosed in a cylindric steel container of 100 mm inner diameter [241] with plates on the top and base, see Figure 3.8. Sample preparation included sieving, washing, and drying the aggregates, as well as calculating the average bulk densities of the aggregates and the energy-absorbing particles, following the guidelines from BS EN 1097-3 [242]. Volumetric contents of 0% and 5% of energy-absorbing particles were used for the sample preparation [243], which included the use of a sieve shaker for 5 minutes to properly mix the particles with the aggregates, ensuring a uniform distribution in the granular medium. Then, samples were divided in half and compacted in layers, using a 2.5 kg compaction rammer [[243],[244]] and applying 4 blows per layer employing the pattern specified in [245], followed by 45 seconds on a vibration table for additional settling. Lastly, the top surface of the specimens was compacted again and levelled prior to placing the top plate.

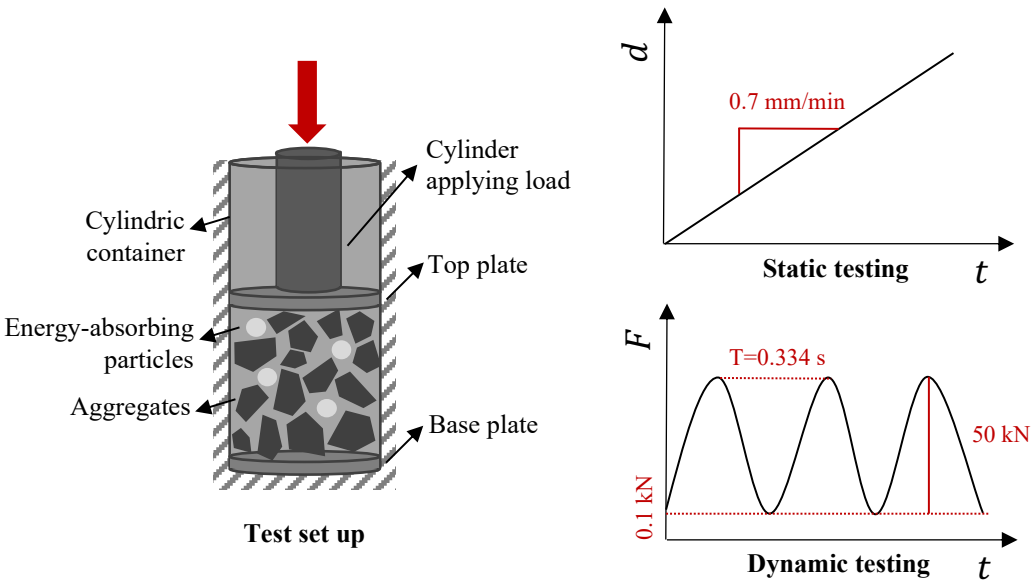


Figure 3.8. Set-up for uniaxial compression testing of the unbound granular medium.

3.5.19.2 Sample Testing

Samples were stored and tested at room temperature (20 ºC) and, for the first phase of testing, uniaxial compression was applied at a constant displacement rate of 0.7 mm/min and up to a maximum load of 50 kN (limit of the equipment), see Figure 3.8, subsequently followed by unloading at the same rate. Five specimens were tested per sample set, and then stress-strain curves were computed from the load and displacement readings to determine the average energy absorbed, see Equation (2), and the average energy recovered.

During the second round of testing, the samples were subjected to cyclic loading after being preloaded with 0.1 kN, see Figure 3.8. Samples containing 0% and 5% of cellular particles were tested over a range of loads (10, 20, 30, 40 and 50 kN) at 3 Hz (T=0.334 s) for a total of 10000 cycles, testing two specimens per sample set. Based on these tests results, sample sets containing 0% and 5% of lattice spheres were tested under the maximum load, 50kN, using four specimens per set. Lastly, after applying a moving average filter to ensure smoothness of the time-strain curves, the maximum test strain, and the average deformation rate (in millimetres per hour) were calculated.

3.5.19.3 Analysis of Materials After Testing in a Granular Unbound Medium

After cyclic testing, the aggregates were sieved to assess the influence of the energy absorbing particles, including both the cellular capsules and the selected lattices, on the aggregate crushing behaviour. Additionally, the deformation of the energy absorbing particles was evaluated by determining the equivalent diameter, aspect ratio and circularity before and after testing on sets of 30 samples, through ImageJ, following the same methodology defined in Section 3.5.1 to evaluate the capsule size and morphology.

3.6 Finite Element Modelling

Abaqus (Version 2022) was used to perform a set of simulations to supplement the findings from experimental testing in Chapter 5, in which it was found that the binder content of the asphalt mixture affected the deformation of the capsules and therefore also the results as to mass loss and rutting testing. A simplified microstructural model comprised of a cellular capsule between two stones was modelled in Abaqus, studying five scenarios in which the area of mastic surrounding the stone-capsule-stone matrix was progressively increased to evaluate the deformation of the particles under uniaxial compression. Then, a qualitative study was made by comparing the results from the simulations.

3.6.1 Microstructural Model

A two-dimensional model was constructed based on a simplified case study of a circular capsule (1.6 mm diameter) between two stones subjected to uniaxial compression, varying the area of mastic surrounding the stone-capsule-stone to create five simulations. This structure was enclosed by rigid body parts surrounded by a layer of asphalt to limit movements, see Figure 3.9. Boundary conditions were applied to the base of the model, limiting all displacements and rotations, and to the rigid top plate, imposing a vertical displacement of 0.35 mm to apply compression. A limitation of this approach is the assumption of plain stress in 2D models. Additionally, the selected geometries for the microstructural model were not generated from asphalt scans, hence, results are only qualitative in nature.

In the interface between the solid skeleton and asphalt mastic, a surface-based cohesive behaviour with a traction-separation law was defined using the default contact enforcement method and friction (coefficient of 0.4) [246]. Friction was also defined between the rigid body boundaries of the model and the corresponding layer of asphalt that surrounded them (coefficient of 0.6) [247]. Quadratic triangular elements were used to discretize the model.

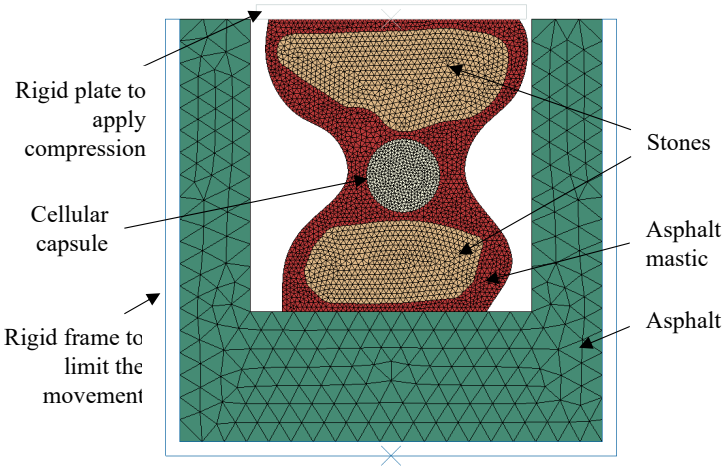


Figure 3.9. Example of a microstructural model and its components, including the stone-capsule-stone surrounded by mastic, a rigid frame surrounded by asphalt, and a rigid plate to apply uniaxial compression.

3.6.2 Determination of the Material Properties

As in prior micromechanical models of asphalt [[170],[171],[173],[175]], granite aggregates were assumed linear elastic, asphalt mastic was assumed linear viscoelastic, and the capsules were assumed to be elastoplastic.

The elastoplastic properties of the capsules were determined from the stress–strain curves obtained during uniaxial compression of the material, including the Young modulus (E) and the plastic deformation and stresses after yielding [248], see Section 3.5.6. Then, they were verified by simulating uniaxial compression testing, and comparing the predicted behaviour with the experimental data, see Figure 3.10(a). An analogous procedure was used to determine the properties of the asphalt layer (Figure 3.10(b)), that surrounded the model's rigid body boundaries, see Section 3.5.11, before the initiation and propagation of macrocracks when it reached a strain of 0.06. The properties of the granite aggregates were extracted from [249]. Table 3.7 shows the input parameters for the material properties.

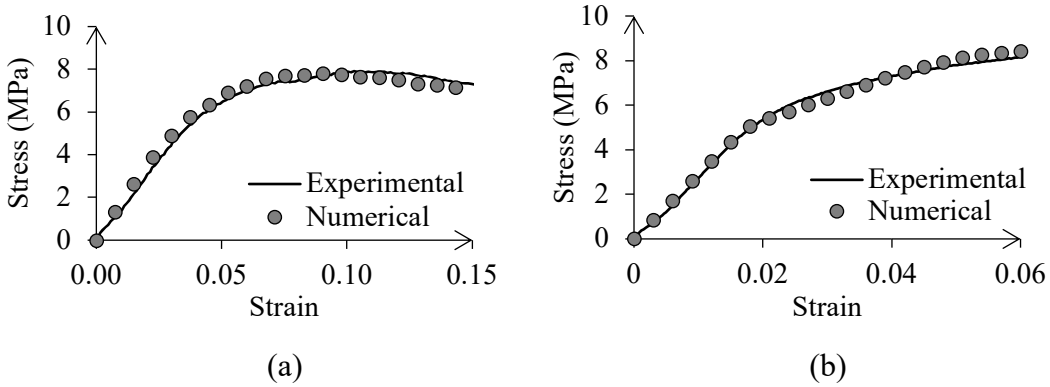


Figure 3.10. Experimental and numerical results of uniaxial compression testing of: (a) Cellular capsules and, (b) stone mastic asphalt.

Table 3.7. Material properties for the FE model.

Mastic		**Cellular particles**		**Asphalt 0.5% ACP**		**Granite**	
ti (s)	**gi**	**Yield stress (MPa)**	**Plastic strain**	**Yield stress (MPa)**	**Plastic strain**		
1.00E+04	1.00E-07	6.56E+00	0.00E+00	4.77E+00	0.00E+00		
9.24E+02	5.00E-07	7.96E+00	1.55E-02	5.38E+00	3.13E-03		
7.60E+01	1.24E-05	8.54E+00	2.63E-02	5.82E+00	5.96E-03		
8.82E+00	1.61E-04	8.74E+00	3.04E-02	6.50E+00	1.22E-02		
1.00E+00	1.84E-03	8.81E+00	3.52E-02	6.76E+00	1.50E-02		
9.85E-02	1.57E-02	9.13E+00	4.39E-02	7.09E+00	1.96E-02		
1.00E-02	7.95E-02	9.53E+00	5.66E-02	7.56E+00	2.70E-02		
4.63E-04	4.39E-01	9.66E+00	7.02E-02	7.84E+00	3.22E-02		
1.98E-05	1.08E-01						
1.98E-05	1.31E-01						
1.96E-06	2.25E-01						
G0 (MPa)	1600	**E (MPa)**	148	**E (MPa)**	274	**E (MPa)**	55000
Poisson	0.30	**Poisson**	0.35	**Poisson**	0.30	**Poisson**	0.25

Viscoelasticity in Abaqus is defined by Prony series expansion of the dimensionless shear relaxation modulus, based on the generalised Maxwell model [[170],[171]]. It can be expressed in the frequency domain with Equations (24), (25) and (26), in which $G'(\omega)$ and $G''(\omega)$ are the storage and loss modulus at an angular frequency ω, G_0 is the instantaneous shear modulus and t_i and g_i are the dimensionless Prony series parameters, which can be determined from the calibration of frequency

dependant data from the Dynamic Shear Rheometer (DSR) obtained in Section 3.5.15, which are the complex shear modulus G^* and the phase angle ϕ.

$$G'(\omega) = G_0\left(1 - \sum_{i=1}^{n} g_i\right) + G_0\left(\sum_{i=1}^{n} \frac{g_i {t_i}^2 \omega^2}{1 + {t_i}^2 \omega^2}\right) \quad (24)$$

$$G''(\omega) = G_0\left(\sum_{i=1}^{n} \frac{g_i t_i \omega}{1 + {t_i}^2 \omega^2}\right) \quad (25)$$

$$G' = |G^*| \cos\phi \; ; \; G'' = |G^*| \sin\phi \quad (26)$$

$$G_0 = \frac{E_0}{(1+\nu)} \quad (27)$$

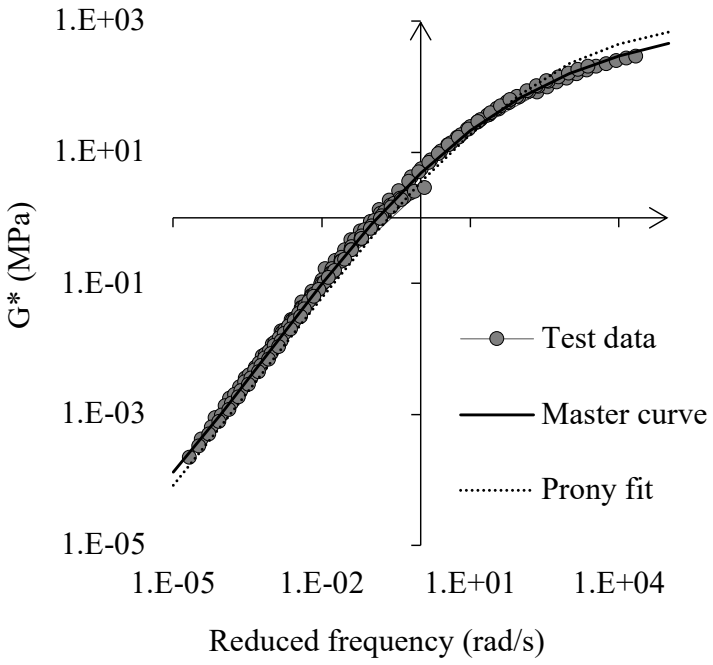


Figure 3.11. Results from DSR of asphalt mastic, master curve fitting and Prony series fitting at 20 °C.

The Prony series parameters were calibrated to asphalt mastic master curves of $G'(\omega)$ and $G''(\omega)$, using the solver from MCalibration, see Figure 3.11. Lastly, viscosity should be defined along with elasticity in Abaqus, and the E_0 modulus was obtained from Equation (27), where ν is the Poisson ratio and G_0 the instantaneous shear modulus obtained from the calibration.

3.6.3 Evaluation of Results from the FE Model

The deformation of the capsule after applying compression was evaluated by the aspect ratio (AR), see Equation (7), which expresses the ratio between the major and minor axes of the fitted ellipse. A value of 1 describes a circle, whereas an increasing aspect ratio depicts a greater difference between both axes, hence, higher deformation of the capsule and higher energy absorbed due to the gradual collapse of its internal cellular structure [191].

Chapter 4. Evaluation of Cellular Capsules to Mitigate Asphalt Stone Loss

4.1 Introduction

This chapter evaluated the delay of asphalt's aggregate loss by incorporating cellular capsules into asphalt mixtures. The cellular structure of the calcium-alginate capsules was originally intended to release an asphalt rejuvenator and promote the self-healing of asphalt cracks. However, the internal porous structure and unique impact-energy absorption properties of the capsules were considered in this study, that was divided into four phases:

- Phase 1: Manufacturing cellular capsules and analysis of their morphology using imaging techniques to assess the size and internal structure.
- Phase 2: Aggregate loss, rutting and skid resistance results of asphalts with various percentages of cellular capsules were used to determine their optimum percentage to increase asphalt's durability.
- Phase 3: Cores with different compaction levels and gradations were manufactured with and without capsules and the stone loss was determined using the Cantabro test. Thereafter, the effectiveness of the capsules in delaying asphalt ravelling and the influence of asphalt physical properties on their performance were assessed.
- Phase 4: The deformation of the cellular capsules in the asphalt during testing was studied and correlated to their microstructure. Also, the energy absorption properties of asphalt with cellular capsules were quantified.

4.2 Size and Structure of the Cellular Capsules

The size of more than 250 cellular capsules was examined through ImageJ software, and a histogram of the capsules' distribution by equivalent circular area diameter is shown in Figure 4.1, where the largest frequency was located in the 1.60-1.65 mm bin. The median diameter of the particles was 1.6 mm, with a Median Absolute Deviation (MAD) of 0.054, and a particle size greater than 1.8 mm or smaller than 1.3 mm represented less than 4% of the sample set.

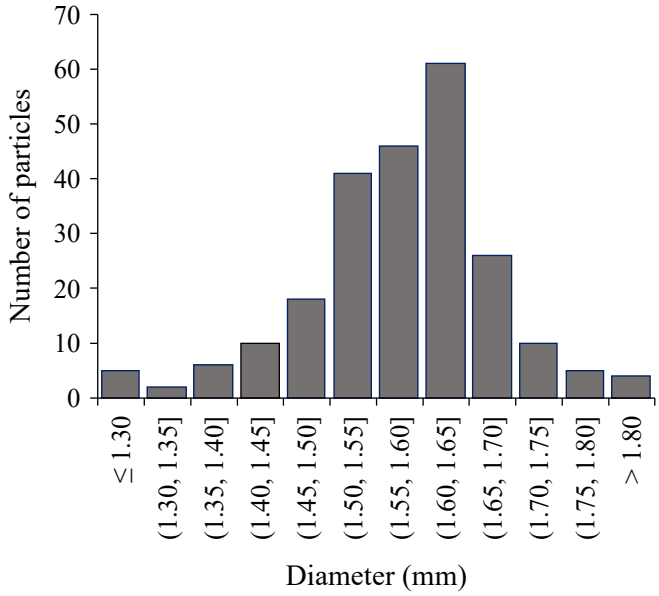


Figure 4.1. Distribution of the cellular capsule equivalent circular area diameter.

Regarding their inner structure, image analysis revealed that the cavities in which the oil is enclosed constitute 67.7% of the capsule, whereas the remaining 32.3% corresponds to the matrix generated by the calcium alginate polymer. The approximate size of these cavities is 40± 22 μm (average ± standard deviation) of equivalent circular diameter. Some areas may experience a higher density of calcium alginate, as presented in Figure 4.2, in which the polymer comprises up to 72% of the inner structure.

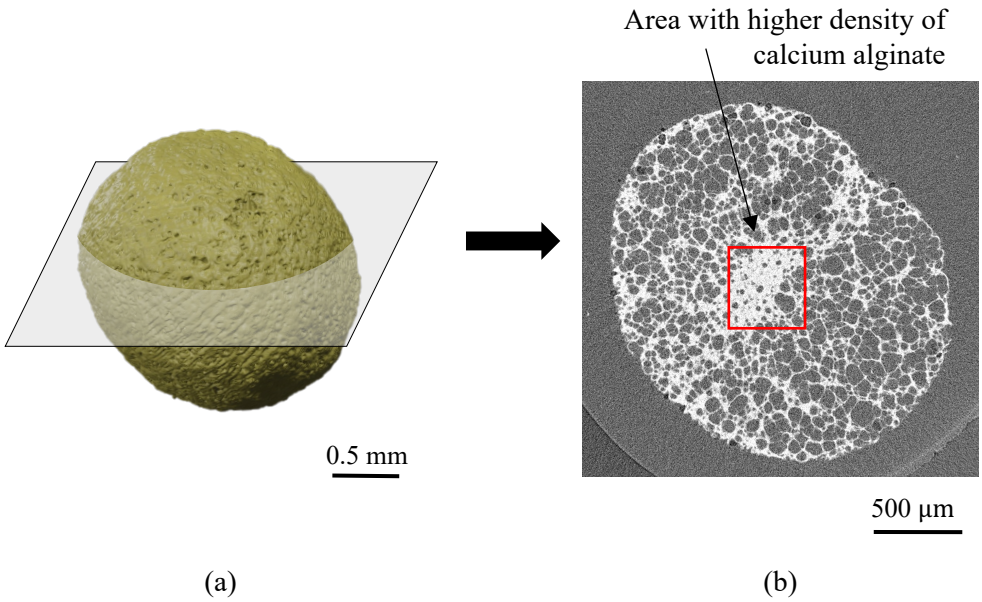


Figure 4.2. (a) CT reconstruction of an energy-absorbing particle after manufacturing and drying and, (b) top view scan of its inner structure.

4.3 Effect of Cellular Capsules on Mass Loss, Rutting and Skid Resistance

Figure 4.3 presents average mass loss results of asphalt cores (Mixture M1 from Table 3.4) containing five percentages of cellular capsules (0.0%, 0.5%, 1.0%, 1.5% and 2.0% by total weight of the asphalt mixture) tested in the Los Angeles drum for Phase 1 of the experimental programme (error bars represent ± one standard deviation). As the content of cellular capsules in the asphalt mixture was increased, the average mass loss of the sample set decreased, see Figure 4.3(a). The association between the variables was modelled by linear regression, and the goodness of the fit was assessed through the coefficient of determination, which was approximately 0.99, see Figure 4.3(a). The minimum loss of aggregates was obtained with 2% of capsule content (2.95% mass loss), with a decrease in the mass loss of nearly 60% compared to asphalt without cellular capsules, which presented an average mass loss of 7.27%.

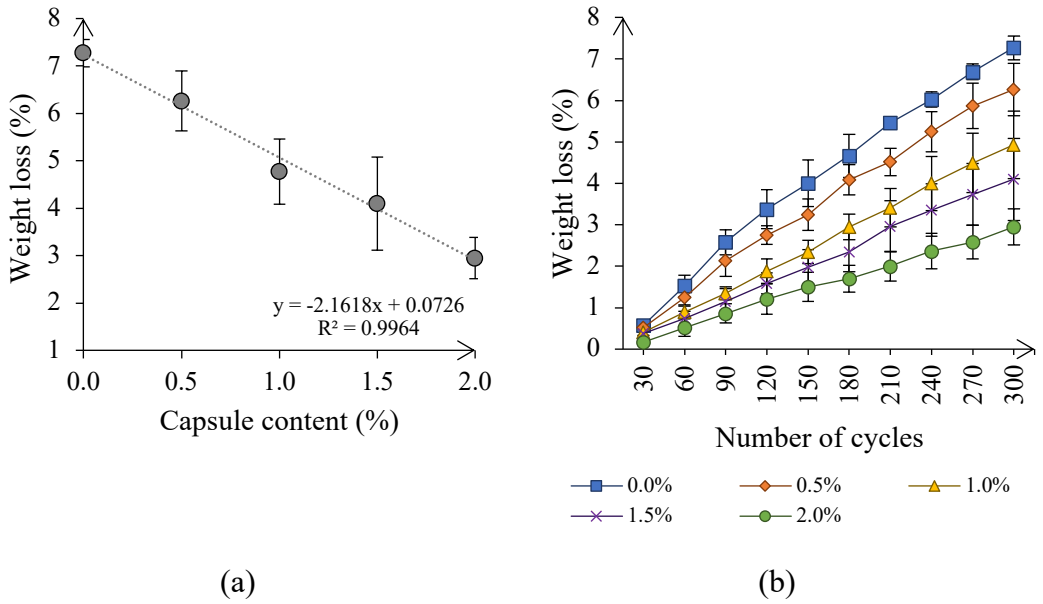


Figure 4.3. Results from ravelling testing for different cellular capsule contents: (a) Mass loss after 300 cycles and (b) degradation curves.

Figure 4.3(b) shows the cumulative loss of aggregates over cycles calculated every 30 revolutions. The increase of mass loss was steady over time, as seen in Figure 5(b), and the average mass loss rate (% mass loss per 30 cycles) ranged from 0.30% for a capsule content of 2%, to 0.75% on asphalt without cellular capsules. Thus, results presented in Figure 4.3 provide evidence of a correlation between the cellular capsule content of the asphalt mixture and its ravelling resistance, as measured by mass loss in the Cantabro test.

A further novel finding was a colour shift after testing samples in the Los Angeles drum, see Figure 4.4. The RGB model was used to characterise the specimens' colours from photographs taken of sample cores, and a higher cellular capsule content in the asphalt mixture resulted in lower RGB values of the tested specimens, that is, a darker colour. This gradual change of colour, see Figure 4.4, suggests that these particles deformed during mass loss testing, absorbing the kinetic energy and, as a result, oil was released from the cavities.

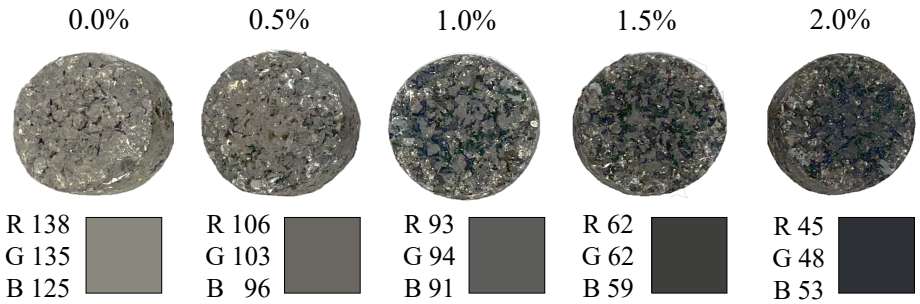
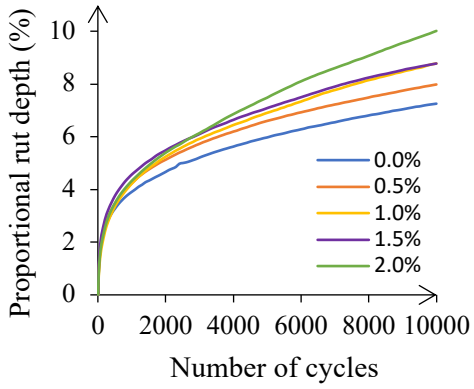


Figure 4.4. Cores with different content of cellular capsules after the Cantabro test (300 cycles) and RGB values for each asphalt sample set.

In contrast to mass loss testing, increasing the content of cellular capsules in the asphalt mixture increased rutting, as presented in Figure 4.5. The proportional rut depth evolution over time, see Figure 4.5(a), revealed different asphalt degradation rates for each content of cellular capsules from about cycle 2000. The rut depth increased by 10% (0.5% capsules) to 40% (2% capsules) on asphalt containing cellular capsules, registering a maximum rut depth of 3.83 mm. Rutting resistance of tested slabs should be considered acceptable, as the rut depth was far less than the 10 mm maximum recommended by [107].



(a)

Capsule content (%)	Ruth depth (mm)	Proportional rut depth (%)	Wheel track slope (mm/1000 load cycles)
0.00	2.76	7.26	0.10
0.50	3.05	7.98	0.11
1.00	3.37	8.79	0.14
1.50	3.32	8.79	0.13
2.00	3.83	10.02	0.19

(b)

Figure 4.5. Results from rutting testing for different cellular capsule contents: (a) Proportional rut depth over cycles and (b) summary of results.

The present findings show that rutting development and the cellular capsule content in the asphalt are related, supporting the notion that these particles are deformed by external forces, modifying asphalt mechanical properties. Lastly, it has been concluded that the addition of cellular capsules does not affect asphalt skid resistance, after obtaining PTV values of 69, 65, 68, 66 and 71 on asphalts containing 0.0%, 0.5%, 1.0%, 1.5% and 2.0% of capsules, respectively.

In view of the results obtained from evaluating the mass loss, rutting and skid resistance, a cellular capsule content of 1% by total weight was selected for a more extensive study of asphalt ravelling. This percentage generated significant mass loss mitigation without showing additional asphalt distresses, such as stripping in the wheel path after rutting testing.

4.4 Effect of Compaction Energy on Mass Loss

Compaction is a crucial stage of the asphalt manufacturing process, in which the solid skeleton that will resist external loading is defined. Figure 4.6 depicts mass loss variation as a function of the number of blows applied per face by the Marshall compactor, representing the compaction energy. Asphalt cores containing 0% and 1% of capsules (mixture M1 from Table 3.4) presented less mass loss after the Cantabro test for an increasing number of blows, see Figure 4.6. Furthermore, substantially better results were obtained by adding cellular capsules to the asphalt, mitigating the mass loss by 13% (100 blows) to almost 25% (20 blows), as presented in Figure 4.6.

When the Cantabro test is performed, aggregates from the core surface are subjected to an impact load that gradually loosens them from the solid skeleton, until they are finally detached due to a cohesive fracture of the binder caused by an excess of tensile stress. Hence, poor compaction during the sample manufacturing reduces the contact points (i.e. interfacial transition zone) [250] and prevents an adequate bond between the aggregates and the binder, ultimately triggering ravelling. However, the compaction of the asphalt samples with cellular capsules may be increased during testing due to the energy absorption capability of the capsules, that deform under impact loading and increase interactions within the aggregate skeleton.

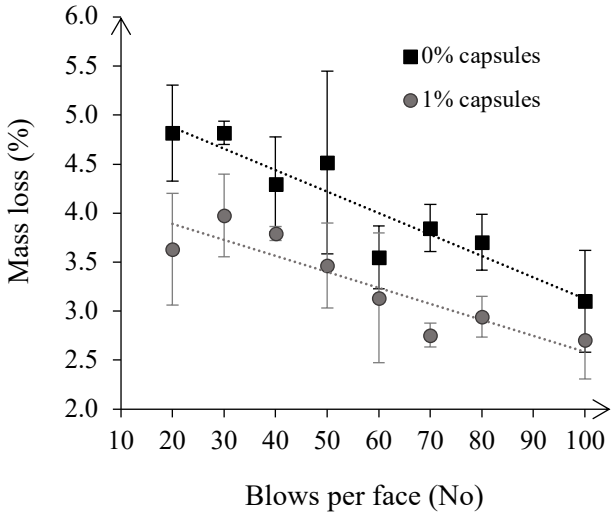


Figure 4.6. Effect of the compaction energy (number of blows per face using the Marshall compactor) on the mass loss of asphalt containing 0% and 1% of cellular capsules.

4.5 Effect of Asphalt Gradation on Mass Loss

Five additional asphalt gradations (mixtures M2 to M6 from Table 3.4) containing 0% and 1% of cellular capsules were tested in the Los Angeles machine to assess the effect on ravelling of the fraction of the largest aggregate. Test results are presented in Figure 4.7, where the mass loss was plotted against the number of 10 mm aggregates (determined from the stone count of a sample of 100 g of unbound 10 mm aggregates). The percentage of mass loss showed exponential growth as the number of maximum size aggregates increased in the asphalt mixture. However, as the fraction of 10 mm aggregates increased, the standard deviation increased as well, see Figure 4.7; this is thought to be a result of a higher mass loss resulting from the loss of larger aggregate.

Incorporating cellular capsules into the asphalt mixture yielded increasingly good mass loss results, reducing the mass loss by at least 24% and up to 30%, as presented in Figure 4.7. Nevertheless, the capsule efficiency index fluctuated with the proportion of 10 mm aggregates in the asphalt mixture. After being tested, visual inspection of asphalt core condition, shown in Figure 4.8, revealed a diminished degree of disintegration of asphalt containing the cellular capsules and darker colour that might be associated with their deformation and subsequent oil release.

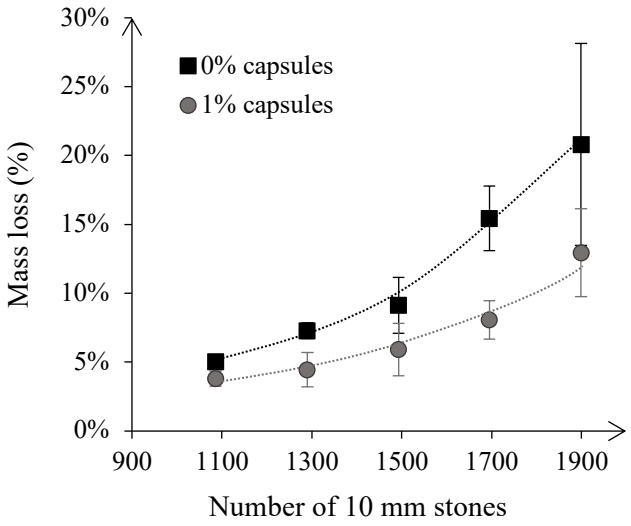
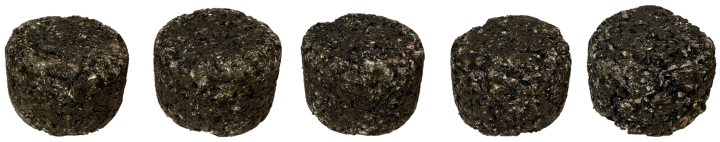


Figure 4.7. Effect of the asphalt gradation on the mass loss of asphalt containing 0% and 1% of cellular capsules.

No of 10 mm aggregates	1086	1290	1493	1695	1899
0% capsules					
AVC (%)	14.46 %	15.96 %	18.03 %	20.63 %	23.11 %
Density (kg/m^3)	2174	2137	2086	2021	1959
0% capsules					
AVC (%)	14.32 %	16.60 %	18.70 %	19.81 %	23.87 %
Density (kg/m^3)	2178	2121	2069	2042	1940

100 mm

Figure 4.8. Photographs of asphalt cores after the Cantabro test with and without cellular capsules, and physical properties of the cores before testing.

Previous studies [251] reported that shear stresses induced by the contact of vehicle tyres were concentrated on the largest aggregates. In the LA machine, if the highest loads are applied to the largest aggregates, this would result in the mass loss due to the loss of these aggregates, having a more significant influence on the overall mass loss (as shown in Figure 4.7). The addition of cellular capsules to the mixture may reduce the stresses on these aggregates by deforming and absorbing some of the load during the Cantabro test.

4.6 Influence of AVC on Mass Loss

Both poor compaction and an imbalance between the aggregates in the asphalt gradation may increase the number of interconnected voids. For this reason, mass loss values of sample sets from mixture M1 (varying compaction energy - Section 4.4) and mixtures M2 to M6 (varying asphalt gradation - Section 4.5) containing 0% and 1% of capsules were plotted against the air void content in Figure 4.9. This graph was supplemented with results from testing additional sample sets (mixture M4 varying the compaction energy, see Table 3.5). The mass loss after the Cantabro test increased with the AVC up to about 14%, as presented in Figure 4.9, after which it grew more rapidly. This suggests that asphalt mass loss is mainly dominated by the air void content.

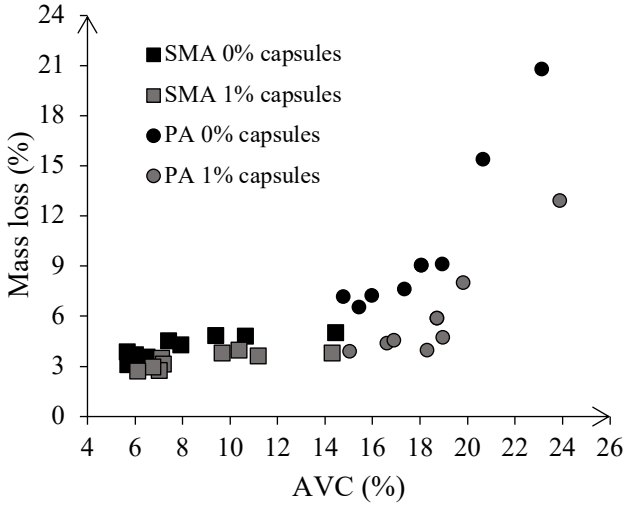


Figure 4.9. Mass loss and AVC of asphalts containing 0% and 1% of cellular capsules.

The mass loss envelope of asphalt cores containing cellular capsules, see Figure 4.9, lies below the one corresponding to asphalt without capsules, implying that adding cellular capsules to the asphalt contributed to ravelling mitigation. The efficiency index (reduction of mass loss, expressed in %) of the cellular capsules was also calculated and plotted against the air void content, as presented in Figure 4.10. Mass loss reduction ranged from 13% to almost 56%, and the determination coefficient of approximately 0.6, see Figure 4.10, indicated that cellular capsules' performance on ravelling mitigation is likely to depend on the air void content of the asphalt mixture.

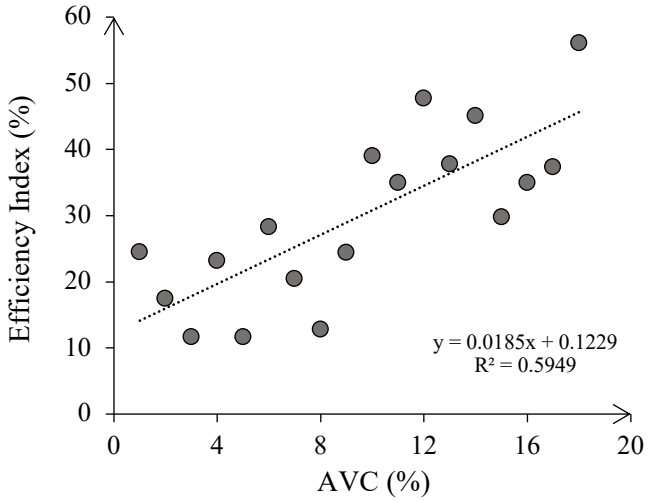


Figure 4.10. Efficiency index for asphalt mixtures containing 1% of cellular capsules, based on the Air Void Content (AVC).

4.7 Influence of Cellular Capsules on Asphalt Volumetric Properties

Figure 4.11 presents average Air Void Content (AVC) measurements of core sample sets of asphalt mixtures M1 to M6 containing 0% and 1% of cellular capsules from Phase 2 of the experimental programme before testing. Each set was composed of five samples, modifying the compaction level and asphalt gradation according to Table 3.5. Data from Figure 4.11 could be fitted to a linear equation, and regression analysis of paired AVC values yielded an R-squared of 0.98, demonstrating a correlation between the variables.

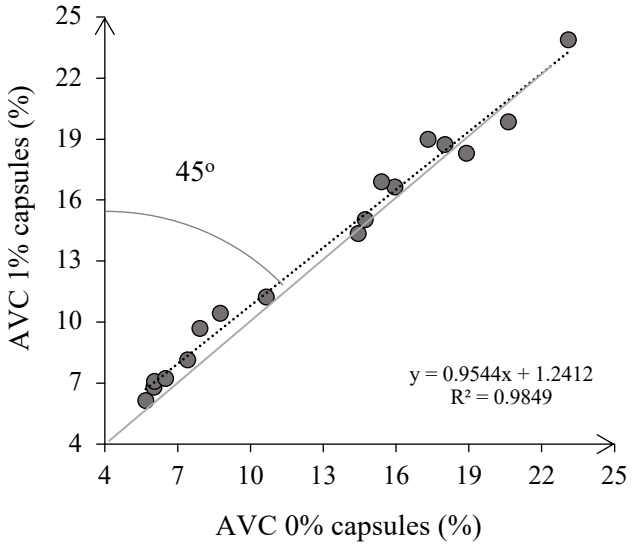


Figure 4.11. Correlation between Air Void Content (AVC) of asphalt mixtures with and without cellular capsules.

Moreover, samples containing 1% of cellular capsules presented higher AVC than specimens without these particles, as seen in Figure 4.11, where results rest largely above the 45º angle line. Similar variations of AVC of asphalt containing capsules have also been reported in previous studies [31]. Overall results from asphalt air void content analysis suggest that the size and number of the cellular capsules may affect asphalt's solid skeleton and hence, alter its physical properties. The density of these particles, lower than that of aggregates and binder, can also explain the reduction of specimen bulk density seen in Table 3.5.

4.8 Assessment of the Cellular Capsule Deformation During Testing

The cross-section of asphalt slabs containing 1% of cellular capsules was examined after rutting testing to assess any changes in the morphology of the cellular capsules- Digital image analysis revealed deformation of the capsules in the loaded area (wheel path), as presented in Figure 4.12, compared to the ones located in the slabs' edges (untested areas). The area of the cellular capsules was reduced by 24% in the wheel path and showed a higher aspect ratio that increased by 15% and a lower circularity that decreased by 7%. Changes in these shape descriptors were significant, as revealed by a Student's t-test ($P < 0.05$). The energy absorption and deformation of

these cellular particles induced by loading could affect how aggregates interact within the skeleton, changing the forces between the aggregate skeleton and the binder and hence the adhesion between the two, see Figure 4.12.

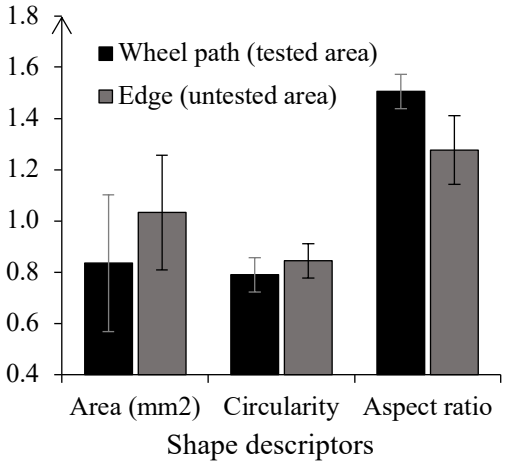


Figure 4.12. Shape descriptors of cellular capsules embedded in asphalt slabs containing 1% of cellular capsules after testing in the Hamburg wheel tracker.

To evaluate the deformation of the cellular capsules under impact loading, several samples were extracted from a core after the Cantabro test. As presented in Figure 4.13(b) and (c), CT scans revealed deformations of the cellular capsules in the contact areas with the aggregates, as well as certain abraded regions that might have originated during asphalt manufacturing (mixing and compaction) [159]. This implies that when the cellular capsules are subjected to impact loading, they adapt their shape to the surrounding aggregates (Figure 4.13(a)), absorbing the energy and increasing asphalt compaction level. In Figure 4.13(c) the damage in the capsule (1.4 mm diameter) was generated by an aggregate of an approximate size of 1.6 mm. This suggests that the energy absorbed by these particles may be maximised by adapting their size to the asphalt gradation, so that it is equivalent to the size of the smallest aggregate in the solid skeleton.

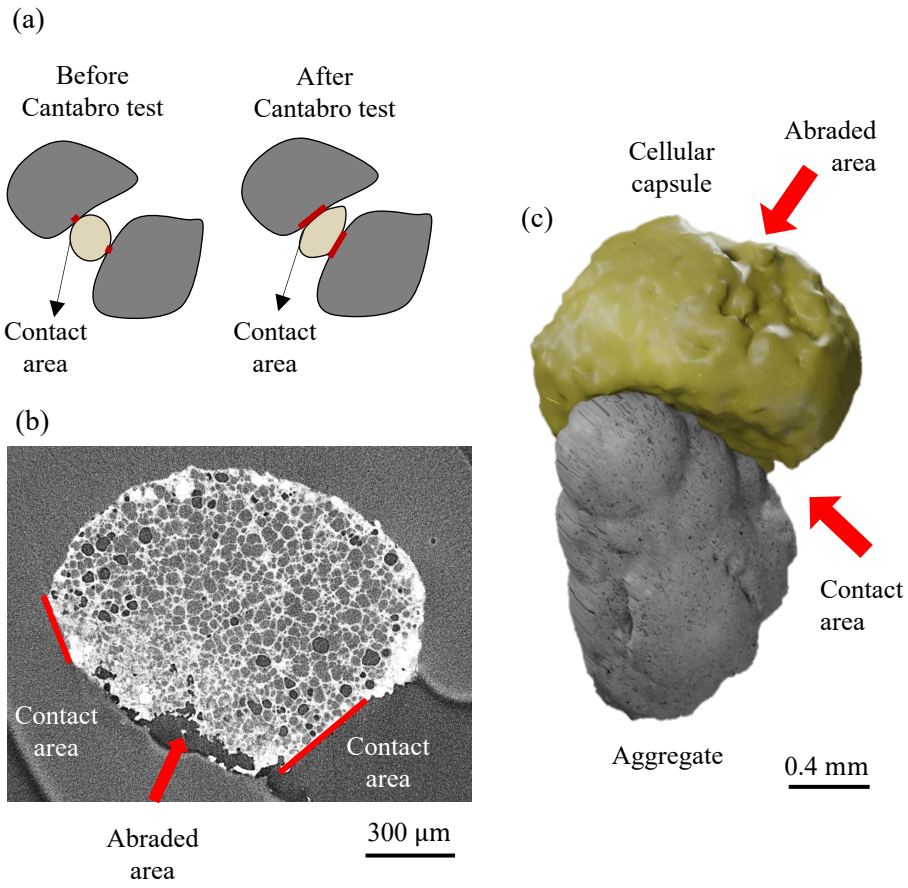


Figure 4.13. (a) Diagram of cellular capsule deformation under loading and interaction within the aggregate skeleton, (b) CT-scan of the top view of a cellular capsule extracted from a core specimen after the Cantabro test and, (c) reconstruction of a cellular capsule damaged by the aggregates after impact loading in the Los Angeles machine.

4.9 Assessment of Energy Absorption Under Loading

Figure 4.14(a) presents an example of a load-strain curve for a cellular capsule under compressive loading, in which three regions can be identified [191]: linear elasticity, collapse plateau and densification area. Under a moderate load, 20 N, the cellular particles showed linear elasticity, which may be explained by the bending and stretching of the cavity faces. After a yield load, the cells may have eventually collapsed, with the subsequent release of the enclosed oil. Lastly, the complete collapse of the cellular structure was followed by a densification region with a significant rise in stress, caused by the contact between the opposed faces of the cavities. The capsules' degradation mechanism prior to the collapse of the internal structure can increase the energy absorbed by the asphalt when it is subjected to

loading [191], as presented in Figure 4.14(b). Moreover, the energy absorbed by the asphalt under compressive loading increased linearly with the content of cellular capsules in the mixture, see capsules in Figure 4.14 (c). Thus, results from the aggregate loss test, where the mass loss decreased linearly as the content of cellular capsules increased, see Figure 4.3, may be justified by the energy absorbed by the cellular capsules in the asphalt under impact loading.

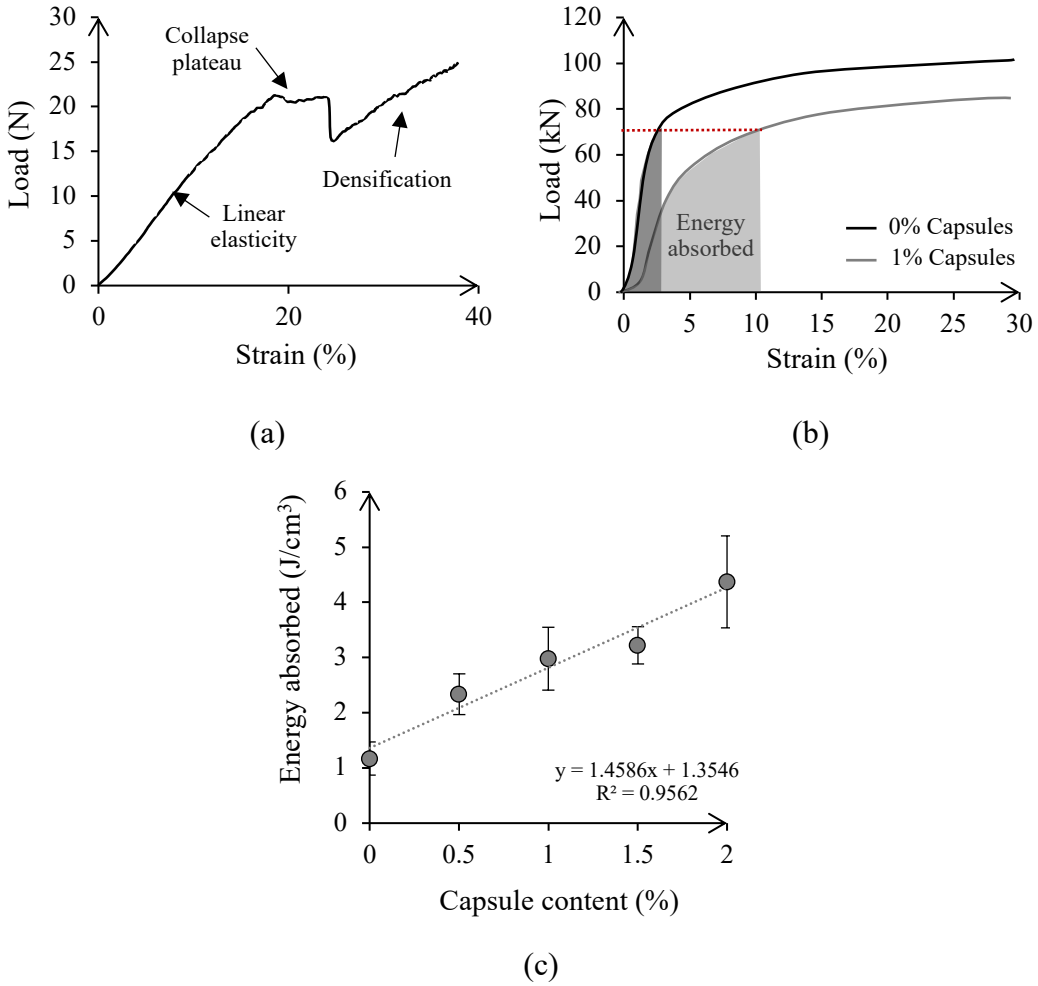


Figure 4.14. (a) Compressive load-strain diagram of a cellular capsule, (b) Compressive load-strain curve of asphalt containing 0% and 1% of cellular capsules (c) Energy absorbed by asphalt containing a range of percentages of cellular capsules under compression testing.

Previous research reported similar results: Ruiz-Riancho et al. [159] documented that the size and strength of the polymeric capsules were related to the release of the encapsulated rejuvenator. What is more, a higher amount of oil released was

associated with an increase of the cyclic loads resisted, which also increased rutting. In this study, changes in asphalt performance were associated with the release of the capsules' payload. Based on the conclusions of the current study, under cyclic loading, capsules may deform permanently due to their energy absorption capacity, promoting local compaction of aggregates. A greater deformation in the capsules may increase the durability of asphalt due to the absorption of energy and, consequently, the amount of oil released by the capsule.

Furthermore, Al-Mansoori et al. [25] developed a novel test method to measure the crack healing of asphalt beams containing capsules. It was found that asphalt beams broken into two pieces could recover most of their strength by compressing the two pieces and placing them together [167]. It was explained that the oil in the capsules would promote the drainage of bitumen in the crack; however, bitumen drainage might be justified by the capsules' deformation, which helped relocate the aggregates, increasing the pore pressure and promoting the draining of bitumen into the cracks, as presented in Figure 4.15.

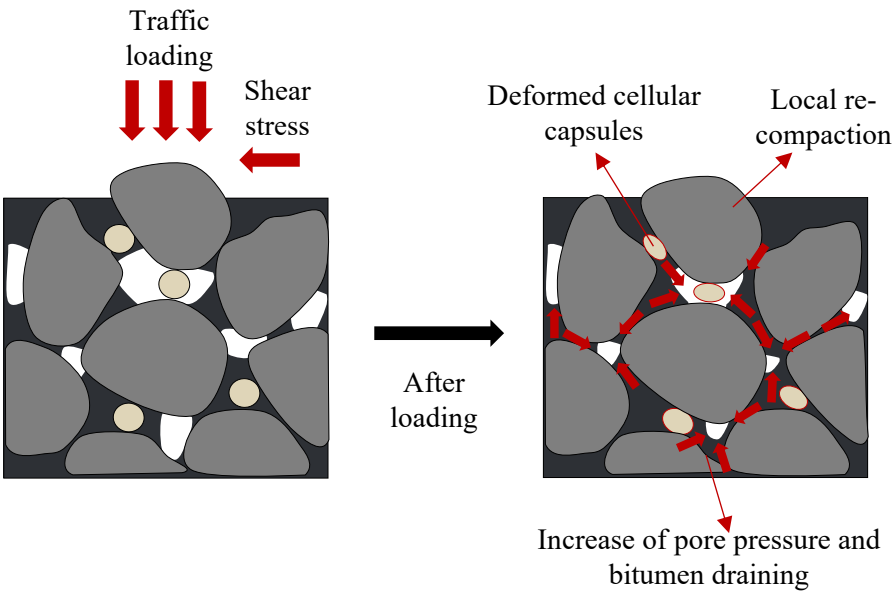


Figure 4.15. Action mechanism of the cellular capsules.

In addition, García-Hernández et al. [252] reported, that under cyclic loading, the release of oil was higher in stone mastic asphalt, compared to well-graded asphalt. SMA mixtures with capsules showed a higher self-healing level and greater compressive deformation compared to well-graded asphalt. This could have occurred due to the capsules being part of the solid skeleton in SMA, which may have contributed to deforming them. This finding is in line with the results presented in this study, where asphalt containing cellular capsules and a higher volume of voids showed more significant mass loss reduction compared to asphalt without cellular capsules.

Therefore, the key function of the cellular capsules might be to absorb the impact-load energy, deforming and causing the local re-compaction of aggregates, which increases asphalt durability, due to: (i) the cellular capsule deformation and, (ii) the subsequent local increase of pressure in the mastic, which makes it move within the pores in the solid skeleton, as summarised in [253]. This novel working mechanism could justify results from previous research that were explained as asphalt self-healing.

Chapter 5. Performance of Plant-produced Asphalt Containing Cellular Capsules

5.1 Introduction

This chapter assessed the influence of cellular capsules on the performance of asphalt manufactured at an industrial site. Based on the results from the previous chapter, in which the capsules were found to be more than just a rejuvenator release mechanism, the capsules were examined as cellular materials that, under loading, deform and absorb energy while they experience a progressive collapse of their porous structure. Therefore, the key variables during asphalt manufacturing that may affect their plastic deformation under loading were assessed as well to better understand the mechanisms underlying their deformation and their impact on asphalt's durability. This study was divided into the following phases:

- Phase 1: Upscaled manufacturing of cellular capsules and analysis of their physical and mechanical properties.
- Phase 2: Manufacturing of asphalt at an asphalt plant to evaluate the capsules' distribution and integrity after mixing using industrial processes. Thereafter, asphalt's stability, ravelling resistance, macrotexture, and void content were evaluated to determine whether the aggregate skeleton that characterizes SMA mixtures was affected by the deformation of the capsules.
- Phase 3: The results were corroborated with asphalt manufactured at the laboratory under controlled conditions, eliminating disparities in asphalt's performance caused by the large-scale production.
- Phase 4: FE modelling was used to verify findings from the testing campaign.

5.2 Physical and Mechanical Properties of the Cellular Capsules

The cellular capsules were characterized to determine the impact of the upscaled manufacturing methodologies on their physical and mechanical properties. The median diameter of a set of 50 capsules was 1.6 mm (Q2), and 50% of the ordered data set ranged between 1.4 mm (Q1) and 1.9 mm (Q3), as in [159]. The capsules presented an elongated shape, with a notably high median aspect ratio of 1.45 and circularity values below 1 (median of 0.88). The median volume of the equivalent ellipsoid was 1.7 mm^3.

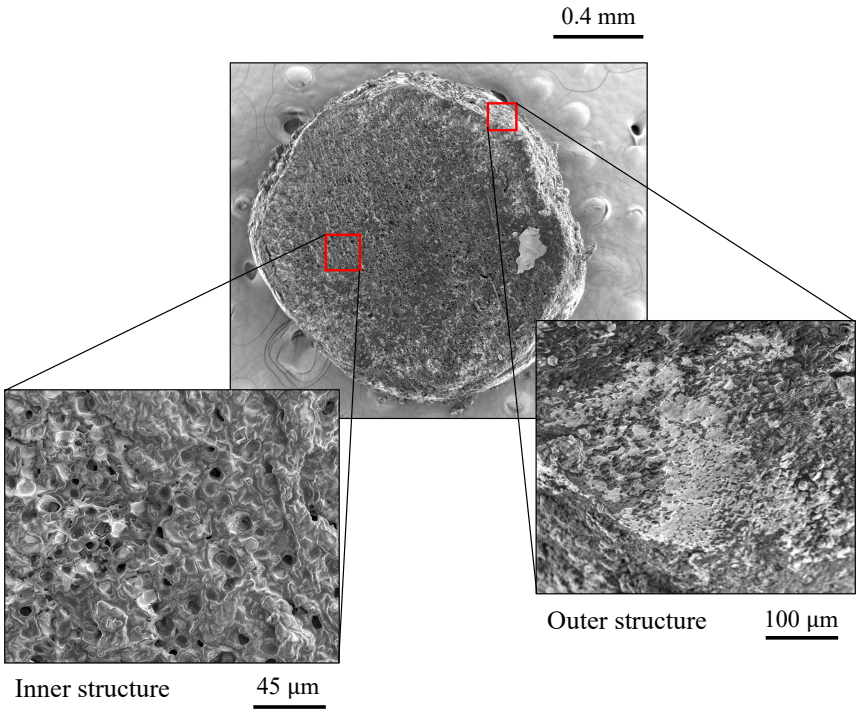


Figure 5.1. SEM images of the inner and outer structure of a bisected cellular capsule.

Figure 5.1 presents detailed views of the capsules' inner and outer structure. The external structure did not present any pores, whereas a porous matrix constituted the internal one with closed cells generated from cross-linking sodium alginate with calcium ions. The cellular capsules comprised 47.1% calcium alginate, 46.7% additive, and 6.2% air. The rejuvenator, which was used in prior research [[31],[157]], was enclosed in cavities of 4.9 ± 4.8 µm diameter (average ± one

standard deviation), while the confined air was in voids of about 3.3 ± 2.1 μm diameter.

Under compressive loading, the cellular capsules exhibited an elastoplastic behaviour. The average yield load of a sample set of 50 capsules was 9.5 N, in accordance with findings from [144], and was dependent on the diameter of the capsules, as described by a linear regression model ($y = 8.68d - 4.82$) with residuals normally distributed and a coefficient of determination (R2) of 0.75, that reported a meaningful level of predicted accuracy [254]. After yielding, the capsules showed strain hardening due to the plastic deformation. Lastly, rather than experiencing a brittle fracture, the internal microstructure showed in Figure 5.1 initiated a gradual collapse with the subsequent release of additive. The average Poisson ratio was 0.34, a similar value to gels, dental composites, and rubber [255].

5.3 Cellular Capsule Distribution and Integrity in Plant-Produced Asphalt Samples

Asphalt cores from asphalt produced at Mountsorrel Tarmac asphalt plant containing capsules were CT-scanned, see Figure 5.2, to evaluate not only if mixing at an asphalt plant could affect their distribution and integrity but also to evaluate at what stage of the mixing process capsules should be added. Although their distribution throughout the asphalt was generally uniform in the evaluated samples, see examples in Figure 5.2, some areas of the B4 batch (adding capsules at second 20 out of 27 seconds of mixing) had a higher concentration of capsules on the surface and centre of the scanned cores, suggesting that the mixing drum took longer to distribute the capsules properly. Further analysis reported an average number of capsules (± one standard deviation) per 3 mm of the height of 9 ± 4, 6 ± 4, 8 ± 6 in batch B2 (adding capsules to the aggregates), B3 (adding capsules at second 5 out of 27 seconds of mixing) and B4 (adding capsules at second 20 out of 27 seconds of mixing), respectively. Undamaged capsules represented about 88 ± 3% of the total volume of capsules in batch B2, 85 ± 5% in batch B3, and 96 ± 1% in batch B4. Their morphology was not affected by the mixing process, as the capsules displayed similar median aspect ratio and circularity values as loose capsules (AR of 1.45, circularity of 0.92).

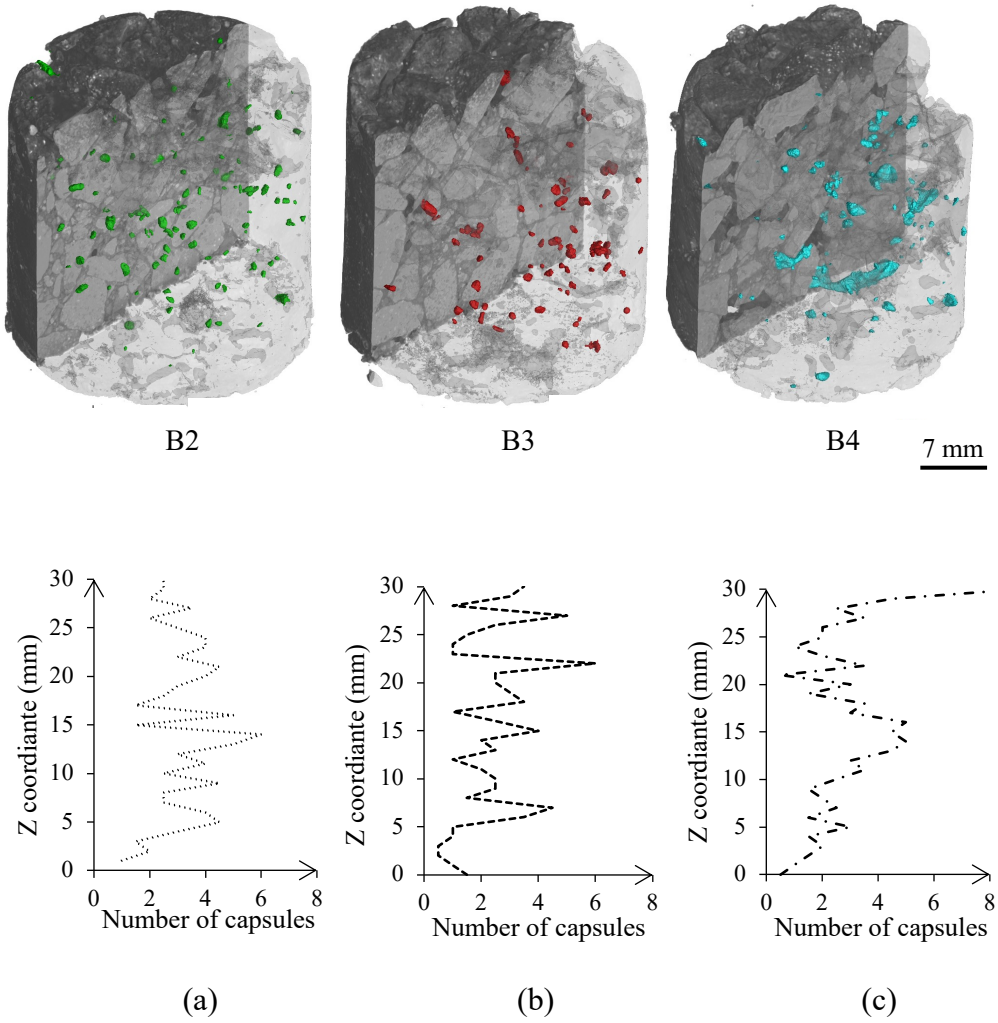


Figure 5.2. 3D reconstruction of plant-produced asphalt specimens containing cellular capsules, and average number of capsules per mm of height, from batches: (a) B2, (b) B3, (c) B4.

No more than 15% of the capsules were affected by the mixing process at an industrial scale. Moreover, adding the capsules at the end of the mixing resulted in less probability of damage, but also in a poorer distribution. Lastly, no traces of calcium alginate were identified in the FTIR analysis of the bitumen after mixing and compacting the asphalt, suggesting that the calcium alginate did not dissolve or intimately mix with bitumen.

5.4 Characterization of Plant-Produced Asphalt

The composition of plant-produced asphalt can be prone to a certain variability associated with the technologies employed to dry the aggregates and dose the materials. Therefore, prior to asphalt's evaluation under impact loading (Cantabro test) and cyclic loading (Hamburg wheel-tracking test), asphalt produced at Mountsorrel Tarmac asphalt plant was subjected to a compositional analysis to detect any inconsistencies, and the semi-circular bending testing was performed to assess whether disparities in asphalt composition might impact its performance.

Table 5.1. Compositional analysis of asphalt manufactured at Mountsorrel Tarmac asphalt plant.

Sieve size		**% Passing**			
		B1	**B2**	**B3**	**B4**
14	mm	100	100	100	100
10	mm	96	95	94	96
8	mm	74	74	62	62
6.3	mm	43	48	29	29
4	mm	26	33	16	15
2	mm	17	23	12	11
1	mm	12	15	9	9
0.5	mm	10	12	8	7
0.25	mm	9	11	7	6
0.125	mm	8	9	7	6
0.063	mm	7	8	6	5
Binder (%)		5.7	6.9	4.8	4.1

Based on Table 5.1, significant variations were found in the binder content, outside the 6.4% target by up to 2.3%. However, these variations may not have prevented a homogeneous distribution of the capsules during asphalt mixing, see Figure 5.2. According to the results from the semi-circular bending test, see Figure 5.3, batch B2 exhibited the highest fracture toughness, while batches B1, B3, and B4 presented similar fracture resistance values. Furthermore, as reported by [256], asphalt resistance to cracking severely decreased in batches with a higher percentage of voids. No outliers were found in the data sets, and further statistical analysis (Student t-test) revealed that B2 void content and fracture toughness were significantly

different from batches B1, B3, and B4 (p-value < 0.05). Hence, these results indicate that asphalt's composition must be considered when evaluating the performance of the plant-produced asphalt batches.

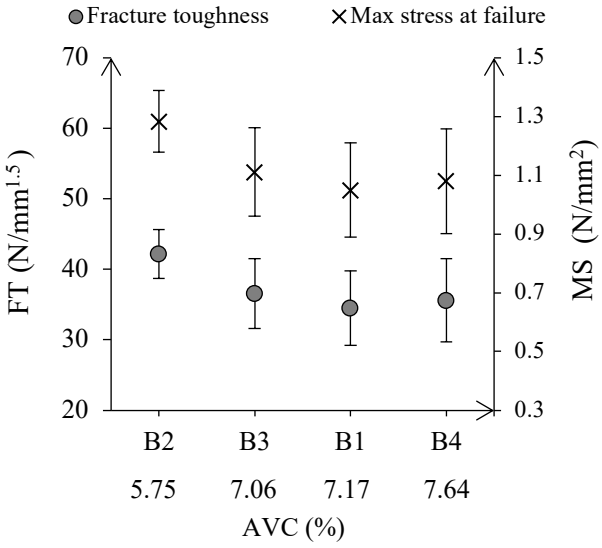


Figure 5.3. Results from semi-circular bending test and Air Void Content (AVC) calculations of asphalt manufactured at Mountsorrel Tarmac asphalt plant.

5.5 Evaluation of Plant-Produced Asphalt Performance

Due to the capsules' cellular nature and their ability to deform and absorb energy, there was no assessment of asphalt's crack-healing. Instead, asphalt's loss of stones, resistance to plastic deformations and macrotexture measurements were evaluated to determine if the aggregate skeleton that characterises SMA mixtures was affected by the deformation of the capsules under cyclic and impact loading.

The Cantabro test showed a reduction of the aggregate loss in asphalt containing capsules of 49% and 12% in batches B2 and B3, as shown in Figure 5.4(a), whereas it increased by 25% in batch B4. However, based on asphalt's characterization from Section 4.3, these results were highly influenced by variations in the binder dosing, as shown in Figure 5.4(a), in which a power law was fit with a coefficient of determination of 0.98. Besides, the percentage of coarse aggregates lost increased with the mass loss, as presented in Figure 5.4(b).

Furthermore, FTIR analysis of the recovered binder revealed that, during testing, the capsules released about 66.8% and 62.5% of the additive in batches B4 and B3, and 48.0% in batch B2. These results suggest that the capsules experienced a plastic deformation that yielded in a release of additive during testing. Additionally, the high release of additive in batch B4 could have been influenced not only by the binder dosing, but also by the mixing process, as the 3D reconstruction of batch B4 (Figure 5.2) showed some areas with a higher concentration of capsules, that might have facilitated their deformation and release of additive.

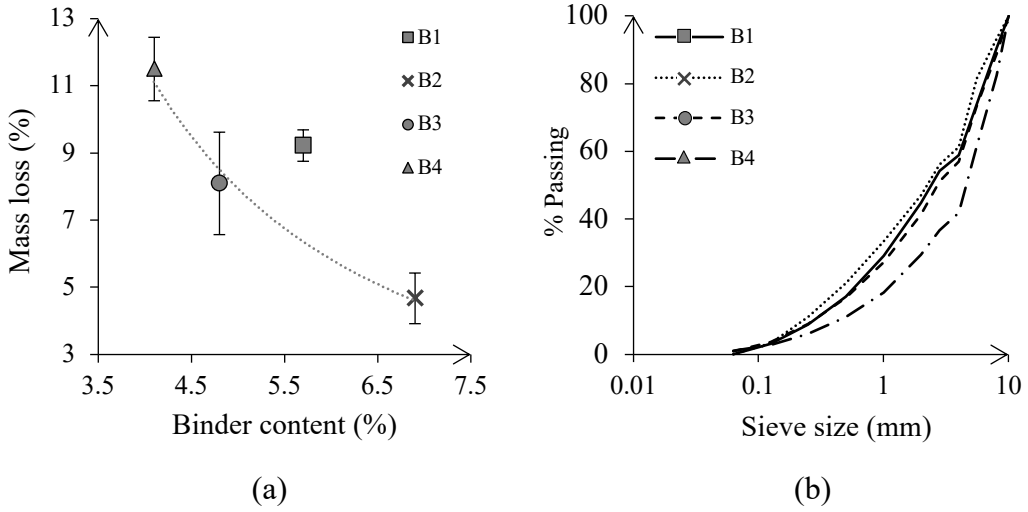


Figure 5.4. Results from the Cantabro test: (a) Percentage of mass loss and (b) aggregate gradation of the lost aggregates.

All four asphalt mixtures showed a proportional rut depth below 5%, or 2.55 mm after wheel-tracking, as presented in Figure 5.5(a). The highest plastic deformation was reached in asphalt batches B3 and B4, which contained capsules but also presented the lowest binder content. Therefore, the differences in the binder dosing reported in the previous section may have affected the deformation of the capsules under cyclic loading. Additionally, asphalt's macrotexture measurements before testing showed higher MPD values on samples containing capsules: B1, 1.43 mm; B2, 1.45 mm; B3, 1.57 mm; B4, 1.50 mm. After testing, the MPD was increased by an average of 2% due to the wheel that, during testing, wore away the initial thick film of binder, see Figure 5.5(b).

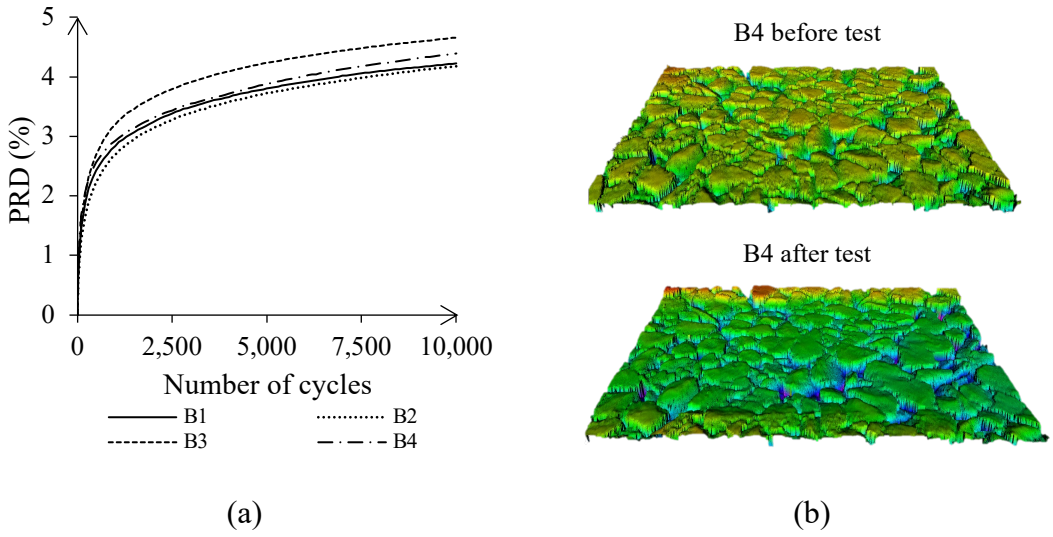


Figure 5.5. (a) Proportional rut depth of asphalt samples after wheel/tracking and (b) reconstruction from the scanned lines of a specimen in the mid-centre before (MPD of 1.50 mm) and after (MPD of 1.56 mm) wheel tracking.

There is no clear indication of whether the industrial plant's mixing stage affects the capsules' ability to deform and absorb energy. Additionally, disparities in binder dosing affected asphalt's performance, but their influence on the deformation of the capsules could not be quantified. Hence, a laboratory validation under controlled conditions is required to assess separately the effect of the capsules on asphalt performance when modifying: (i) the mixing stage in which they are incorporated, (ii) the binder content of the batch.

5.6 Validation of Results at the Laboratory Scale: Effect of Mixing Time

In light of the results from Section 5.5, an equivalent SMA mixture with 0% and 0.5% of cellular capsules was manufactured at lab-scale (mixture M7 from Table 3.4), to determine if the mixing time might have affected the capsules' performance. The capsules were added at different stages of the mixing process, as defined in Table 3.6, and the test results from mechanical testing and morphological assessments are summarized in the following table (Table 5.2):

Table 5.2. Testing of lab asphalt mixtures varying the mixing process on asphalt containing cellular capsules.

Property measured	0% capsules	0.5% capsules				
		Mixing time (%)				
		0%	20%	50%	75%	83%
Air Void content (%)	8.20	6.69	8.25	7.62	6.96	7.86
Standard deviation	0.35	0.32	0.35	0.42	0.06	0.12
Mass loss (%)	5.43	3.39	3.31	2.84	4.03	4.10
Standard deviation	0.42	0.53	0.69	0.82	0.61	0.35
Proportional rut depth (%)	4.93	4.90	4.28	3.88	3.92	4.27
Standard deviation	0.92	0.73	0.14	0.34	0.10	0.77
MPD before testing	0.96	0.89	0.91	0.90	0.88	1.02
MPD after testing	1.05	0.97	0.88	0.99	0.90	0.97

Although the volume of voids and the particle loss decreased in asphalt samples containing capsules, no evidence of a correlation between these parameters and variations in the mixing process was found. A Student t-test revealed that samples containing 0% and 0.5% of capsules presented substantially different mass loss results after conducting the Cantabro test (p-value < 0.05). Besides, adding the capsules at 50% of the mixing process or before reduced the mass loss by an average of 38%, compared to an average reduction of 25% when added after 50% of the mixing.

The proportional rut depth seemed to be reduced when adding capsules at about 50% and 75% of the mixing interval. An excessive mixing time might have released part of the additive, affecting the binder and hence also asphalt's permanent deformation. However, mixing at the end of the process may have left some areas with a higher concentration of capsules, as seen in the plant-produced asphalt CT-scans (Figure 5.2), increasing rutting. Lastly, asphalt macrotexture on samples without capsules had a steeper increase after wheel tracking, of about 9%, when compared to those containing capsules, whose MPD increased by an average of 3% but with no statistically significant differences when changing the mixing time of the capsules.

5.7 Validation of Results at the Laboratory scale: Effect of Bitumen Content Variations

Considering the results from Section 5.5, an equivalent SMA mixture with 0% and 0.5% of cellular capsules was manufactured at lab-scale (mixture M7 from Table 3.4), to determine if variations in the binder dosing might have influenced the capsules' deformation. Five asphalt mixtures were manufactured with different binder contents, and the test results are summarized in Figure 5.6.

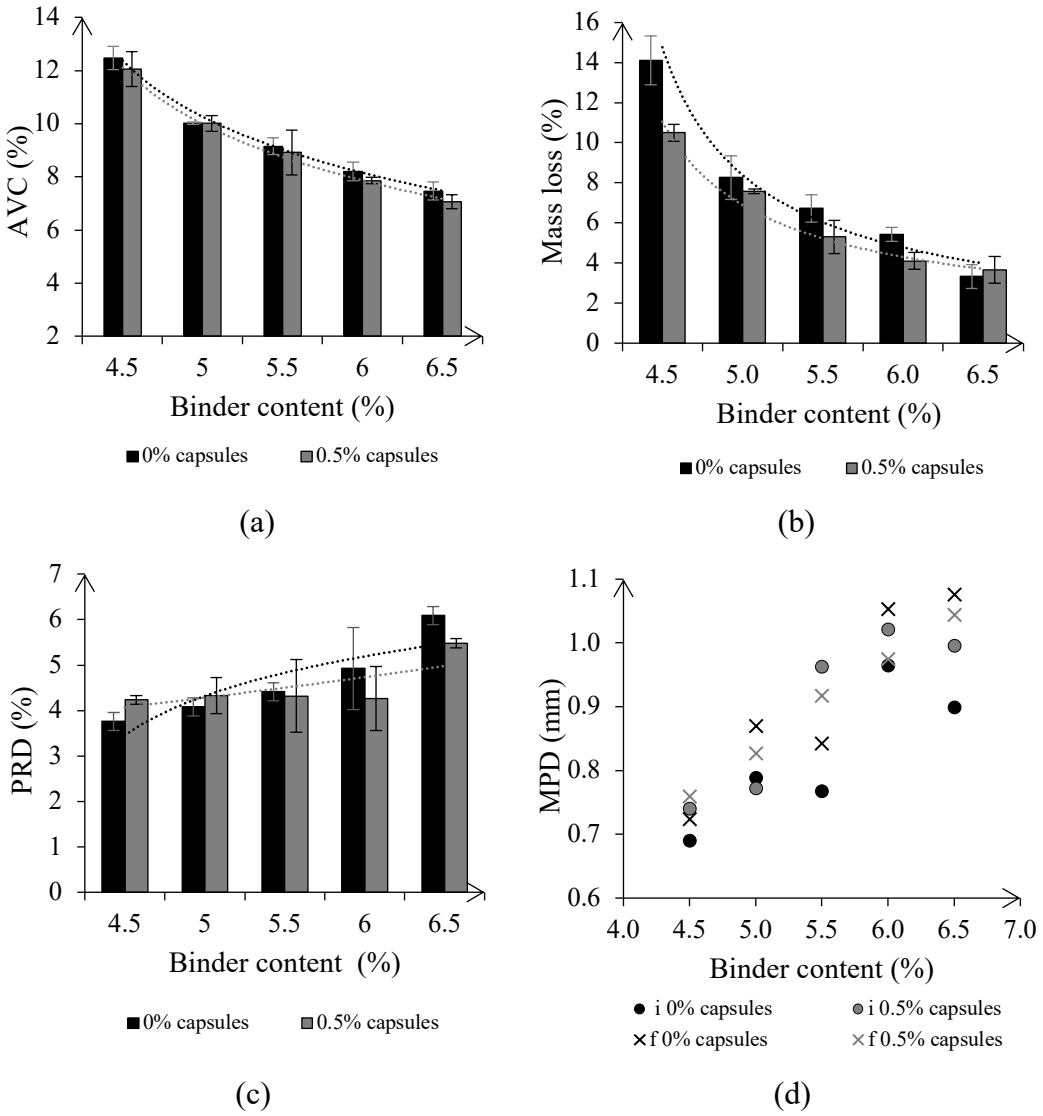


Figure 5.6. Testing of NTEC asphalt mixtures with different binder contents with 0% and 0.5% of capsules: (a) AVC, (b) ravelling resistance, (c) rutting resistance and (d) initial and final asphalt macrotexture during the Hamburg wheel tracking test.

Asphalt's AVC was barely affected by the presence of capsules, and decreased by approximately 3% on samples with capsules regardless of the bitumen content, as seen in Figure 5.6(a), which is in line with the results from the previous section, see Table 5.2. Moreover, Figure 5.6(b) shows that asphalt resistance to stone loss was highly dependent on the bitumen content, following a similar power law to that of Figure 5.4(a). The capsules exhibited a greater performance when reducing the binder content of the asphalt mixture, decreasing the loss of stones by up to 25% compared to asphalt without capsules, as presented in Figure 5.6(b). Besides, this finding suggests that when asphalt's binder content is increased, the cellular capsules' deformation and subsequent energy absorption may be limited. This may stem from the capsules being within the mortar fraction rather than constituting part of the aggregate skeleton.

Asphalt rutting increased with the bitumen content, as shown Figure 5.6(c). However, this increase was gradual in samples containing 0.5% capsules, whereas the development of plastic deformations was steeper in asphalt without capsules. As a result, asphalt's stability was improved by adding capsules for bitumen contents higher than 5%, matching the results obtained from the evaluation of plant-produced asphalt, see Figure 5.5, and the lab verification from the prior section, see Table 5.2. Under the test conditions, the capsules, which are prone to deformation, may act as a micro reinforcement of the mastic if there is a high bitumen content, improving the mixture's stability.

Besides, asphalt macrotexture was also affected by the addition of cellular capsules, as shown in Figure 5.6(d). Before wheel tracking, asphalt MPD values on samples containing capsules ranged between 0.75 mm and 1.05 mm, compared to 0.70 mm and 0.85 mm for asphalt without capsules. After testing, asphalt MPD on specimens with 0.5% of capsules fluctuated in the same range. In contrast, asphalt texture increased on samples without capsules, with an MPD varying from 0.77 mm to 1.09 mm, which was also observed in the lab verification from the prior section, see Table 5.2. According to [257], MPD values in asphalt with and without capsules are acceptable despite these variations. As asphalt's macrotexture contributes to water

evaporation on its surface [258], adding capsules will reduce the risk of aquaplaning in wet conditions.

5.8 Numerical Simulations Using FEM

The previous chapter evaluated the capsules as cellular materials that deform under loading, experiencing a progressive collapse of their porous structure that allowed them to absorb energy. In addition, the experimental campaign of this chapter revealed that their performance may be affected by the binder dosing in Sections 5.5 and 5.7. Hence, to supplement findings from experimental testing, Abaqus was used to model the deformation of a capsule between two stones when applying uniaxial compression, studying five scenarios in which the area of mastic surrounding the stone-capsule-stone matrix was progressively increased. Thereafter, a qualitative study was made by comparing the results from all the simulations.

The results of the simulations are presented in Figure 5.7. The model with the lowest volume of mastic, see Figure 5.7(a), showed the highest deformation of the capsule, with an aspect ratio of 1.35. Then, as the area of mastic was gradually increased in the subsequent simulations, the deformation of the capsule was also reduced, as shown by the reduction of the aspect ratio up to a value of 1.12 in the last simulation, see Figure 5.7(e). Therefore, this model provides some explanation of the test results from the particle loss in Figure 5.6(b), in which the performance of the capsules increased as the binder content was reduced and the stone-on-stone contact was enhanced, increasing their deformation and energy absorption when they form part of the aggregate skeleton.

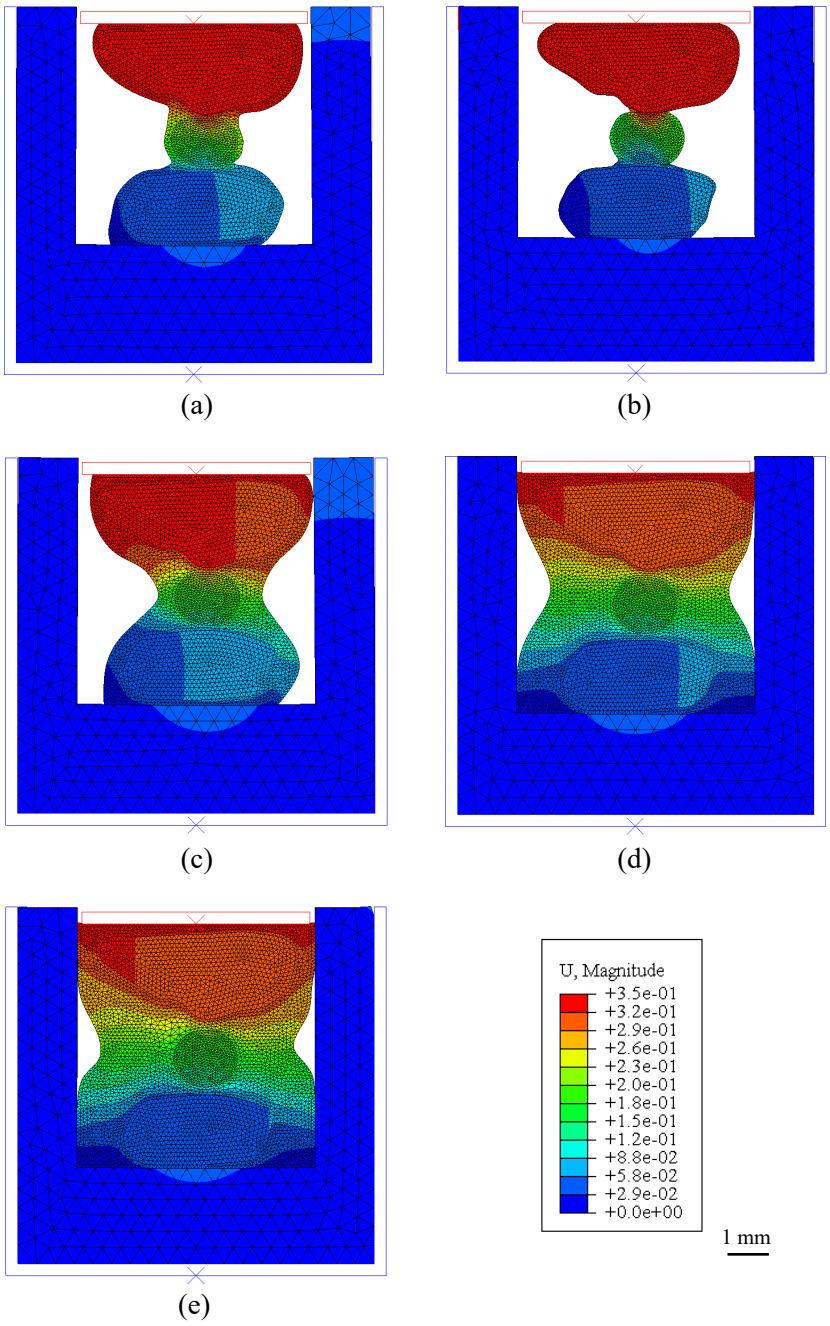


Figure 5.7. Total displacement U (in mm) in the FE model after applying uniaxial compression for the five variations in the case study altering the area of mastic. From (a–e), AR of the capsule after loading: 1.35, 1.30, 1.20, 1.14, 1.12.

Chapter 6. Evaluation of Lattice Metamaterials for Enhanced Asphalt Performance

6.1 Introduction

According to the results from the previous chapters, cellular capsules may induce physical changes in the aggregate skeleton of asphalt mixtures due to their energy absorption properties, ultimately affecting asphalt's durability and performance. To test this hypothesis, a fundamental study was conducted in this chapter, in which the use of lattice structures that absorb energy as an alternative to cellular capsules was evaluated as well due to the advantages they offer in the design, optimisation, and manufacturing processes. The study was divided into the following phases:

- Phase 1: During the first phase, diverse lattice structures were designed, 3D-printed, and mechanically characterised through uniaxial compression under a constant displacement rate. Two lattice structures with distinctly different mechanical properties were then selected for further evaluation in the second phase.
- Phase 2: Cellular capsules, spherical lattices and hard spheres with negligible energy absorption were tested in a granular unbound medium under static and cyclic compression loading. This fundamental study aimed to evaluate and compare the effect of the energy-absorbing particles on the overall response of the composite granular unbound medium, as well as the deformation of the particles and the crushing behaviour of the aggregates.

6.2 Characterization of Materials Used for MJF

Polyamides PA11 and PA12 gained significant popularity in power bed fusion techniques such as Multi Jet Fusion (MJF), and regardless of the similarities in their chemical structure, the two materials exhibit different mechanical properties [221]. Therefore, to compare their material properties, the mechanical performance of both polyamides was assessed through tensile testing, as presented in Table 6.1. With a Young's modulus of E=1209 MPa, PA12 was more prone to elastic deformations than PA11 (E=1402 MPa). However, PA11 exhibited greater ductility, reaching higher tensile stress values at break and a maximum elongation of 67%, whereas PA12 only attained 15% elongation before breaking.

Table 6.1. Results from tensile testing polyamides PA11 and PA12.

		PA11	**PA12**
E (MPa)	Average	1401.70	1208.72
	Standard deviation	80.82	16.43
Max stress (MPa)	Average	50.11	42.56
	Standard deviation	0.90	0.99
Max strain (-)	Average	0.67	0.15
	Standard deviation	0.07	0.02

6.3 Manufacturability of the Proposed Lattices

Despite the design constraints, the excellent printability of the selected polyamides, coupled with the great accuracy provided by the MJF 3D-printing technology, enabled the successful manufacturing of the designed lattice structures. However, local printing inaccuracies were identified in several walled TPMS and beam-based lattices, regardless of the polyamide used, as presented in Table 6.2. In the case of walled TPMS, surface points that did not attain the minimum thickness tolerance presented improper geometries, whereas some beam lattices yielded irregularities such as fused parts or imperfections at the end of the beams.

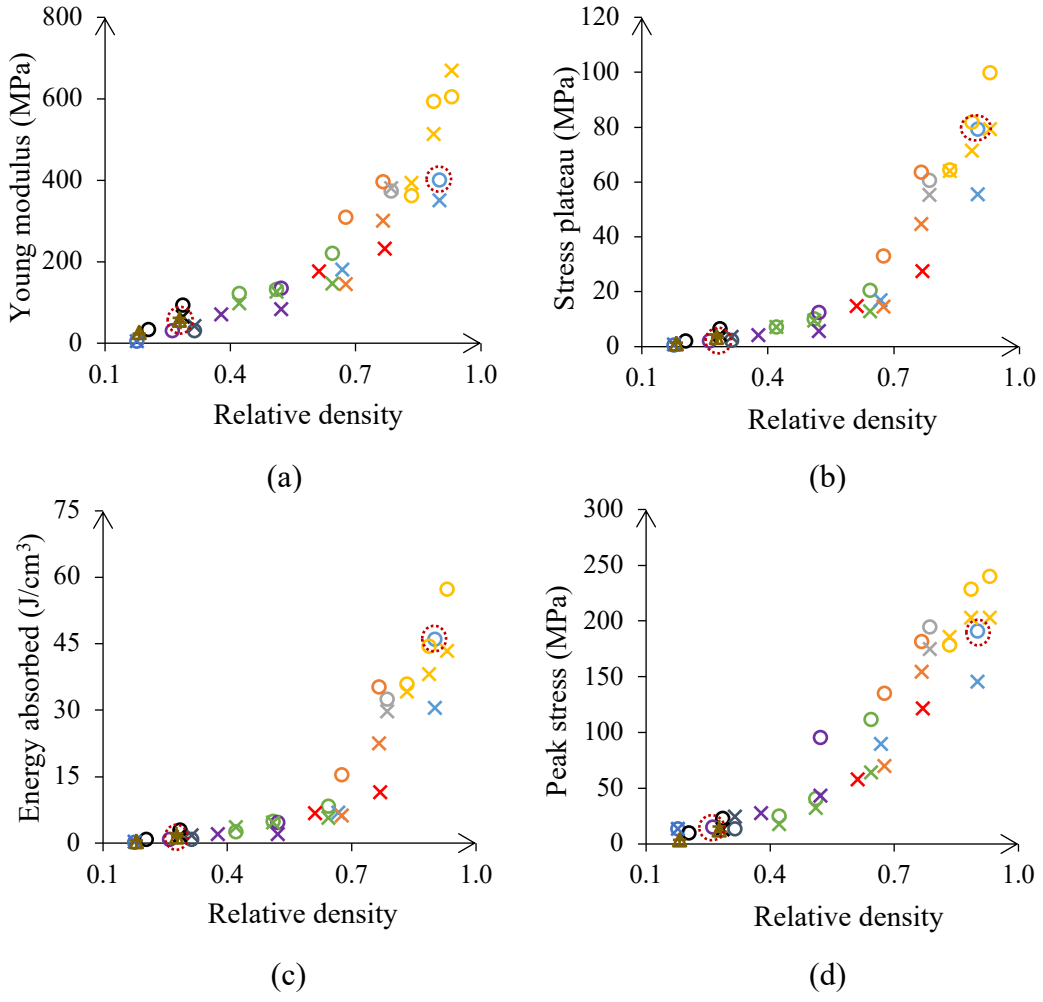
Table 6.2. Lattices discarded due to manufacturability (M) or integrity (I) issues, classififed by the material type (PA11or PA12), Unit Cell size (UC of 4mm, 5mm or 6mm) and type of unit cell.

Material	**PA11**	**PA11**	**PA11**	**PA12**	**PA12**	**PA12**
Cell size	**UC4**	**UC5**	**UC6**	**UC4**	**UC5**	**UC6**
Diamond	I	I	M			M
Gyroid						
Lidinoid		M	I		M	
Neovius						
Schwarz	M		M	M		M
Splitp	M			M		
BCC	M, I		I	M, I		I
Fluorite	M		M, I	M		M
Kelvin			I		I	I
Octet		I				I
Material	**PA11**			**PA12**		
Voronoi P20R1						
Voronoi P20R2	I			I		
Voronoi P40R1	I					
Voronoi P40R2						

6.4 Evaluation of the Lattice Mechanical Performance

Due to the large number of lattices tested, the evaluation of their mechanical properties focused on the main attributes that characterise their stress-strain curves, which were plotted against their relative densities, following the methodology used in prior research studies [259], based on the Ashby plots [192]. Lattices that presented manufacturability difficulties were not included in this assessment, see Table 6.2, not only due to the inconsistent results they might lead to during their mechanical characterisation, but also because of the discrepancies between the original design and the 3D-printed lattices [200], which might compromise the use of numerical modelling for further evaluation and optimisation in future research. Moreover, lattices that fragmented into several pieces during mechanical testing were also discarded from further evaluation, see Table 6.2, to reduce the likelihood of particle breakage within the asphalt mixture, which must be composed of a durable granular medium resistant to fragmentation.

The test results are summarised in Figure 6.1, and Table 6.3 provides a Pearson correlation matrix evaluating the selected parameters. In the linear elastic region of the stress-strain curves, the Young modulus exhibited a wide range of values, from 5 to 670 MPa (Figure 6.1(a)), as well as the average stress in the plateau region, which ranged from 1.3 to 99MPa (Figure 6.1(b)), and the energy absorbed until the end of the plateau region, which variated from 0.6 to 60.9 J/cm^3 (Figure 6.1(c)). Similarly, the peak stress at the maximum strain also covered a wide range of values, from 3.85 to 240 MPa (Figure 6.1(d)). These four parameters were highly associated with the relative density of the lattices, as revealed by the Pearson correlation coefficients from Table 6.3.



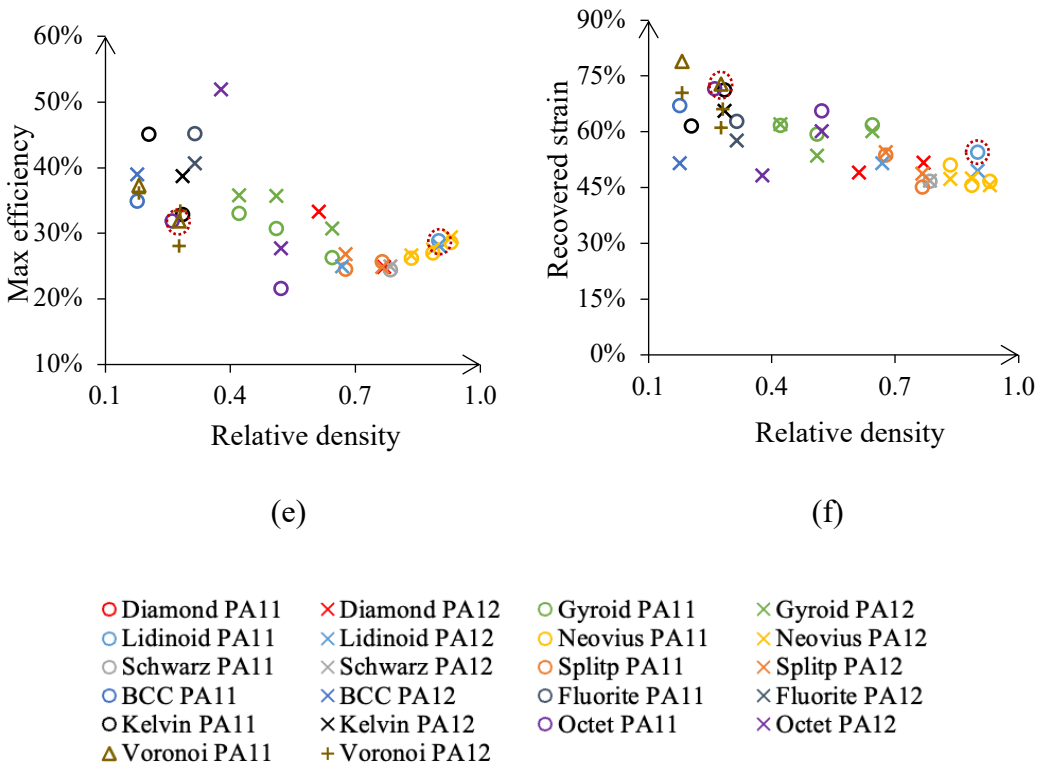


Figure 6.1. Results from uniaxial compression of the lattices, and selected lattices for further evaluation: (a) Young modulus, (b) average stress plateau, (c) energy absorbed, (d) peak stress, (e) maximum efficiency and (f) recovered strain.

Similar results were obtained in diverse research studies, in which it was acknowledged through the definition of scaling laws for each cell geometry [260] the relationship between the relative density of lattice structures and the mechanical properties extracted from the compressive stress-strain graphs, for both TPMS [261] and beam-based lattice structures [259]. However, the scaling laws do not isolate the effect of cell geometry from the relative density (also affected by the thickness of the beams/walls), which was also reported to affect the energy absorption properties of the lattices [[262],[212]]. Regarding the selection of materials for MJF, although the overall lattice performance was similar for both PA11 and PA12, lattices manufactured with PA11 exhibited higher elastic modulus and stress values, which is aligned with the behaviour of the parent materials observed during tensile testing, that determine the baseline properties of the lattices [193] , see Table 6.1.

Nonetheless, the magnitude of the correlation between the maximum efficiency and the recovered strain with the relative density of the evaluated lattice structures was found to be lower, as presented in Table 6.3. Besides, Figure 6.1(e) and Figure 6.1(f) illustrate that, as the difference between the density of the lattice and its corresponding parent material grew, the dispersion in the test results increased as well. This indicates that the relative density is not the main parameter governing those mechanical properties, and thus, geometric properties inherent to each type of lattice cause a non-negligible effect on the lattice efficiency and recovered strain. Similar test results were obtained in [263], in which the efficiency in the energy absorption of several beam-based lattices printed with different AM processes yielded efficiency indexes in the same range of values (30-45%) without discerning a clear correlation with the relative density.

Lastly, the influence of the type of polyamide was almost negligible for lattices with relative densities above 0.7, as shown in Figure 6.1(e) and Figure 6.1(f), whereas below that range, lattices manufactured with PA11 exhibited greater recovered strain and lower efficiency in the energy absorption when compared to those manufactured with PA12.

Table 6.3. Pearson correlation coefficients of the relationships between the evaluated variables used to characterise the mechanical performance of the lattices.

	Relative density	**Young modulus**	**Energy absorbed**	**Stress plateau**	**Peak stress**	**Max efficiency**	**Recovered strain**
Relative density	1.00	0.91	0.86	0.89	0.93	-0.67	-0.79
Young modulus	0.91	1.00	0.96	0.97	0.96	-0.56	-0.74
Energy absorbed	0.86	0.96	1.00	1.00	0.95	-0.51	-0.71
Stress plateau	0.89	0.97	1.00	1.00	0.97	-0.54	-0.72
Peak stress	0.93	0.96	0.95	0.97	1.00	-0.65	-0.76
Max efficiency	-0.67	-0.56	-0.51	-0.54	-0.65	1.00	0.32
Recovered strain	-0.79	-0.74	-0.71	-0.72	-0.76	0.32	1.00

6.5 Lattice Selection for Testing in a Granular Medium

The selected 3D-printing technologies allowed the successful manufacturing of lattice structures with a wide range of geometrical and mechanical properties from the same parent materials, as shown in Figure 6.1, although several lattices were discarded from further evaluation due to printing inaccuracies after manufacturing or integrity issues during uniaxial compression, see Table 6.2. Based on the results from Table 6.3, which identified a high correlation between the relative density of the lattices and four out of six parameters characterising their mechanical behaviour, the relative density was divided into two centred intervals, [0.20, 0.45] and [0.65, 0.90], aiming to select for further evaluation two lattice structures with distinct mechanical behaviours and thus, conduct a more comprehensive analysis.

In the first interval, the maximum strain recovery was prioritised, whereas in the second interval, the focus shifted towards optimising the efficiency in the energy absorption. Based on this screening criteria, the Voronoi tessellation ($\rho* = 0.28$, PA11), which recuperated about 73% of the strain after testing, and the Lidinoid ($\rho* = 0.9$, PA11), with exhibited a maximum efficiency in the energy absorption of 29%, see Figure 6.1, were selected for testing in a granular unbound medium, aiming to evaluate the feasibility of using lattice structures as an alternative to cellular capsules.

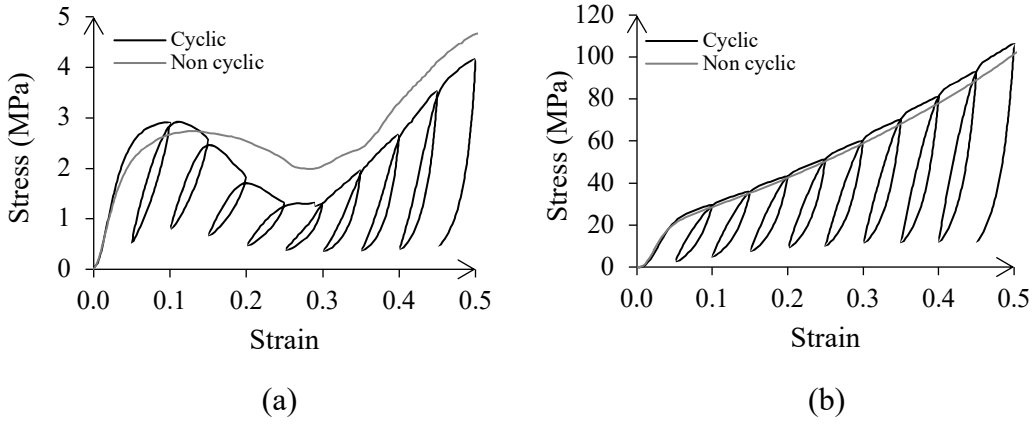


Figure 6.2. Compressive stress-strain curve and deformation during mechanical testing of the selected lattices made of PA11: (a) Voronoi with 40 points and randomness 2 and, (b) Lidinoid with a unit cell size of 4 mm^3.

Prior to this fundamental study, both lattices were subjected to cyclic uniaxial compression. Cubic samples were loaded under a constant displacement rate of up to 50% of strain, and for every 10% of strain, they were unloaded at the same displacement rate until reducing the vertical strain by 5%, generating with this loading-unloading profile the hysteresis loops depicted in Figure 6.2. The deformation characteristics of the Voronoi tessellation were affected under repeated loading conditions, as depicted in Figure 6.2(a), resulting in a reduction of its bearing capacity.

This might be attributed to the accumulated damage in the lattice structure, as the bending stresses in the struts initiate and propagate cracks which can be discerned in Figure 6.3, caused by the cell topology that significantly affects the fatigue properties of the Voronoi lattice, as reported by [200]. In contrast, the Lidinoid lattice displayed minimal differences in the stress-strain curve under cyclic loading, see Figure 6.2(b), exhibiting consistent behaviour on the hysteresis loops, which reveal a constant energy dissipation capacity.

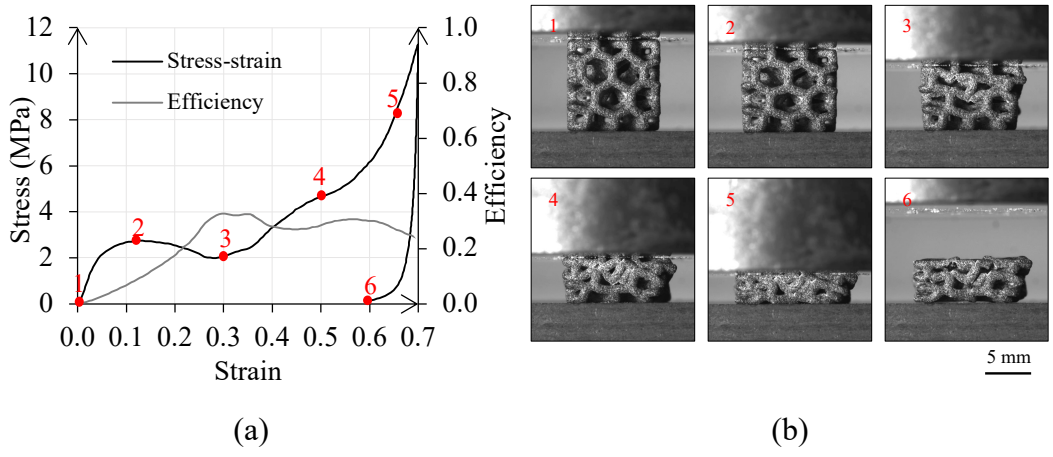
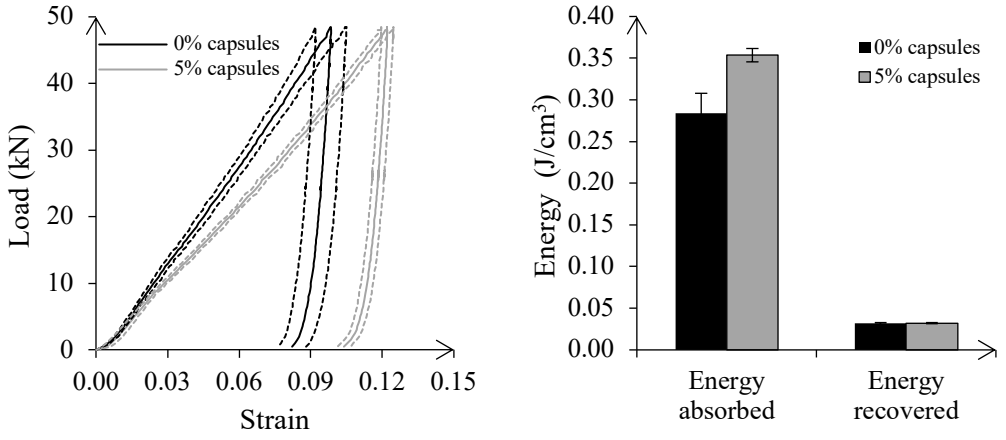


Figure 6.3. Stress-strain and efficiency-strain graphs of a Voronoi lattice under uniaxial compression (a), with (b) photographs taken at different strain levels during testing.

6.6 Mechanical Response in a Granular Unbound Medium

In previous chapters, it was suggested that under loading, the cellular capsules deform in the contact areas with the aggregates, adapting their geometry to the surrounding aggregate skeleton while absorbing energy, inducing a local re-compaction. But also, the binder content in the asphalt mixture may affect the capsule's ability to undergo deformation. Therefore, a fundamental study was conducted to evaluate the lattice's deformation behaviour in a granular unbound medium (with single size aggregates), to reduce the variability associated with the presence of the binder on the lattice's deformation behaviour, as well as the potential challenges that may arise during the mixing process.

The test results from evaluating the mechanical response of the granular unbound medium with and without energy-absorbing particles under a constant displacement rate are presented in Figure 6.4. Single-size aggregates of 1-2 mm attained an average strain at the end of loading of 9.8%, as depicted in Figure 6.4(a), which increased up to 11.9% when capsules were incorporated into the granular medium, increasing the energy absorbed by 24%, as shown in Figure 6.4(b). However, as shown in Figure 6.4(a), the unloading force-strain curves remained parallel regardless of the cellular particle content, with no discernible differences in the energy recovered, as seen in Figure 6.4(b).



(a) (b)

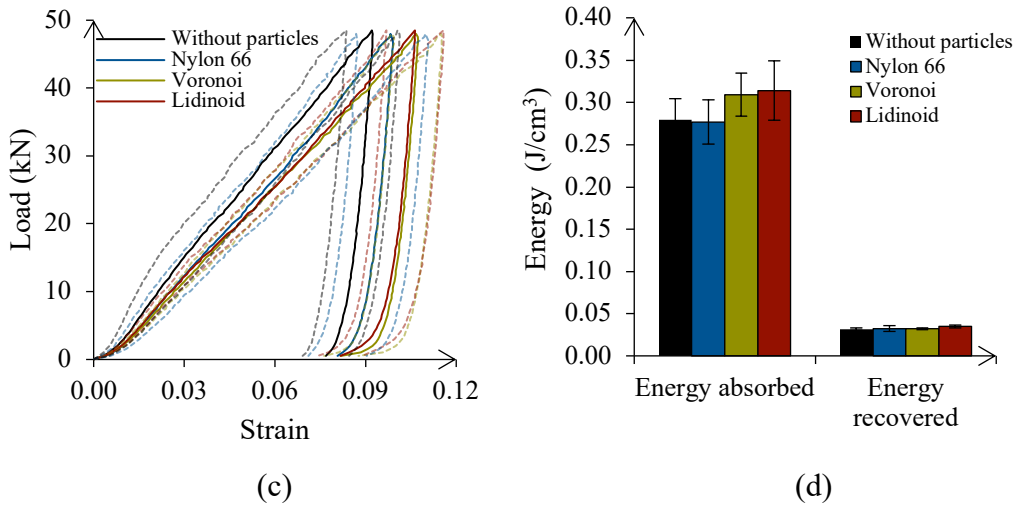


Figure 6.4. Testing of the granular unbound medium under uniaxial compression: (a) Load -strain curves on samples containing cellular capsules, (b) energy absorption on samples containing cellular capsules, (c) load-strain curves on samples containing spherical lattices and (d) energy absorption on samples containing spherical lattices.

Moreover, when evaluating the results of the 8-10 mm aggregates without any particles, both the average maximum strain after loading (approximately 9.2%) and the energy absorbed (0.28 J/cm^3) were similar to those seen on the 1-2 mm aggregates, as shown in Figure 6.4(c) and Figure 6.4(d). Samples containing Voronoi and Lidinoid lattices yielded a similar response, increasing the total strain after loading to approximately 10.6%, see Figure 6.4(c), and the energy absorbed to 0.31 J/cm^3, although a significative overlapping in the standard deviations was observed in Figure 6.4(d). Lastly, the mechanical response of this granular medium was further evaluated by introducing spheres made of Nylon 66 (maximum stress of 80 MPa under tensile testing [264]) to assess the effect of introducing spherical-non deformable particles on the 8-10 mm granular medium. However, no differences were observed in the energy absorption of tested specimens with and without these spheres.

Therefore, to provide a more comprehensive examination, additional testing was performed under cyclic loading. Firstly, different cyclic loads were used on specimens with an aggregate size of 1-2 mm, with and without cellular capsules, to determine the optimum test parameters. Then, based on the results from Figure 6.5(a), a load of 50 kN was selected for further evaluation, see Figure 6.5(b), not only

due to the lack of overlapping in the maximum strain after testing samples with cellular particle contents of 0% and 5%, but also due to the increased difference in the deformation rate, which was found to be 80% higher on test specimens containing capsules subjected to a cyclic load of 50 kN.

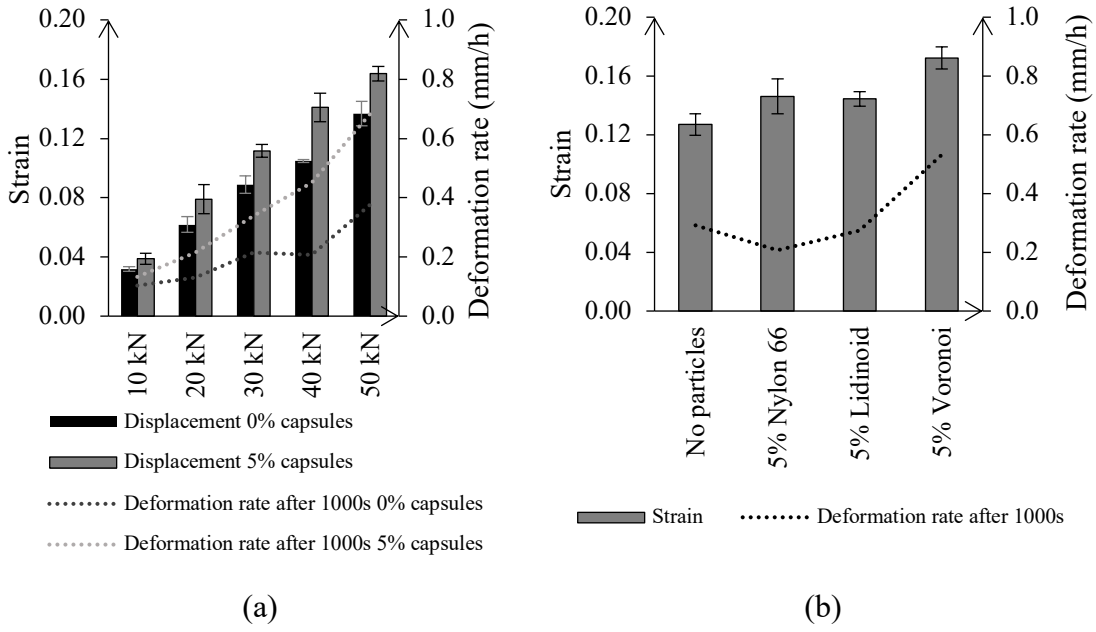


Figure 6.5. Testing of the granular unbound medium under cyclic loading on: (a) samples containing cellular capsules) and (b) samples containing spherical lattices.

Thus, results from Figure 6.5(a) seem to suggest that the addition of cellular particles affected the mechanical response of the granular medium under cyclic loading, due to their progressive deformation during testing, which increased as well the strain and deformation rate of the granular unbound medium. As to the test results on specimens with an aggregate size of 8-10 mm, the addition of Voronoi lattices increased the total strain of the granular medium, from 12% with 0% of particles to 17% in samples containing 5% of Voronoi lattices, see Figure 6.5(b). Besides, the displacement rate exhibited on samples containing Voronoi lattices increased by 80%, from 0.29 mm/h to 0.53 mm/h, showing a similar response to the addition of cellular capsules on the 1-2 mm granular medium. However, Lidinoid lattices barely affected the deformation rate of the granular medium, and the minimal impact they had on the total strain, see Figure 6.5(b), might be attributed to the presence of

spherical particles in the granular medium, as evidenced by the similar response showed by the spheres made of Nylon 66 in Figure 6.5(b).

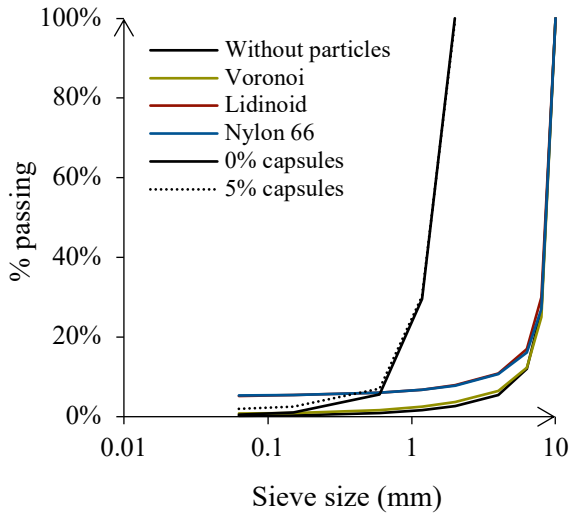


Figure 6.6. Particle Size Distribution (PSD) curves after uniaxial compression under cyclic loading.

To further support these findings, after cyclic testing the aggregates were sieved to evaluate the aggregate crushing, see Figure 6.6, and the deformation of the energy-absorbing particles was assessed as well through imaging techniques, see Figure 6.7 and Table 6.4. As to the Particle Size Distribution (PSD) curves, aggregates from samples that did not contain any energy-absorbing particles exhibited parallel curves that evidenced an equivalent behaviour. Besides, samples containing cellular capsules and Voronoi lattices did not show an increase in the percentage of crushed aggregates, see Figure 6.6. However, the PSD curves of samples containing Lidinoid lattices and Nylon 66 spheres displayed a different response, showing a higher proportion of crushed aggregates that might be caused by the presence of spheres that did not absorb any energy and, therefore, contributed to that increase in the fraction of crushed aggregates.

Table 6.4. Geometrical measurements of the evaluated energy-absorbing particles before and after testing in a granular unbound medium.

	Diameter (mm)			**Aspect Ratio (AR)**			**Circularity**		
	AVG	**SD**	**P-value**	**AVG**	**SD**	**P-value**	**AVG**	**SD**	**P-value**
Capsules									
Before	1.60	0.29	3.67E-06	1.31	0.22	7.59E-09	0.88	0.05	5.91E-16
After	1.77	0.27		1.54	0.35		0.81	0.08	
Voronoi									
Before	10.55	0.22	3.07E-30	1.05	0.03	6.49E-07	0.89	0.01	2.61E-02
After	8.99	0.63		1.12	0.06		0.88	0.04	
Lidinoid									
Before	10.50	0.18	4.47E-01	1.04	0.02	1.91E-01	0.90	0.00	3.69E-03
After	10.54	0.21		1.03	0.02		0.88	0.02	
Nylon 66									
Before	10.58	0.16	8.26E-01	1.04	0.03	8.52E-01	0.90	0.01	1.64E-02
After	10.59	0.26		1.04	0.02		0.90	0.00	

The main outcomes obtained from analysing the response of the granular medium under cyclic loading and evaluating the PSD curves of the aggregates were additionally supported by the assessment of the particle deformation in Table 6.4., through the measurement of the equivalent diameter, aspect ratio and circularity of the particles before and after testing. As shown in Figure 6.7(a) and Figure 6.7(c), both cellular capsules and Voronoi lattices showed deformed particles after testing, and the shape descriptors used in Table 6.4 depicted sample sets statistically different before and after testing (P-value < 0.05). Lidinoid lattices and Nylon 66 spheres, however, did not evidence signs of a noteworthy deformation in Figure 6.7(b) and Figure 6.7(d), or statistically significant changes on the shape descriptors evaluated in Table 6.4.

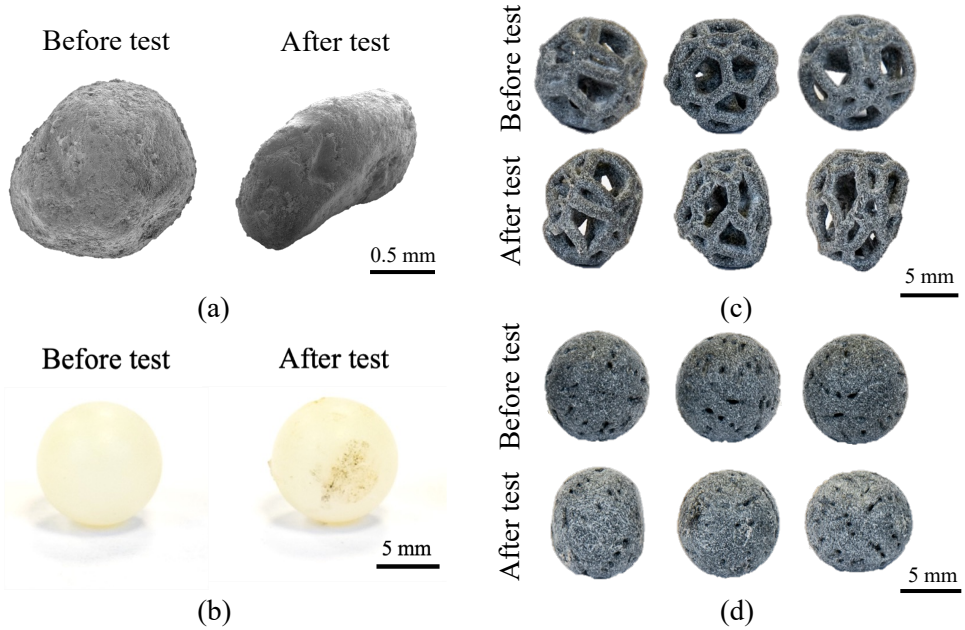


Figure 6.7. Evaluated energy-absorbing particles before and after testing, including: (a) Images of the cellular capsules using the ESEM, (b) photographs of PA66, (c) photographs of Voronoi lattices and (d) photographs of Lidinoid lattices.

Chapter 7. Conclusions

7.1 Conclusions

The previous chapters discussed the studies that were conducted as part of this research, based on the aims and objectives that were initially defined. As past research focused on evaluating the release and diffusion of the encapsulated rejuvenator and estimating the self-healing of asphalt cracks, in Chapter 4 the focus shifted towards evaluating the influence of the cellular capsules on the mitigation of asphalt ravelling, which is, along with asphalt cracking, one of the most prevalent distresses on the road network. After investigating the impact of the capsules on the aggregate loss and assessing the changes in their internal porous structure under loading, it was found that the capsules are more than a release mechanism, and their cellular structure experiences a progressive collapse under impact-loading while absorbing energy, which may cause a local re-compaction in the asphalt mixture.

Therefore, Chapter 5 focused on evaluating the influence of the cellular capsules on the performance of plant-produced asphalt, as well as evaluating variables throughout asphalt manufacturing that may affect the mechanisms governing their plastic deformation. It was found that, to maximize their energy absorption, the cellular capsules must be part of the aggregate skeleton. Lastly, in Chapter 6, this hypothesis was tested through a fundamental study in a granular unbound medium, and this study also evaluated the use of lattice structures that absorb energy as an alternative to the cellular capsules due to the advantages they offer in the design, optimisation, and manufacturing processes.

The following sections provide a comprehensive review of the main findings and conclusions of Chapters 4, 5, and 6.

7.2 Evaluation of Cellular Capsules to Mitigate Asphalt Stone Loss

This chapter investigated the use of cellular capsules on the mitigation of ravelling in asphalt mixtures, as measured by mass loss in the Cantabro test. Firstly, the capsule content for this study was selected based on results from aggregate loss, rutting and skid resistance testing. Then, to quantify the effect of the cellular capsules and investigate correlations, both compaction energy and asphalt gradation were varied. Lastly, asphalt mechanical properties under uniaxial compression testing were assessed to identify any changes induced by the cellular capsules, and both the particle deformation and asphalt's energy absorption were evaluated. Based on the results from this study, the following conclusions were obtained:

- The addition of cellular capsules to the asphalt increased the volume of air voids by up to 1.7%. This may be caused by the size of the capsules and the cellular capsule content, sufficient to cause changes in the asphalt morphology.
- As the percentage of cellular capsules in the mixture was increased, asphalt mass loss linearly decreased while the rut depth increased. Skid resistance values were not affected by any cellular capsule content. A content of 1% by weight of total asphalt mixture was selected for assessing ravelling because it reduced the mass loss by 30% without generating significant uncoated aggregates (stripping) in the wheel path after rutting testing.
- The Cantabro test results showed a rise in the mass loss when the compaction energy was reduced. In asphalt mixtures containing cellular capsules, the efficiency index of the capsules fluctuated between 13% and 25%. Cellular capsules may have contributed to reducing tensile stresses in the interfacial zone.
- The mass loss of asphalt showed a significant increase as the proportion of the largest aggregate was increased. In asphalt containing cellular capsules, the mass loss mitigation ranged from 24% to 30%. Cellular capsules may have reduced the shear stresses in the largest aggregates.

- There was a correlation between the efficiency index of the particles and the air void content of the asphalt mixture, suggesting that the volume of voids strongly influences the cellular capsules' effect on ravelling (mass loss) reduction.
- Under loading, cellular capsules deform and absorb energy. Increasing the percentage of cellular capsules in the asphalt mixture increased the energy absorbed by the asphalt. The deformation of the capsules, along with the subsequent increase of the pore pressure and bitumen flow, may locally re-compact the asphalt mixture, which helps increase its durability.

7.3 Performance of Plant-produced Asphalt Containing Cellular Capsules

In this chapter, the performance of plant-produced asphalt containing capsules was assessed, evaluating the capsules as cellular materials that deform and absorb energy rather than simply a means to release the rejuvenator. In addition, the variables during asphalt manufacturing that may affect their plastic deformation were evaluated as well. Firstly, the morphological and mechanical properties of SMA mixtures produced at Mountsorrel Tarmac asphalt plant were evaluated through experimental testing. The results were then contrasted with those obtained from testing equivalent mixtures manufactured at laboratory scale under controlled conditions. Lastly, a simplified FE case study verified the findings from experimental testing with a numerical simulation. As a result, the following conclusions were obtained:

- The capsules can be incorporated into an asphalt plant without compromising their integrity or their distribution within the asphalt.
- The mixing stage in which the capsules were incorporated during asphalt manufacturing did not yield significant differences in lab-produced asphalt's morphological and mechanical properties.
- The aggregate loss resistance increased in asphalt containing cellular capsules with the deformation of the capsules. Asphalt's stability was also affected by

the addition of capsules. Below a certain binder content, the capsules can deform and absorb energy, increasing rutting.

- Asphalt's macrotexture increased in asphalt containing cellular capsules. In this asphalt with capsules, the MPD was barely affected by the Hamburg wheel tracking test. Asphalt without capsules showed a substantial increase in its macrotexture after Hamburg wheel tracking testing.
- The mixture's binder content influences the deformation and energy absorption of the capsules. These need to constitute part of the stone-on-stone contact for maximising their deformation. If they are floating in mortar, they will reduce their performance or remain inactive.

7.4 Evaluation of Lattice Metamaterials for Enhanced Asphalt Performance

This chapter investigated the use of lattice metamaterials as potential alternatives to the cellular capsules used in asphalt mixtures for ravelling mitigation, with a specific focus on evaluating the physical impact of both the lattice structures and cellular capsules on asphalt's aggregate skeleton with a fundamental study. Firstly, the materials used for 3D-printing the particles were characterised through tensile testing, and then, the mechanical response of lattice metamaterials was evaluated through uniaxial compression testing. Lastly, the effect of the cellular capsules and the selected lattices on an unbound granular medium was assessed with a simplified study. This fundamental study encompassed the evaluation of the overall mechanical response of the granular medium containing particles under static and cyclic loading, as well as the crushing behaviour of the aggregates and the deformation of the energy-absorbing particles. Based on the results of this study, the following conclusions were obtained:

- Despite the limitations imposed by the design constraints, the selected 3D-printing technologies and materials allowed the successful manufacturing of the lattice metamaterials.

- Lattice metamaterials offer a wide range of mechanical properties, which can be tailored to meet specific requirements. Although there was a high correlation between the relative density of the lattices and their mechanical response, the maximum efficiency and the recovered strain were also influenced by the lattice design itself.
- The fundamental study in a granular unbound medium verified the physical influence of the cellular capsules on the aggregate skeleton, corroborating findings from prior research.
- The Voronoi lattice emerged as a noteworthy alternative to the cellular capsules, showing an equivalent particle deformation and mechanical response of the granular medium. Besides, 3D-printed lattice metamaterials offer advantages as to particle manufacturing using Multi Jet Fusion, and particle analysis and optimisation through numerical modelling.

7.5 Recommendations For Future Research

The following section provides guidance and recommendations for future research based on the conclusions drawn in the previous sections. The suggestions provide useful insight for future research to enable a more comprehensive assessment of the cellular capsules:

- Cellular capsules induce physical changes in the aggregate skeleton of the asphalt due to their energy absorption properties. In future research on cellular capsules, the focus should be shifted from investigating the release of the encapsulated rejuvenator and the effect of its chemical characteristics on asphalt self-healing to evaluating and optimizing the energy absorption of the capsules, with a particular emphasis on open-graded or gap-graded asphalt mixtures that rely on the stone-on-stone contact.
- It has been demonstrated that the production of capsules can be scaled up and that cellular capsules can be mixed with asphalt at an industrial scale without compromising their performance. Hence, it is possible to construct road

sections with and without capsules to monitor their condition and quantify the increase of asphalt's service life due to the action of the capsules.

- To evaluate the worthiness of the capsules as an additive that can increase asphalt's durability, the cost of manufacturing the capsules and the carbon emitted during their production should be considered, as well as the estimated service life of asphalt containing capsules and the maintenance needs over its lifespan. Therefore, the environmental sustainability of asphalt containing cellular capsules should be evaluated through a Life Cycle Assessment. Moreover, a Whole Life Costing (WLC) appraisal should also be considered in future research to determine if, in terms of Net Present Service Value (NPSV), asphalt containing capsules is an economically beneficial option.
- In this research, a fundamental study in a granular unbound medium identified noteworthy alternatives to the cellular capsules using 3D-printed lattice structures. However, it is essential to acknowledge the limitations of this fundamental study, which should be addressed in future studies. These include the influence of the forces and temperatures to which the lattice structures should be exposed during asphalt manufacturing on their physical and mechanical properties. It will also be crucial to investigate the response of lattice structures embedded in asphalt to loading under different load, temperature, and moisture conditions. Lastly, although the focus in this research was on 3D-printed lattice structures, the use of natural or synthetic foams as an alternative porous material should be considered as well in future research.

References

[1] C. A. O'Flaherty and A. Boyle, *Highways : the location, design, construction and maintenance of road pavements*. Oxford: Butterworth-Heinemann, 2002.

[2] N. Thom, *Principles of Pavement Engineering*. Thomas Telford Ltd, 2008. doi: 10.1680/pope.34808.

[3] C. Nicholls, 'Hot mix asphalt layers', in *ICE manual of highway design and management*, Thomas Telford Ltd, 2015.

[4] M. E. Nunn, 'Evaluation of stone mastic asphalt (SMA): A high stability wearing course materia', Transport Research Laboratory (TRL), PR 65, 1994.

[5] C. Miller, K. L. Vasconcelos, D. N. Little, and A. Bhasin, 'Investigating aspects of aggregate properties that influence asphalt mixture performance', The University of Texas, Austin, Research Report For DTFH61-06-C-00021, 2011.

[6] R. Hainin, W. F. Reshi, and H. Niroumand, 'The Importance of Stone Mastic Asphalt in Construction', *Electronic Journal of Geotechnical Engineering*, vol. 17, 2012.

[7] M. M. E. Zumrawi, 'Investigating causes of pavement deterioration in Khartoum State', *Int J Civ Eng Technol*, vol. 7, no. 2, pp. 203–214, 2016.

[8] J. Zhang, W. Huang, Y. Zhang, Q. Lv, and C. Yan, 'Evaluating four typical fibers used for OGFC mixture modification regarding drainage, raveling, rutting and fatigue resistance', *Construction and Building Materials*, vol. 253, p. 119131, 2020, doi: 10.1016/j.conbuildmat.2020.119131.

[9] T. Bennert and L. A. Cooley, 'Evaluate the contribution of the mixture components on the longevity and performance of FC-5.', Dept. of Transportation, Florida, No. BDS15 977-01., 2014.

[10] A. Abouelsaad and G. White, 'Review of Asphalt Mixture Ravelling Mechanisms, Causes and Testing', *Int. J. Pavement Res. Technol.*, vol. 15, no. 6, pp. 1448–1462, 2022, doi: 10.1007/s42947-021-00100-7.

[11] K. R. Opara, M. Skakuj, and M. Stöckner, 'Factors affecting raveling of motorway pavements—A field experiment with new additives to the deicing brine', *Construction and Building Materials*, vol. 113, pp. 174–187, 2016, doi: 10.1016/j.conbuildmat.2016.03.039.

[12] A. Habibnejad Korayem, H. Ziari, M. Hajiloo, M. Abarghooie, and P. Karimi, 'Laboratory evaluation of stone mastic asphalt containing amorphous carbon powder as filler material', *Construction and Building Materials*, vol. 243, p. 118280, 2020, doi: 10.1016/j.conbuildmat.2020.118280.

[13] F. M. Nejad, 'The effects of bitumen percentage and percentage of air void on rutting potential of hma by using of dynamic creep test', in *Proceedings of the 10th Annual International Conference on Sustainable Construction & Pavement Engineering*, Liverpool, UK, 2011.

[14] Y. Liu, P. Su, M. Li, Z. You, and M. Zhao, 'Review on evolution and evaluation of asphalt pavement structures and materials', *Journal of Traffic and Transportation Engineering (English Edition)*, vol. 7, no. 5, pp. 573–599, 2020, doi: 10.1016/j.jtte.2020.05.003.

[15] M. C. Rubio, G. Martínez, L. Baena, and F. Moreno, 'Warm mix asphalt: an overview', *Journal of Cleaner Production*, vol. 24, pp. 76–84, 2012, doi: 10.1016/j.jclepro.2011.11.053.

[16] S. Jain and B. Singh, 'Cold mix asphalt: An overview', *Journal of Cleaner Production*, vol. 280, p. 124378, 2021, doi: 10.1016/j.jclepro.2020.124378.

[17] J. Zhu, B. Birgisson, and N. Kringos, 'Polymer modification of bitumen: Advances and challenges', *European Polymer Journal*, vol. 54, pp. 18–38, 2014, doi: 10.1016/j.eurpolymj.2014.02.005.

[18] C. Oliviero Rossi, P. Caputo, S. Ashimova, A. Fabozzi, G. D'Errico, and R. Angelico, 'Effects of Natural Antioxidant Agents on the Bitumen Aging Process: An EPR and Rheological Investigation', *Applied Sciences*, vol. 8, no. 8, p. 1405, 2018, doi: 10.3390/app8081405.

[19] A. Aksoy, K. Şamlioglu, S. Tayfur, and H. Özen, 'Effects of various additives on the moisture damage sensitivity of asphalt mixtures', *Construction and Building Materials*, vol. 19, no. 1, pp. 11–18, 2005, doi: 10.1016/j.conbuildmat.2004.05.003.

[20] R. N. Hunter, 'Assessing aggregates for use in asphalts', in *Asphalts in road construction*, Thomas Telford, 2000.

[21] N. Palankar, A. U. Ravi Shankar, and B. M. Mithun, 'Investigations on Alkali-Activated Slag/Fly Ash Concrete with steel slag coarse aggregate for pavement structures', *International Journal of Pavement Engineering*, vol. 18, no. 6, pp. 500–512, 2017, doi: 10.1080/10298436.2015.1095902.

[22] F. Moreno, M. C. Rubio, and M. J. Martinez-Echevarria, 'Analysis of digestion time and the crumb rubber percentage in dry-process crumb rubber modified hot bituminous mixes', *Construction and Building Materials*, vol. 25, no. 5, pp. 2323–2334, 2011, doi: 10.1016/j.conbuildmat.2010.11.029.

[23] A. Hassani, H. Ganjidoust, and A. A. Maghanaki, 'Use of plastic waste (poly-ethylene terephthalate) in asphalt concrete mixture as aggregate replacement', *Waste Manag Res*, vol. 23, no. 4, pp. 322–327, Aug. 2005, doi: 10.1177/0734242X05056739.

[24] A. Behnood, 'Application of rejuvenators to improve the rheological and mechanical properties of asphalt binders and mixtures: A review', *Journal of Cleaner Production*, vol. 231, pp. 171–182, 2019, doi: 10.1016/j.jclepro.2019.05.209.

[25] T. Al-Mansoori, J. Norambuena-Contreras, R. Micaelo, and A. Garcia, 'Self-healing of asphalt mastic by the action of polymeric capsules containing rejuvenators', *Construction and Building Materials*, vol. 161, pp. 330–339, 2018, doi: 10.1016/j.conbuildmat.2017.11.125.

[26] Á. García, E. Schlangen, M. Van De Ven, and G. Sierra-Beltrán, 'Preparation of capsules containing rejuvenators for their use in asphalt concrete', *Journal of Hazardous Materials*, vol. 184, no. 1–3, pp. 603–611, 2010, doi: 10.1016/j.jhazmat.2010.08.078.

[27] D. Sun *et al.*, 'A comprehensive review on self-healing of asphalt materials: Mechanism, model, characterization and enhancement', *Advances in Colloid and Interface Science*, vol. 256, pp. 65–93, 2018, doi: 10.1016/j.cis.2018.05.003.

[28] J. Ji *et al.*, 'Effectiveness of Vegetable Oils as Rejuvenators for Aged Asphalt Binders', *J. Mater. Civ. Eng.*, vol. 29, no. 3, p. D4016003, 2017, doi: 10.1061/(ASCE)MT.1943-5533.0001769.

[29] I. Gonzalez-Torre and J. Norambuena-Contreras, 'Recent advances on self-healing of bituminous materials by the action of encapsulated rejuvenators', *Construction and Building Materials*, vol. 258, p. 119568, 2020, doi: 10.1016/j.conbuildmat.2020.119568.

[30] N. Ruiz-Riancho, A. Garcia, D. Grossegger, T. Saadoon, and R. Hudson-Griffiths, 'Properties of Ca-alginate capsules to maximise asphalt self-healing properties', *Construction and Building Materials*, vol. 284, p. 122728, 2021, doi: 10.1016/j.conbuildmat.2021.122728.

[31] T. Al-Mansoori, J. Norambuena-Contreras, and A. Garcia, 'Effect of capsule addition and healing temperature on the self-healing potential of asphalt mixtures', *Mater Struct*, vol. 51, no. 2, p. 53, 2018, doi: 10.1617/s11527-018-1172-5.

[32] D. Pearson, *Deterioration and Maintenance of Pavements*, First edition. ICE Publishing, 2011. doi: 10.1680/dmp.41141.

[33] Design Manual for Roads and Bridges (DMRB), 'CD 225. Design for New Pavement Construction'. Accessed: Aug. 02, 2023. [Online]. Available: https://www.standardsforhighways.co.uk/ha/standards/

[34] E. J. Yoder and W. Matthew W., *Principles of pavement design*. John Wiley & Sons, 1991.

[35] Y. H. Huang, *Pavement Analysis and Design*, Second. Upper Saddle River, NJ: Pearson/Prentice Hall, 2004.

[36] S. S. Adlinge and P. a K. Gupta, 'Pavement Deterioration and its Causes', *Mechanical & Civil Engineering*, pp. 9–15, 2009.

[37] National Asphalt Pavement Association, 'HMA Pavement Mix Type Selection Guide', National Asphalt Pavement Association (NAPA), 2001.

[38] R. N. Hunter, 'Functions and properties of road layers', in *Asphalts in road construction*, Thomas Telford, 2000.

[39] Design Manual for Roads and Bridges (DMRB), 'CD 224. Traffic Assessment'. Accessed: Aug. 02, 2023. [Online]. Available: https://www.standardsforhighways.co.uk/ha/standards/

[40] R. N. Hunter, 'Design and maintenance of asphalt pavements', in *Asphalts in road construction*, Thomas Telford, 2000.

[41] 'Manual for Design of Hot Mix Asphalt with Commentary: (NCHRP Report 673)', Transportation Research Board (TRB), 2011.

[42] A. M. Babalghaith *et al.*, 'A systematic review of the utilization of waste materials as aggregate replacement in stone matrix asphalt mixes', *Environ Sci Pollut Res*, vol. 29, no. 24, pp. 35557–35582, 2022, doi: 10.1007/s11356-022-19447-w.

[43] F. L. Roberts, L. N. Mohammad, and L. B. Wang, 'History of Hot Mix Asphalt Mixture Design in the United States', *J. Mater. Civ. Eng.*, vol. 14, no. 4, pp. 279–293, 2002, doi: 10.1061/(ASCE)0899-1561(2002)14:4(279).

[44] C. O'Flaherty and D. Hughes, Eds., 'Materials used in road pavements', in *Highways: The location, design, construction and maintenance of road pavements*, Fifth., ICE Publishing, 2015. doi: 10.1680/h5e.59931.

[45] D. Woodward and M. Forde, 'Aggregate properties and test methods', in *ICE manual of Construction Materials*, Thomas Telford Ltd, 2009.

[46] C. O'Flaherty and D. Hughes, Eds., 'Standard asphalt mixtures used in pavement layers', in *Highways: The location, design, construction and maintenance of road pavements*, Fifth., ICE Publishing, 2015. doi: 10.1680/h5e.59931.

[47] Asphalt Institute, *MS-2 asphalt mix design methods*, 7th edition. Lexington, KY: Asphalt Institute, 2014.

[48] S. Caro, E. Masad, A. Bhasin, and D. Little, 'Probabilistic Modeling of the Effect of Air Voids on the Mechanical Performance of Asphalt Mixtures Subjected to Moisture Diffusion', *Asphalt Paving Technology-Proceedings Association of Asphalt Technologists*, vol. 79, no. 221, 2010.

[49] Z. Leng, 'Prediction of in-situ asphalt mixture density using ground penetrating radar: theoretical development and field verification', *University of Illinois at Urbana-Champaign*, 2011.

[50] 'Pavement Manual', Texas Department of Trnasportation, Abstract, 2016.

[51] R. Elvik and P. Greibe, 'Road safety effects of porous asphalt: a systematic review of evaluation studies', *Accident Analysis & Prevention*, vol. 37, no. 3, pp. 515–522, 2005, doi: 10.1016/j.aap.2005.01.003.

[52] M. Taghipoor, A. Hassani, and M. M. Karimi, 'Development of procedure for design and preparation of open-graded asphalt mixture used in semi-flexible pavement', *Construction and Building Materials*, vol. 306, p. 124884, 2021, doi: 10.1016/j.conbuildmat.2021.124884.

[53] H. Wu, J. Yu, W. Song, J. Zou, Q. Song, and L. Zhou, 'A critical state-of-the-art review of durability and functionality of open-graded friction course mixtures', *Construction and Building Materials*, vol. 237, p. 117759, Mar. 2020, doi: 10.1016/j.conbuildmat.2019.117759.

[54] 'APWA GSP 4-07. Asphalt Treated Permeable Base (ATPB)'. 2015.

[55] S. Pathak, R. Choudhary, and A. Kumar, 'Drainability and Clogging Behavior of Open-Graded Asphalt Friction Courses with Basic Oxygen Furnace Steel Slag Aggregates', *Transportation Research Record: Journal of the Transportation Research Board*, vol. 2676, no. 12, pp. 356–373, 2022, doi: 10.1177/03611981221095525.

[56] R. M. Xavier, B. Martin, L. A. Babu, L. E. Jose, and L. Roy, 'A Review on Fiber Modified Stone Matrix Asphalt', *International Research Journal of Engineering and Technology (IRJET)*, vol. 05, no. 03, 2018.

[57] L. Devulapalli, G. Sarang, and S. Kothandaraman, 'Characteristics of aggregate gradation, drain down and stabilizing agents in stone matrix asphalt mixtures: A state of art review', *Journal of Traffic and Transportation Engineering (English Edition)*, vol. 9, no. 2, pp. 167–179, 2022, doi: 10.1016/j.jtte.2021.10.007.

[58] E. Gashi, H. Sadiku, and M. Misini, 'A Review of Aggregate and Asphalt mixture Specific Gravity measurements and their Impacts on Asphalt Mix Design Properties and Mix Acceptance', *IJAERS*, vol. 4, no. 5, pp. 195–201, 2017, doi: 10.22161/ijaers.4.5.31.

[59] A. F. Ikechukwu and M. M. Hassan, 'Assessing the Extent of Pavement Deterioration Caused by Subgrade Volumetric Movement Through Moisture Infiltration', *Int. J. Pavement Res. Technol.*, vol. 15, no. 3, pp. 676–692, 2022, doi: 10.1007/s42947-021-00044-y.

[60] A. Milling, H. Martin, and A. Mwasha, 'Design, Construction, and In-Service Causes of Premature Pavement Deterioration: A Fuzzy Delphi Application', *J. Transp. Eng., Part B: Pavements*, vol. 149, no. 1, p. 05022004, 2023, doi: 10.1061/JPEODX.PVENG-1071.

[61] J. V. Camahan, W. J. Davis, M. Y. Shahin, P. L. Keane, and M. I. Wu, 'Optimal Maintenance Decisions for Pavement Management', *J. Transp. Eng.*, vol. 113, no. 5, pp. 554–572, 1987, doi: 10.1061/(ASCE)0733-947X(1987)113:5(554).

[62] J. D. Brock *et al.*, 'Perpetual Bituminous Pavements', *Transportation Research Circular*, vol. 503, no. 12, pp. 32–49.

[63] M. Raheel *et al.*, 'Impact of axle overload, asphalt pavement thickness and subgrade modulus on load equivalency factor using modified ESALs equation', *Cogent Engineering*, vol. 5, no. 1, p. 1528044, 2018, doi: 10.1080/23311916.2018.1528044.

[64] J. J. Hajek, 'General axle load equivalency factors', *Transportation Research Record*, vol. 1482, p. 67, 1995.

[65] S. I. R. Amorim, J. C. Pais, A. C. Vale, and M. J. C. Minhoto, 'A model for equivalent axle load factors', *International Journal of Pavement Engineering*, vol. 16, no. 10, pp. 881–893, 2015, doi: 10.1080/10298436.2014.968570.

[66] P. S. Kandhal, C. W. Lubold, and F. L. Roberts, 'Water Damage to Asphalt Overlays: Case Stories', *Association of Asphalt Paving Technologists Proc*, vol. 58, 1989.

[67] B. Ruth, Ed., *Evaluation and Prevention of Water Damage to Asphalt Pavement Materials*. 100 Barr Harbor Drive, PO Box C700, West Conshohocken, PA 19428-2959: ASTM International, 1985. doi: 10.1520/STP899-EB.

[68] A. Yilmaz and Ş. Sargin, 'Water Effect on Deterioration Of Asphalt Pavements', *TOJSAT*, vol. 2, no. 1, 2012.

[69] J. C. Nicholls, M. J. Mchale, and R. D. Griffiths, *Best practice guide for durability of asphalt pavements*, no. 42. 2008. [Online]. Available: http://trid.trb.org/view.aspx?id=864458

[70] E. Simonsen and U. Isacsson, 'Thaw weakening of pavement structures in cold regions', *Cold Regions Science and Technology*, vol. 29, no. 2, pp. 135–151, 1999, doi: 10.1016/S0165-232X(99)00020-8.

[71] B. Hallet, 'Why Do Freezing Rocks Break?', *Science*, vol. 314, no. 5802, pp. 1092–1093, 2006, doi: 10.1126/science.1135200.

[72] E. Remišová, M. Decký, L. Podolka, M. Kováč, T. Vondráčková, and L. Bartuška, 'Frost Index from Aspect of Design of Pavement Construction in Slovakia', *Procedia Earth and Planetary Science*, vol. 15, pp. 3–10, 2015, doi: 10.1016/j.proeps.2015.08.002.

[73] M. Bäckström, 'Ground Temperature in Porous Pavement during Freezing and Thawing', *J. Transp. Eng.*, vol. 126, no. 5, pp. 375–381, 2000, doi: 10.1061/(ASCE)0733-947X(2000)126:5(375).

[74] J. P. McGreevy, 'Some perspectives on frost shattering', *Progress in Physical Geography: Earth and Environment*, vol. 5, no. 1, pp. 56–75, 1981, doi: 10.1177/030913338100500103.

[75] G. Liao, M. Heitzman, R. West, S. Wang, and C. Ai, 'Temperature Effects on the Correlations between Tire-Pavement Noises and Pavement Surface Characteristics', in

New Frontiers in Road and Airport Engineering, Shanghai, China: American Society of Civil Engineers, 2015, pp. 219–232. doi: 10.1061/9780784414255.021.

[76] O. A. Abaza, M. Arafat, and T. D. Chowdhury, 'Influence of Asphalt Surface Temperature on Pavement Rutting in Cold Regions', in *Airfield and Highway Pavements 2019*, Chicago, Illinois: American Society of Civil Engineers, 2019, pp. 306–315. doi: 10.1061/9780784482452.030.

[77] D. H. Timm, V. R. Voller, E. Lee, and J. Harvey, 'Calcool: A multi-layer Asphalt Pavement Cooling Tool for Temperature Prediction During Construction', *International Journal of Pavement Engineering*, vol. 2, no. 3, pp. 169–185, 2001, doi: 10.1080/10298430108901725.

[78] E. Schnebele, B. F. Tanyu, and G. Cervone, 'Review of remote sensing methodologies for pavement management and assessment', *European Transport Research Review*, vol. 7, no. 2, 2015, doi: 10.1007/s12544-015-0156-6.

[79] J. S. Miller and Y. B. William, 'Miller, John S., and William Y. Bellinger. Distress identification manual for the long-term pavement performance program', Federal Highway Administration. Office of Infrastructure Research and Development, United States, FHWA-RD-03-031, 2003.

[80] L. M. Pierce, G. McGovern, and K. A. Zimmerman, 'Practical Guide for Quality Management of Pavement Condition Data Collection', Federal Highway Administration. Office of Infrastructure Research and Development, United States.

[81] G. Cossale, R. Elliott, and I. Widyatmoko, 'The Importance of Road Surface Texture in Active Road Safety Design and Assessment.', 2013.

[82] D. W. and J. C. N. M E Nunn, A Brown, 'Design of long-life flexible pavements for heavy traffic Prepared for Highways Agency , British Aggregate Construction', *Transport Research Laboratory*, vol. TRL REPORT, no. June, 1997.

[83] J. H. G. Wambura, J. Maina, and H. R. Smith, 'Kenya Bituminous Materials Study', *Transportation Research Record*, vol. 1681, no. 1, pp. 129–137, 1999, doi: 10.3141/1681-16.

[84] R. B. Mallick and T. El-Korchi, 'Distress and Performance', in *Pavement Engineering - Principles and Practice*, Third., CRC Press, 2018.

[85] L. Sun, G. Wang, H. Zhang, and L. Liu, 'Initiation and propagation of top-down cracking in asphalt pavement', *Applied Sciences (Switzerland)*, vol. 8, no. 5, 2018, doi: 10.3390/app8050774.

[86] F. Canestrari and L. P. Ingrassia, 'A review of top-down cracking in asphalt pavements: Causes, models, experimental tools and future challenges', *Journal of Traffic and Transportation Engineering (English Edition)*, vol. 7, no. 5, pp. 541–572, 2020, doi: 10.1016/j.jtte.2020.08.002.

[87] I. Bessa, K. Vasconcelos, V. Castelo Branco, L. A. Nascimento, and L. Bernucci, 'Prediction of Fatigue Cracking in Flexible and Semi-rigid Asphalt Pavement Sections', *Int. J. Pavement Res. Technol.*, vol. 16, no. 3, pp. 563–575, 2023, doi: 10.1007/s42947-021-00148-5.

[88] L. B. Wang, L. A. Myers, L. N. Mohammad, and Y. R. Fu, 'Micromechanics Study on Top-Down Cracking', *Transportation Research Record*, vol. 1853, no. 1, pp. 121–133, 2003, doi: 10.3141/1853-14.

[89] M. de Beer, C. Fisher, and F. J. Jooste, 'Determination of pneumatic tyre/pavement interface contact stresses under moving loads and some effects on pavements with thin asphalt surfacing layers'.

[90] T. Svasdisant, M. Schorsch, G. Y. Baladi, and S. Pinyosunun, 'Mechanistic Analysis of Top-Down Cracks in Asphalt Pavements', *Transportation Research Record*, vol. 1809, no. 1, pp. 126–136, 2002, doi: 10.3141/1809-15.

[91] S. Nithin, K. Rajagopal, and A. Veeraragavan, 'Reflection Cracking: A Review on the Potential of Interlayer System with reference to Natural Fibres'.

[92] J. De Visscher and A. Vanelstraete, 'Ravelling by traffic: Performance testing and field validation', *International Journal of Pavement Research and Technology*, vol. 10, no. 1, pp. 54–61, 2017, doi: 10.1016/j.ijprt.2016.12.004.

[93] G. D'Angelo, C. Ojum, I. Widyatmoko, M. Wayman, and A. Khojinian, 'Ravelling resistance of UK thin asphalt surface course systems under a large-scale accelerated test method', 2016.

[94] H. Zhang, K. Anupam, A. Skarpas, C. Kasbergen, and S. Erkens, 'Simple Homogenization-Based Approach to Predict Raveling in Porous Asphalt', *Transportation Research Record*, vol. 2674, no. 12, pp. 263–277, 2020, doi: 10.1177/0361198120953159.

[95] R. N. Hunter, A. Self, and J. Read, *The Shell Bitumen handbook*, Sixth edition. Westminster, London: Published for Shell Bitumen by ICE Publishing, 2015.

[96] J. C. Nicholls, J. de Visscher, F. Hammoum, and M. Jacobs, 'DRaT–Development of the Ravelling Test Review of parameters influencing the propensity of asphalt to ravel', 2015.

[97] C. Gorkem and B. Sengoz, 'Predicting stripping and moisture induced damage of asphalt concrete prepared with polymer modified bitumen and hydrated lime', *Construction and Building Materials*, vol. 23, no. 6, pp. 2227–2236, 2009, doi: 10.1016/j.conbuildmat.2008.12.001.

[98] Wallis, 'The UKPMS User Manual Volume 2: Visual Data Collection for UKPMS', 2009.

[99] 'Highway asset management survey - carriageways', Transport for London, 2010.

[100] A. H. Albayati, 'A review of rutting in asphalt concrete pavement', *Open Engineering*, vol. 13, no. 1, p. 20220463, 2023, doi: 10.1515/eng-2022-0463.

[101] R. Joumblat, Z. Al Basiouni Al Masri, G. Al Khateeb, A. Elkordi, A. R. El Tallis, and J. Absi, 'State-of-the-Art Review on Permanent Deformation Characterization of Asphalt Concrete Pavements', *Sustainability*, vol. 15, no. 2, p. 1166, 2023, doi: 10.3390/su15021166.

[102] T. B. Moghaddam, M. R. Karim, and M. Abdelaziz, 'A review on fatigue and rutting performance of asphalt mixes', *Sci. Res. Essays*.

[103] R. Garba, 'Permanent deformation properties of asphalt concrete mixtures', 2002.

[104] A. Ragnoli, M. De Blasiis, and A. Di Benedetto, 'Pavement Distress Detection Methods: A Review', *Infrastructures*, vol. 3, no. 4, p. 58, 2018, doi: 10.3390/infrastructures3040058.

[105] R. B. Smith, 'Forensic Investigation of Pavement Failures', University of Southern Queensland, 2004.

[106] Q. Dong, B. Huang, and S. Zhao, 'Field and laboratory evaluation of winter season pavement pothole patching materials', *International Journal of Pavement Engineering*, vol. 15, no. 4, pp. 279–289, 2014, doi: 10.1080/10298436.2013.814772.

[107] 'Technical Note. Road Condition and Maintenance Data'. UK. 2021.

[108] L. E. Vallejo, 'Fractal Assessment of the Surface Texture of Pavements', *International Journal of Pavement Engineering*, vol. 2, no. 2, pp. 149–156, 2001, doi: 10.1080/10298430108901723.

[109] R. B. Kogbara, E. A. Masad, E. Kassem, A. (Tom) Scarpas, and K. Anupam, 'A state-of-the-art review of parameters influencing measurement and modeling of skid resistance of asphalt pavements', *Construction and Building Materials*, vol. 114, pp. 602–617, 2016, doi: 10.1016/j.conbuildmat.2016.04.002.

[110] I. M. Asi, 'Evaluating skid resistance of different asphalt concrete mixes', *Building and Environment*, vol. 42, no. 1, pp. 325–329, 2007, doi: 10.1016/j.buildenv.2005.08.020.

[111] M.-T. Do, Z. Tang, M. Kane, and F. De Larrard, 'Evolution of road-surface skid-resistance and texture due to polishing', *Wear*, vol. 266, no. 5–6, pp. 574–577, Mar. 2009, doi: 10.1016/j.wear.2008.04.060.

[112] Design Manual for Roads and Bridges (DMRB), 'CD 228. Skidding resistance'. Accessed: Aug. 02, 2023. [Online]. Available: https://www.standardsforhighways.co.uk/ha/standards/

[113] C. G. Thigpen, H. Li, S. L. Handy, and J. Harvey, 'Modeling the Impact of Pavement Roughness on Bicycle Ride Quality', *Transportation Research Record*, vol. 2520, no. 1, pp. 67–77, 2015, doi: 10.3141/2520-09.

[114] Sayers, 'The little book of profiling: basic information about measuring and interpreting road profiles.', University of Michigan, Ann Arbor, Transportation Research Institute, 1998.

[115] G. Cantisani and G. Loprencipe, 'Road Roughness and Whole Body Vibration: Evaluation Tools and Comfort Limits', *J. Transp. Eng.*, vol. 136, no. 9, pp. 818–826, 2010, doi: 10.1061/(ASCE)TE.1943-5436.0000143.

[116] K. Park, N. E. Thomas, and K. Wayne Lee, 'Applicability of the International Roughness Index as a Predictor of Asphalt Pavement Condition', *J. Transp. Eng.*, vol. 133, no. 12, pp. 706–709, 2007, doi: 10.1061/(ASCE)0733-947X(2007)133:12(706).

[117] Y. Du, C. Liu, D. Wu, and S. Jiang, 'Measurement of International Roughness Index by Using Z -Axis Accelerometers and GPS', *Mathematical Problems in Engineering*, vol. 2014, pp. 1–10, 2014, doi: 10.1155/2014/928980.

[118] T. D. Gillespie, 'Everything You Always Wanted to Know about the IRI, But Were Afraid to Ask!'.

[119] O. Sirin, D. K. Paul, and E. Kassem, 'State of the Art Study on Aging of Asphalt Mixtures and Use of Antioxidant Additives', *Advances in Civil Engineering*, vol. 2018, pp. 1–18, 2018, doi: 10.1155/2018/3428961.

[120] F. Durrieu, F. Farcas, and V. Mouillet, 'The influence of UV aging of a Styrene/Butadiene/Styrene modified bitumen: Comparison between laboratory and on site aging', *Fuel*, vol. 86, no. 10–11, pp. 1446–1451, 2007, doi: 10.1016/j.fuel.2006.11.024.

[121] S. Wu, L. Pang, L. Mo, J. Qiu, G. Zhu, and Y. Xiao, 'UV and Thermal Aging of Pure Bitumen-comparison Between Laboratory Simulation and Natural Exposure Aging', *Road Materials and Pavement Design*, vol. 9, no. sup1, pp. 103–113, 2008, doi: 10.1080/14680629.2008.9690161.

[122] Y. Yildirim, 'Polymer modified asphalt binders', *Construction and Building Materials*, vol. 21, no. 1, pp. 66–72, 2007, doi: 10.1016/j.conbuildmat.2005.07.007.

[123] Á. García, 'Self-healing of open cracks in asphalt mastic', *Fuel*, vol. 93, pp. 264–272, 2012, doi: 10.1016/j.fuel.2011.09.009.

[124] 'Self-Healing Materials: An Alternative Approach to 20 Centuries of Materials Science', *Chemistry International -- Newsmagazine for IUPAC*, vol. 30, no. 6, 2008, doi: 10.1515/ci.2008.30.6.20.

[125] J. Qiu, M. F. C. Van De Ven, S. P. Wu, J. Y. Yu, and A. A. A. Molenaar, 'Investigating self healing behaviour of pure bitumen using Dynamic Shear Rheometer', *Fuel*, vol. 90, no. 8, pp. 2710–2720, 2011, doi: 10.1016/j.fuel.2011.03.016.

[126] S. Xu, A. García, J. Su, Q. Liu, A. Tabaković, and E. Schlangen, 'Self-Healing Asphalt Review: From Idea to Practice', *Adv Materials Inter*, vol. 5, no. 17, p. 1800536, 2018, doi: 10.1002/admi.201800536.

[127] L. W. Corbett, 'Composition of asphalt based on generic fractionation, using solvent deasphaltening, elution-adsorption chromatography, and densimetric characterization', *Anal. Chem.*, vol. 41, no. 4, pp. 576–579, 1969, doi: 10.1021/ac60273a004.

[128] F. L. Robert, P. S. Kandhal, and E. R. Bron, *Hot mix asphalt materials, mixture design and construction. K (1991).* 1991.

[129] D. Lesueur, 'The colloidal structure of bitumen: Consequences on the rheology and on the mechanisms of bitumen modification', *Advances in Colloid and Interface Science*, vol. 145, no. 1–2, pp. 42–82, 2009, doi: 10.1016/j.cis.2008.08.011.

[130] J. Shen, S. Amirkhanian, and J. Aune Miller, 'Effects of Rejuvenating Agents on Superpave Mixtures Containing Reclaimed Asphalt Pavement', *J. Mater. Civ. Eng.*, vol. 19, no. 5, pp. 376–384, 2007, doi: 10.1061/(ASCE)0899-1561(2007)19:5(376).

[131] J. Brownridge, 'The Role of an Asphalt Rejuvenator in Pavement Preservation: Use and Need for Asphalt Rejuvenation', presented at the Compendium of papers from the first international conference on pavement preservation, USA: Newport Beach CA, 2010.

[132] A. I. Rajib, A. Samieadel, A. Zalghout, K. E. Kaloush, B. K. Sharma, and E. H. Fini, 'Do all rejuvenators improve asphalt performance?', *Road Materials and Pavement Design*, vol. 23, no. 2, pp. 358–376, 2022, doi: 10.1080/14680629.2020.1826348.

[133] M. Zaumanis, R. B. Mallick, and R. Frank, 'Evaluation of different recycling agents for restoring aged asphalt binder and performance of 100 % recycled asphalt', *Mater Struct*, vol. 48, no. 8, pp. 2475–2488, 2015, doi: 10.1617/s11527-014-0332-5.

[134] K. Zhao, Y. Wang, L. Chen, and F. Li, 'Diluting or dissolving? The use of relaxation spectrum to assess rejuvenation effects in asphalt recycling', *Construction and Building Materials*, vol. 188, pp. 143–152, 2018, doi: 10.1016/j.conbuildmat.2018.08.098.

[135] J. L. Concha *et al.*, 'Effect of rejuvenating oil type on the synthesis and properties of alginate-based polynuclear capsules for asphalt self-healing', *Road Materials and Pavement Design*, vol. 24, no. 7, pp. 1669–1694, 2023, doi: 10.1080/14680629.2022.2092026.

[136] S. Xu *et al.*, 'The role of rejuvenators in embedded damage healing for asphalt pavement', *Materials & Design*, vol. 202, p. 109564, 2021, doi: 10.1016/j.matdes.2021.109564.

[137] J. Norambuena-Contreras, L. E. Arteaga-Perez, A. Y. Guadarrama-Lezama, R. Briones, J. F. Vivanco, and I. Gonzalez-Torre, 'Microencapsulated Bio-Based Rejuvenators for the Self-Healing of Bituminous Materials', *Materials*, vol. 13, no. 6, p. 1446, 2020, doi: 10.3390/ma13061446.

[138] J. Norambuena-Contreras, J. Concha, L. Arteaga-Pérez, and I. Gonzalez-Torre, 'Synthesis and Characterisation of Alginate-Based Capsules Containing Waste Cooking Oil for Asphalt Self-Healing', *Applied Sciences*, vol. 12, no. 5, p. 2739, 2022, doi: 10.3390/app12052739.

[139] Ö. E. Yamaç, M. Yilmaz, E. Yalçın, B. V. Kök, J. Norambuena-Contreras, and A. Garcia, 'Self-healing of asphalt mastic using capsules containing waste oils', *Construction and Building Materials*, vol. 270, p. 121417, 2021, doi: 10.1016/j.conbuildmat.2020.121417.

[140] J. L. Concha, L. E. Arteaga-Pérez, I. Gonzalez-Torre, Q. Liu, and J. Norambuena-Contreras, 'Biopolymeric Capsules Containing Different Oils as Rejuvenating Agents for Asphalt Self-Healing: A Novel Multivariate Approach', *Polymers*, vol. 14, no. 24, p. 5418, 2022, doi: 10.3390/polym14245418.

[141] S. J. Risch and G. A. Reineccius, Eds., *Encapsulation and Controlled Release of Food Ingredients*, vol. 590. in ACS Symposium Series, vol. 590. Washington, DC: American Chemical Society, 1995. doi: 10.1021/bk-1995-0590.

[142] A. Kanellopoulos, P. Giannaros, D. Palmer, A. Kerr, and A. Al-Tabbaa, 'Polymeric microcapsules with switchable mechanical properties for self-healing concrete: synthesis, characterisation and proof of concept', *Smart Mater. Struct.*, vol. 26, no. 4, p. 045025, 2017, doi: 10.1088/1361-665X/aa516c.

[143] A. Garcia, J. Jelfs, and C. J. Austin, 'Internal asphalt mixture rejuvenation using capsules', *Construction and Building Materials*, vol. 101, pp. 309–316, 2015, doi: 10.1016/j.conbuildmat.2015.10.062.

[144] Á. García, E. Schlangen, and M. Van De Ven, 'Properties of capsules containing rejuvenators for their use in asphalt concrete', *Fuel*, vol. 90, no. 2, pp. 583–591, 2011, doi: 10.1016/j.fuel.2010.09.033.

[145] A. Garcia, C. J. Austin, and J. Jelfs, 'Mechanical properties of asphalt mixture containing sunflower oil capsules', *Journal of Cleaner Production*, vol. 118, pp. 124–132, 2016, doi: 10.1016/j.jclepro.2016.01.072.

[146] D. Sun, T. Lu, X. Zhu, B. Li, and Y. Tian, 'Optimization of synthesis technology to improve the design of asphalt self-healing microcapsules', *Construction and Building Materials*, vol. 175, pp. 88–103, 2018, doi: 10.1016/j.conbuildmat.2018.04.162.

[147] J. Norambuena-Contreras, Q. Liu, L. Zhang, S. Wu, E. Yalcin, and A. Garcia, 'Influence of encapsulated sunflower oil on the mechanical and self-healing properties of dense-graded asphalt mixtures', *Mater Struct*, vol. 52, no. 4, p. 78, 2019, doi: 10.1617/s11527-019-1376-3.

[148] A. Tabaković, W. Post, D. Cantero, O. Copuroglu, S. J. Garcia, and E. Schlangen, 'The reinforcement and healing of asphalt mastic mixtures by rejuvenator encapsulation in alginate compartmented fibres', *Smart Mater. Struct.*, vol. 25, no. 8, p. 084003, 2016, doi: 10.1088/0964-1726/25/8/084003.

[149] D. Sun *et al.*, 'Aided regeneration system of aged asphalt binder based on microcapsule technology', *Construction and Building Materials*, vol. 201, pp. 571–579, 2019, doi: 10.1016/j.conbuildmat.2018.12.167.

[150] J.-F. Su, E. Schlangen, and J. Qiu, 'Design and construction of microcapsules containing rejuvenator for asphalt', *Powder Technology*, vol. 235, pp. 563–571, 2013, doi: 10.1016/j.powtec.2012.11.013.

[151] J.-F. Su, P. Yang, Y.-Y. Wang, S. Han, N.-X. Han, and W. Li, 'Investigation of the Self-Healing Behaviors of Microcapsules/Bitumen Composites by a Repetitive Direct Tension Test', *Materials*, vol. 9, no. 7, p. 600, 2016, doi: 10.3390/ma9070600.

[152] Y.-Y. Wang, J.-F. Su, E. Schlangen, N.-X. Han, S. Han, and W. Li, 'Fabrication and characterization of self-healing microcapsules containing bituminous rejuvenator by a nano-inorganic/organic hybrid method', *Construction and Building Materials*, vol. 121, pp. 471–482, 2016, doi: 10.1016/j.conbuildmat.2016.06.021.

[153] J.-F. Su *et al.*, 'Experimental observation of the vascular self-healing hollow fibers containing rejuvenator states in bitumen', *Construction and Building Materials*, vol. 201, pp. 715–727, 2019, doi: 10.1016/j.conbuildmat.2019.01.001.

[154] A. Tabaković *et al.*, 'The compartmented alginate fibres optimisation for bitumen rejuvenator encapsulation', *Journal of Traffic and Transportation Engineering (English Edition)*, vol. 4, no. 4, pp. 347–359, 2017, doi: 10.1016/j.jtte.2017.01.004.

[155] B. Shu, L. Zhang, S. Wu, L. Dong, Q. Liu, and Q. Wang, 'Synthesis and characterization of compartmented Ca-alginate/silica self-healing fibers containing bituminous rejuvenator', *Construction and Building Materials*, vol. 190, pp. 623–631, 2018, doi: 10.1016/j.conbuildmat.2018.09.121.

[156] X.-L. Zhang *et al.*, 'Novel vascular self-nourishing and self-healing hollow fibers containing oily rejuvenator for bitumen', *Construction and Building Materials*, vol. 183, pp. 150–162, 2018, doi: 10.1016/j.conbuildmat.2018.06.181.

[157] R. Micaelo, T. Al-Mansoori, and A. Garcia, 'Study of the mechanical properties and self-healing ability of asphalt mixture containing calcium-alginate capsules', *Construction and Building Materials*, vol. 123, pp. 734–744, 2016, doi: 10.1016/j.conbuildmat.2016.07.095.

[158] L. Zhang *et al.*, 'Synthesis and characterization of multi-cavity Ca-alginate capsules used for self-healing in asphalt mixtures', *Construction and Building Materials*, vol. 211, pp. 298–307, 2019, doi: 10.1016/j.conbuildmat.2019.03.224.

[159] N. Ruiz-Riancho, T. Saadoon, A. Garcia, D. Grossegger, and R. Hudson-Griffiths, 'Optimisation of self-healing properties for asphalts containing encapsulated oil to mitigate reflective cracking and maximize skid and rutting resistance', *Construction and Building Materials*, vol. 300, p. 123879, 2021, doi: 10.1016/j.conbuildmat.2021.123879.

[160] A. Gray, S. Egan, S. Bakalis, and Z. Zhang, 'Determination of microcapsule physicochemical, structural, and mechanical properties', *Particuology*, vol. 24, pp. 32–43, 2016, doi: 10.1016/j.partic.2015.06.002.

[161] R. Micaelo, T. Al-Mansoori, and A. Garcia, 'Effect of capsules containing sunflower oil on the mechanical behaviour of aged asphalt mixture', 2016.

[162] S. Xu, A. Tabaković, X. Liu, and E. Schlangen, 'Calcium alginate capsules encapsulating rejuvenator as healing system for asphalt mastic', *Construction and*

Building Materials, vol. 169, pp. 379–387, 2018, doi: 10.1016/j.conbuildmat.2018.01.046.

[163] J. Norambuena-Contreras, E. Yalcin, A. Garcia, T. Al-Mansoori, M. Yilmaz, and R. Hudson-Griffiths, 'Effect of mixing and ageing on the mechanical and self-healing properties of asphalt mixtures containing polymeric capsules', *Construction and Building Materials*, vol. 175, pp. 254–266, 2018, doi: 10.1016/j.conbuildmat.2018.04.153.

[164] J. Norambuena-Contreras, E. Yalcin, M. Yilmaz, I. Chan, M. A. Rashdi, and A. Garcia, 'Physical, Thermal And Mechanical Properties Of Polymeric Calcium-Alginate Capsules For Asphalt Self-Healing', 2018.

[165] T. Al-Mansoori, R. Micaelo, and A. Garcia, 'Characterization of polymer capsules used for self-healing asphalt pavements', in *Functional Pavement Design*, 1st ed., S. Erkens, X. Liu, K. Anupam, and Y. Tan, Eds., CRC Press, 2016, pp. 1167–1174. doi: 10.1201/9781315643274-129.

[166] R. Vreeker, L. Li, Y. Fang, I. Appelqvist, and E. Mendes, 'Drying and Rehydration of Calcium Alginate Gels', *Food Biophysics*, vol. 3, no. 4, pp. 361–369, 2008, doi: 10.1007/s11483-008-9087-2.

[167] T. Al-Mansoori, R. Micaelo, I. Artamendi, J. Norambuena-Contreras, and A. Garcia, 'Microcapsules for self-healing of asphalt mixture without compromising mechanical performance', *Construction and Building Materials*, vol. 155, pp. 1091–1100, 2017, doi: 10.1016/j.conbuildmat.2017.08.137.

[168] J. Norambuena-Contreras, E. Yalcin, R. Hudson-Griffiths, and A. García, 'Mechanical and Self-Healing Properties of Stone Mastic Asphalt Containing Encapsulated Rejuvenators', *J. Mater. Civ. Eng.*, vol. 31, no. 5, p. 04019052, 2019, doi: 10.1061/(ASCE)MT.1943-5533.0002687.

[169] I. N. Ruiz-Riancho, A. Alexiadis, Z. Zhang, and A. Garcia Hernandez, 'A Discrete Multi-Physics Model to Simulate Fluid Structure Interaction and Breakage of Capsules Filled with Liquid under Coaxial Load', *Processes*, vol. 9, no. 2, p. 354, 2021, doi: 10.3390/pr9020354.

[170] Y. Zhang, M. Van De Ven, A. Molenaar, and S. Wu, 'Preventive maintenance of porous asphalt concrete using surface treatment technology', *Materials & Design*, vol. 99, pp. 262–272, 2016, doi: 10.1016/j.matdes.2016.03.082.

[171] Y. S. Kumbargeri, M. E. Kutay, and I. Boz, 'Effect of percent embedment on chip seal performance using FE modeling', in *Advances in Materials and Pavement Performance Prediction*, 1st ed., E. Masad, A. Bhasin, T. Scarpas, I. Menapace, and A. Kumar, Eds., CRC Press, 2018, pp. 583–586. doi: 10.1201/9780429457791-141.

[172] Q. Dai, 'Prediction of Dynamic Modulus and Phase Angle of Stone-Based Composites Using a Micromechanical Finite-Element Approach', *J. Mater. Civ. Eng.*, vol. 22, no. 6, pp. 618–627, 2010, doi: 10.1061/(ASCE)MT.1943-5533.0000062.

[173] M. Woldekidan, M. Huurman, E. Vaccari, and M. Poot, 'Meso Mechanical Analysis of AC Mixture Response', presented at the ISAP 2012: International Symposium on Heavy Duty Asphalt Pavements and Bridge Deck Pavements, China, 2012.

[174] A. Bekele, R. Balieu, D. Jelagin, N. Ryden, and A. Gudmarsson, 'Micro-mechanical modelling of low temperature-induced micro-damage initiation in asphalt concrete based on cohesive zone model', *Construction and Building Materials*, vol. 286, p. 122971, 2021, doi: 10.1016/j.conbuildmat.2021.122971.

[175] P. Liu *et al.*, 'Modelling and evaluation of aggregate morphology on asphalt compression behavior', *Construction and Building Materials*, vol. 133, pp. 196–208, 2017, doi: 10.1016/j.conbuildmat.2016.12.041.

[176] A. M. Ozdemir, E. Yalcin, M. Yilmaz, B. V. Kok, and E. Cambay, '3D numerical model of the creep response of hot mix asphalt prepared with capsules containing waste oil', *Petroleum Science and Technology*, pp. 1–20, 2023, doi: 10.1080/10916466.2023.2217833.

[177] S. Inozemtcev, D. Jelagin, E. Korolev, H. Fadil, M. N. Partl, and T. Do Trong, 'Experimental and numerical study on SMA modified with an encapsulated polymeric healing agent', *Mater Struct*, vol. 55, no. 9, p. 230, 2022, doi: 10.1617/s11527-022-02059-8.

[178] P. Jiao and A. H. Alavi, 'Artificial intelligence-enabled smart mechanical metamaterials: advent and future trends', *International Materials Reviews*, vol. 66, no. 6, pp. 365–393, 2021, doi: 10.1080/09506608.2020.1815394.

[179] Z. Jia, F. Liu, X. Jiang, and L. Wang, 'Engineering lattice metamaterials for extreme property, programmability, and multifunctionality', *Journal of Applied Physics*, vol. 127, no. 15, p. 150901, 2020, doi: 10.1063/5.0004724.

[180] J. A. Rosewitz, H. A. Choshali, and N. Rahbar, 'Bioinspired design of architected cement-polymer composites', *Cement and Concrete Composites*, vol. 96, pp. 252–265, 2019, doi: 10.1016/j.cemconcomp.2018.12.010.

[181] N. Friedman and A. Ibrahimbegovic, 'Overview of Highly Flexible, Deployable Lattice Structures Used in Architecture and Civil Engineering Undergoing Large Displacements', *YBL Journal of Built Environment*, vol. 1, no. 1, pp. 85–103, 2013, doi: 10.2478/jbe-2013-0006.

[182] M. Saafi, 'Design and Fabrication of FRP Grids for Aerospace and Civil Engineering Applications', *J. Aerosp. Eng.*, vol. 13, no. 4, pp. 144–149, 2000, doi: 10.1061/(ASCE)0893-1321(2000)13:4(144).

[183] Y. Nian, S. Wan, X. Wang, P. Zhou, M. Avcar, and M. Li, 'Study on crashworthiness of nature-inspired functionally graded lattice metamaterials for bridge pier protection against ship collision', *Engineering Structures*, vol. 277, p. 115404, 2023, doi: 10.1016/j.engstruct.2022.115404.

[184] Y. Darwish and M. ElGawady, 'Analysis of metamaterial bi-stable elements as energy dissipation systems', *BRS*, vol. 15, no. 4, pp. 151–159, 2019, doi: 10.3233/BRS-190161.

[185] Z. Gan, Y. Zhuge, D. P. Thambiratnam, T. H. Chan, T. Zahra, and M. Asad, 'Recent advances in auxetics: Applications in cementitious composites', *International Journal of Protective Structures*, vol. 13, no. 2, pp. 295–316, 2022, doi: 10.1177/20414196211062620.

[186] X. Y. Zhang, X. Ren, Y. Zhang, and Y. M. Xie, 'A novel auxetic metamaterial with enhanced mechanical properties and tunable auxeticity', *Thin-Walled Structures*, vol. 174, p. 109162, 2022, doi: 10.1016/j.tws.2022.109162.

[187] Y. Zhang, X. Ren, X. Y. Zhang, T. T. Huang, L. Sun, and Y. M. Xie, 'A novel buckling-restrained brace with auxetic perforated core: Experimental and numerical studies', *Engineering Structures*, vol. 249, p. 113223, 2021, doi: 10.1016/j.engstruct.2021.113223.

[188] F. Sun and L. Xiao, 'Bandgap Characteristics and Seismic Applications of Inerter-in-Lattice Metamaterials', *J. Eng. Mech.*, vol. 145, no. 9, p. 04019067, 2019, doi: 10.1061/(ASCE)EM.1943-7889.0001642.

[189] G. Aguzzi, A. Colombi, and E. N. Chatzi, 'Vibration mitigation via octet lattice structures', 2021, doi: 10.3929/ETHZ-B-000520521.

[190] X. Lu *et al.*, 'Triple tunability of phononic bandgaps for three-dimensional printed hollow sphere lattice metamaterials', *International Journal of Mechanical Sciences*, vol. 221, p. 107166, 2022, doi: 10.1016/j.ijmecsci.2022.107166.

[191] L. J. Gibson, 'Cellular Solids', *MRS Bull.*, vol. 28, no. 4, pp. 270–274, 2003, doi: 10.1557/mrs2003.79.

[192] D. Bhate, C. Penick, L. Ferry, and C. Lee, 'Classification and Selection of Cellular Materials in Mechanical Design: Engineering and Biomimetic Approaches', *Designs*, vol. 3, no. 1, p. 19, 2019, doi: 10.3390/designs3010019.

[193] W. Tao and M. C. Leu, 'Design of lattice structure for additive manufacturing', in *2016 International Symposium on Flexible Automation (ISFA)*, Cleveland, OH, USA: IEEE, 2016, pp. 325–332. doi: 10.1109/ISFA.2016.7790182.

[194] Z. Wang, Y. Zhang, and J. Liu, 'Comparison between five typical reinforced honeycomb structures', in *Proceedings of the 2015 International Conference on Advanced Engineering Materials and Technology*, Guangzhou, China: Atlantis Press, 2015. doi: 10.2991/icaemt-15.2015.134.

[195] W. Lee *et al.*, 'Effect of auxetic structures on crash behavior of cylindrical tube', *Composite Structures*, vol. 208, pp. 836–846, 2019, doi: 10.1016/j.compstruct.2018.10.068.

[196] W. Wu, W. Hu, G. Qian, H. Liao, X. Xu, and F. Berto, 'Mechanical design and multifunctional applications of chiral mechanical metamaterials: A review', *Materials & Design*, vol. 180, p. 107950, 2019, doi: 10.1016/j.matdes.2019.107950.

[197] C. Pan, Y. Han, and J. Lu, 'Design and Optimization of Lattice Structures: A Review', *Applied Sciences*, vol. 10, no. 18, p. 6374, 2020, doi: 10.3390/app10186374.

[198] A. Nazir, K. M. Abate, A. Kumar, and J.-Y. Jeng, 'A state-of-the-art review on types, design, optimization, and additive manufacturing of cellular structures', *Int J Adv Manuf Technol*, vol. 104, no. 9–12, pp. 3489–3510, 2019, doi: 10.1007/s00170-019-04085-3.

[199] T. A. Schaedler and W. B. Carter, 'Architected Cellular Materials', *Annu. Rev. Mater. Res.*, vol. 46, no. 1, pp. 187–210, 2016, doi: 10.1146/annurev-matsci-070115-031624.

[200] T. Maconachie *et al.*, 'SLM lattice structures: Properties, performance, applications and challenges', *Materials & Design*, vol. 183, p. 108137, 2019, doi: 10.1016/j.matdes.2019.108137.

[201] X. Zhou *et al.*, 'Advances in 3D/4D printing of mechanical metamaterials: From manufacturing to applications', *Composites Part B: Engineering*, p. 110585, 2023, doi: 10.1016/j.compositesb.2023.110585.

[202] F. M. Mwema and E. T. Akinlabi, 'Basics of Fused Deposition Modelling (FDM)', in *Fused Deposition Modeling*, in SpringerBriefs in Applied Sciences and Technology. , Cham: Springer International Publishing, 2020, pp. 1–15. doi: 10.1007/978-3-030-48259-6_1.

[203] A. M. Forster, 'Materials Testing Standards for Additive Manufacturing of Polymer Materials: State of the Art and Standards Applicability', National Institute of Standards and Technology, NIST IR 8059, May 2015. doi: 10.6028/NIST.IR.8059.

[204] J. Del Barrio and C. Sánchez-Somolinos, 'Light to Shape the Future: From Photolithography to 4D Printing', *Advanced Optical Materials*, vol. 7, no. 16, p. 1900598, Aug. 2019, doi: 10.1002/adom.201900598.

[205] C. Schmidleithner and D. M. Kalaskar, 'Stereolithography', in *3D Printing*, D. Cvetković, Ed., InTech, 2018. doi: 10.5772/intechopen.78147.

[206] K. V. Venkatesh and V. V. Nandini, 'Direct Metal Laser Sintering: A Digitised Metal Casting Technology', *J Indian Prosthodont Soc*, vol. 13, no. 4, pp. 389–392, Dec. 2013, doi: 10.1007/s13191-013-0256-8.

[207] J. P. Kruth, X. Wang, T. Laoui, and L. Froyen, 'Lasers and materials in selective laser sintering', *Assembly Automation*, vol. 23, no. 4, pp. 357–371, Dec. 2003, doi: 10.1108/01445150310698652.

[208] M. Galati and L. Iuliano, 'A literature review of powder-based electron beam melting focusing on numerical simulations', *Additive Manufacturing*, vol. 19, pp. 1–20, Jan. 2018, doi: 10.1016/j.addma.2017.11.001.

[209] C. Cai *et al.*, 'Comparative study on 3D printing of polyamide 12 by selective laser sintering and multi jet fusion', *Journal of Materials Processing Technology*, vol. 288, p. 116882, Feb. 2021, doi: 10.1016/j.jmatprotec.2020.116882.

[210] P. Drane, M. De Jesus-Vega, M. Inalpolat, J. Sherwood, and N. Orbey, 'Inductive quantification of energy absorption of high-density polyethylene foam for repeated blunt impact', *Proceedings of the Institution of Mechanical Engineers, Part L: Journal of Materials: Design and Applications*, vol. 234, no. 3, pp. 531–545, Mar. 2020, doi: 10.1177/1464420719899112.

[211] Q. M. Li, I. Magkiriadis, and J. J. Harrigan, 'Compressive Strain at the Onset of Densification of Cellular Solids', *Journal of Cellular Plastics*, vol. 42, no. 5, pp. 371–392, 2006, doi: 10.1177/0021955X06063519.

[212] F. N. Habib, P. Iovenitti, S. H. Masood, and M. Nikzad, 'Fabrication of polymeric lattice structures for optimum energy absorption using Multi Jet Fusion technology', *Materials & Design*, vol. 155, pp. 86–98, Oct. 2018, doi: 10.1016/j.matdes.2018.05.059.

[213] M. Avalle, G. Belingardi, and R. Montanini, 'Characterization of polymeric structural foams under compressive impact loading by means of energy-absorption diagram', *International Journal of Impact Engineering*, vol. 25, no. 5, pp. 455–472, May 2001, doi: 10.1016/S0734-743X(00)00060-9.

[214] 'Bituminous mixtures. Material specifications. Stone Mastic Asphalt. BS EN 13108-5'. BSI, London, 2016.

[215] 'Bituminous mixtures. Material specifications. Porous Asphalt. BS EN 13108-7'. BSI, London, 2016.

[216] 'Bituminous mixtures. Test methods. Laboratory mixing. BS EN 13108-35'. BSI, London, 2016.

[217] 'Bituminous mixtures. Test methods. Specimen preparation by impact compactor. BS EN 12697-30'. BSI, London, 2018.

[218] 'Bituminous mixtures. Test methods. Specimen prepared by roller compactor. BS EN 12697-33'. BSI, London, 2019.

[219] 'Bituminous mixtures. Test methods. Soluble binder content. BS EN 13108-1'. BSI, London, 2020.

[220] 'Bituminous mixtures. Test methods. Determination of particle size distribution. BS EN 13108-2'. BSI, London, 2019.

[221] M. Bahrami, J. Abenojar, and M. A. Martínez, 'Comparative Characterization of Hot-Pressed Polyamide 11 and 12: Mechanical, Thermal and Durability Properties', *Polymers*, vol. 13, no. 20, p. 3553, 2021, doi: 10.3390/polym13203553.

[222] L. Telen, P. Van Puyvelde, and B. Goderis, 'Random Copolymers from Polyamide 11 and Polyamide 12 by Reactive Extrusion: Synthesis, Eutectic Phase Behavior, and Polymorphism', *Macromolecules*, vol. 49, no. 3, pp. 876–890, 2016, doi: 10.1021/acs.macromol.5b00976.

[223] J. Liu, Z. Wang, X. Zhao, C. Yu, and X. Zhou, 'Quantitative evaluations on influences of aggregate surface texture on interfacial adhesion using 3D printing aggregate', *Construction and Building Materials*, vol. 328, p. 127022, 2022, doi: 10.1016/j.conbuildmat.2022.127022.

[224] 'Rigid cellular plastics. Determination of compression properties. BS EN ISO 844'. BSI, London, 2021.

[225] 'Plastics. Determination of tensile properties. Test conditions for moulding and extrusion plastics. BS EN ISO 527-2'. BSI, London, 2012.

[226] D. G. Altman and J. M. Bland, 'Standard deviations and standard errors', *BMJ*, vol. 331, no. 7521, p. 903, 2005, doi: 10.1136/bmj.331.7521.903.

[227] 'Bituminous mixtures. Test methods. Determination of the maximum density. BS EN 12697-5'. BSI, London, 2018.

[228] 'Bituminous mixtures. Test methods. Determination of bulk density of bituminous specimens. BS EN 12697-6'. BSI, London, 2020.

[229] 'Bituminous mixtures. Determination of void characteristics of bituminous specimens. BS EN 12697-8'. BSI, London, 2018.

[230] 'Bituminous mixtures. Test methods. Particle loss of porous asphalt specimens. BS EN 12697-17'. BSI, London, 2017.

[231] B. Iglewicz and D. C. Hoaglin, *How to detect and handle outliers*. in The ASQC basic references in quality control: statistical techniques, no. 16. Milwaukee, Wis: ASQC Quality Press, 1993.

[232] 'Bituminous mixtures. Test methods. Wheel tracking. BS EN 12697-22'. BSI, London, 2020.

[233] A. A. A. Molenaar, A. Scarpas, X. Liu, and S. M. J. G. Erkens, 'Semi-circular bending test; simple but useful?', *Association of Asphalt Paving Technologists Journal*, vol. 71, pp. 794–815, 2002.

[234] 'Bituminous mixtures. Test methods. Crack propagation by semi-circular bending test. BS EN 12697-44'. BSI, London, 2019.

[235] 'Road and airfield surface characteristics. Test methods. Method for measurement of slip/skid resistance of a surface: The pendulum test. BS EN 13036-4'. BSI, London, 2011.

[236] 'Characterization of pavement texture by use of surface profiles. Determination of mean profile depth. BS EN 13473-1'. BSI, London, 2019.

[237] N. H. Md Sai'aan, C. F. Soon, K. S. Tee, M. K. Ahmad, M. Youseffi, and S. A. Khagani, 'Characterisation of encapsulated cells in calcium alginate microcapsules', in *2016 IEEE EMBS Conference on Biomedical Engineering and Sciences (IECBES)*, Kuala Lumpur: IEEE, 2016, pp. 611–616. doi: 10.1109/IECBES.2016.7843522.

[238] 'Bitumen and bituminous mixtures. Test methods. Determination of complex shear modulus and phase angle. Dynamic Shear Rheometer (DSR). BS EN 14770'. BSI, London, 2012.

[239] T. Bai, Z. Cheng, X. Hu, L. Fuentes, and L. F. Walubita, 'Viscoelastic modelling of an asphalt pavement based on actual tire-pavement contact pressure', *Road Materials and Pavement Design*, vol. 22, no. 11, pp. 2458–2477, Nov. 2021, doi: 10.1080/14680629.2020.1766545.

[240] 'Plastics. Determination of tensile properties. General principles. BS EN ISO 527-1'. BSI, London, 2019.

[241] Y. Xiao, M. Meng, A. Daouadji, Q. Chen, Z. Wu, and X. Jiang, 'Effects of particle size on crushing and deformation behaviors of rockfill materials', *Geoscience Frontiers*, vol. 11, no. 2, pp. 375–388, 2020, doi: 10.1016/j.gsf.2018.10.010.

[242] 'Tests for mechanical and physical properties of aggregates Determination of loose bulk density and voids. BS EN 1097-3'. BSI, London, 1998.

[243] Y. Guo, V. Markine, W. Qiang, H. Zhang, and G. Jing, 'Effects of crumb rubber size and percentage on degradation reduction of railway ballast', *Construction and Building Materials*, vol. 212, pp. 210–224, 2019, doi: 10.1016/j.conbuildmat.2019.03.315.

[244] 'Methods of test for soils for civil engineering purposes. Classification tests and determination of geotechnical properties. BS EN 1097-3'. BSI, London, 2022.

[245] 'Standard Test Methods for Laboratory Compaction Characteristics of Soil Using Modified Effort'. 2009.

[246] M. Wasilewska, 'Evaluation of Skid Resistance of Wearing Course Made Of Stone Mastic Asphalt Mixture in Laboratory Conditions', *IOP Conf. Ser.: Mater. Sci. Eng.*, vol. 245, p. 022043, 2017, doi: 10.1088/1757-899X/245/2/022043.

[247] D. Mihora, K. Friedman, and J. Hutchinson, 'Friction Between Steel and Asphalt Without Gouging Under Representative Rollover Impact Pressures', in *Volume 11: Transportation Systems*, Houston, Texas, USA: American Society of Mechanical Engineers, 2012, pp. 213–217. doi: 10.1115/IMECE2012-88983.

[248] 'Abaqus Analysis User's Guide'. Dassault Systèmes Simulia Corp, RI, USA, 2014.

[249] R. A. Tarefder, A. M. Zaman, and W. Uddin, 'Determining hardness and elastic modulus of asphalt by nanoindentation', *International Journal of Geomechanics*, vol. 10(3), 2010.

[250] X. Cai, K. Wu, and W. Huang, 'Study on the optimal compaction effort of asphalt mixture based on the distribution of contact points of coarse aggregates', *Road*

Materials and Pavement Design, vol. 22, no. 7, pp. 1594–1615, 202AD, doi: 10.1080/14680629.2019.1710238.

[251] P. G. Roe and A. Dunford, 'The skid resistance behaviour of thin surface course systems', Transport Research Laboratory, PPR564, 2011.

[252] A. Garcia-Hernández, S. Salih, I. Ruiz-Riancho, J. Norambuena-Contreras, R. Hudson-Griffiths, and B. Gomez-Meijide, 'Self-healing of reflective cracks in asphalt mixtures by the action of encapsulated agents', *Construction and Building Materials*, vol. 252, p. 118929, 2020, doi: 10.1016/j.conbuildmat.2020.118929.

[253] D. Grossegger and A. Garcia, 'Influence of the thermal expansion of bitumen on asphalt self-healing', *Applied Thermal Engineering*, vol. 156, pp. 23–33, 2019, doi: 10.1016/j.applthermaleng.2019.04.034.

[254] J. F. Hair Jr, M. Sarstedt, L. Hopkins, and V. G. Kuppelwieser, 'Partial least squares structural equation modeling (PLS-SEM): An emerging tool in business research', *European Business Review*, vol. 26, no. 2, pp. 106–121, 2014, doi: 10.1108/EBR-10-2013-0128.

[255] G. N. Greaves, A. L. Greer, R. S. Lakes, and T. Rouxel, 'Poisson's ratio and modern materials', *Nature Mater*, vol. 10, no. 11, pp. 823–837, 2011, doi: 10.1038/nmat3134.

[256] H. Behbahani, M. M. Aliha, H. Fazaeli, and M. H. Rezaeifar, 'Effect of Characteristic Specifications on Fracture Toughness of Asphalt Concrete Materials', 2013.

[257] J. Litzka and B. Leben, 'The Way Forward for Pavement Performance Indicators across Europe', European Cooperation in Science and Technology, Brussels, Belgium, 2018.

[258] I. Pranjić, A. Deluka-Tibljaš, M. Cuculić, and S. Šurdonja, 'Influence of pavement surface macrotexture on pavement skid resistance', *Transportation Research Procedia*, vol. 45, pp. 747–754, 2020, doi: 10.1016/j.trpro.2020.02.102.

[259] O. Al-Ketan, R. K. Abu Al-Rub, and R. Rowshan, 'The effect of architecture on the mechanical properties of cellular structures based on the IWP minimal surface', *J. Mater. Res.*, vol. 33, no. 3, pp. 343–359, 2018, doi: 10.1557/jmr.2018.1.

[260] S. Yuan, C. K. Chua, and K. Zhou, '3D-Printed Mechanical Metamaterials with High Energy Absorption', *Adv Materials Technologies*, vol. 4, no. 3, p. 1800419, 2019, doi: 10.1002/admt.201800419.

[261] M. M. Sychov, L. A. Lebedev, S. V. Dyachenko, and L. A. Nefedova, 'Mechanical properties of energy-absorbing structures with triply periodic minimal surface topology', *Acta Astronautica*, vol. 150, pp. 81–84, 2018, doi: 10.1016/j.actaastro.2017.12.034.

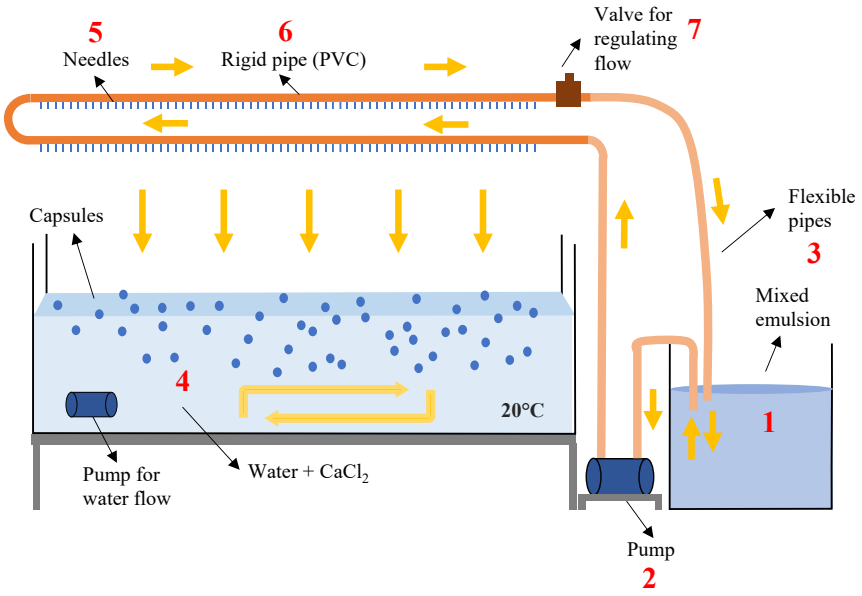
[262] I. Maskery *et al.*, 'Insights into the mechanical properties of several triply periodic minimal surface lattice structures made by polymer additive manufacturing', *Polymer*, vol. 152, pp. 62–71, Sep. 2018, doi: 10.1016/j.polymer.2017.11.049.

[263] M. Mohsenizadeh, F. Gasbarri, M. Munther, A. Beheshti, and K. Davami, 'Additively-manufactured lightweight Metamaterials for energy absorption', *Materials & Design*, vol. 139, pp. 521–530, 2018, doi: 10.1016/j.matdes.2017.11.037.

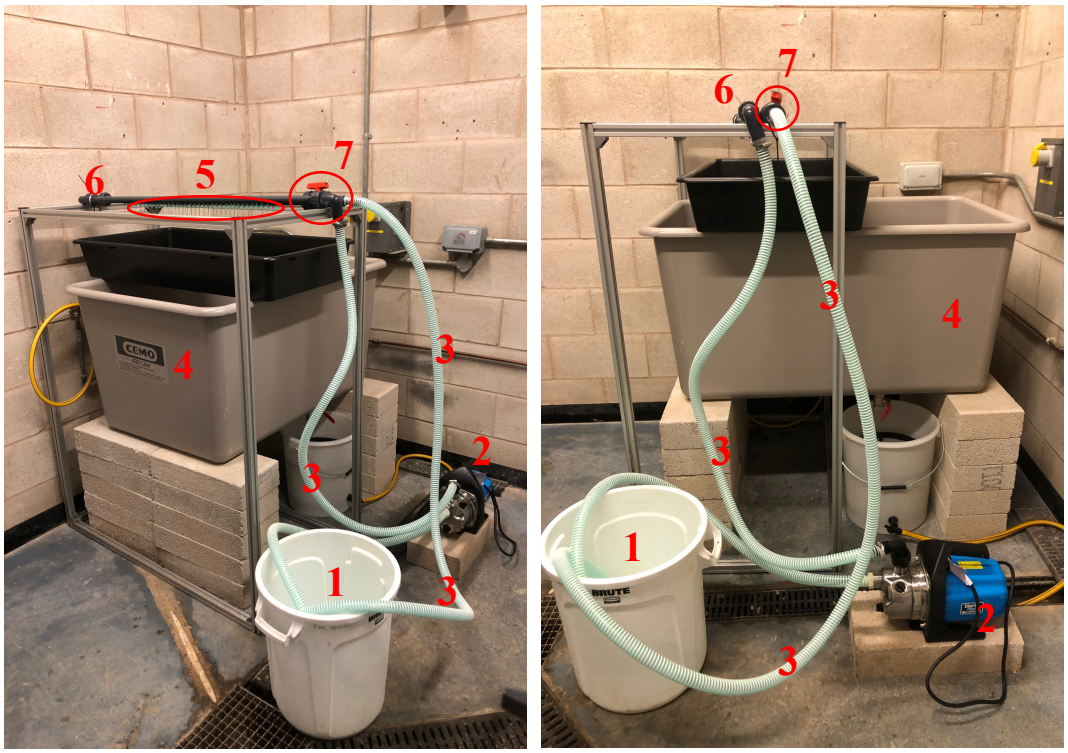
[264] S. Meister and D. Drummer, 'Influence of manufacturing conditions on measurement of mechanical material properties on thermoplastic micro tensile bars', *Polymer Testing*, vol. 32, no. 2, pp. 432–437, 2013, doi: 10.1016/j.polymertesting.2012.12.006.

Appendix I

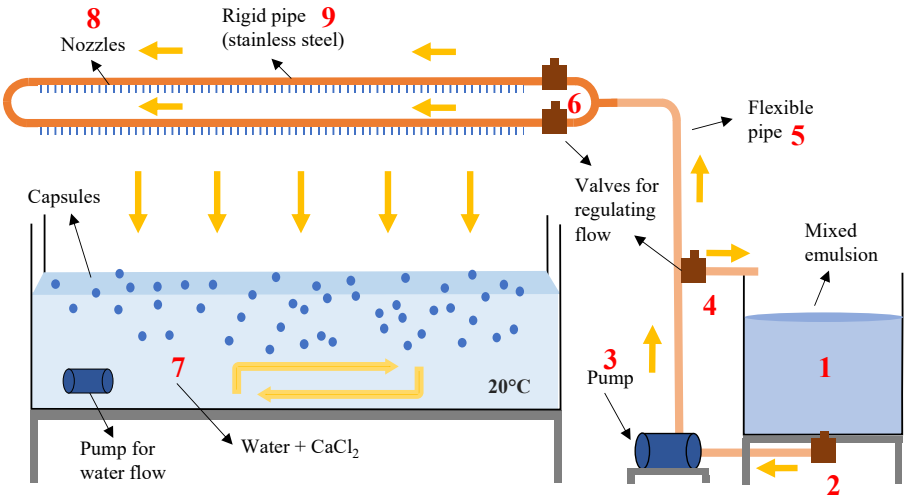
This appendix contains images depicting the prototype model and the final assembly of the encapsulation machine used to upscale the production of capsules to attain the required amount for manufacturing batches of asphalts at an asphalt plant. The first prototype model iterations were done between October 2019 and March 2020 and, after the university reopened the access to the research facilities, the final prototype model was assembled, as shown in the following pictures corresponding to October 2020. Tests on this prototype led to the assembly of the final model in March 2021, which is shown in the pictures as well.



Schematic representation of the prototype model.

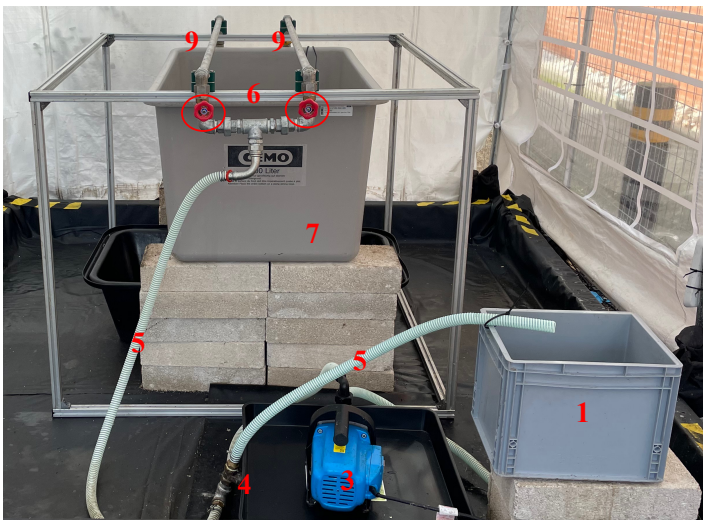


Images of the prototype mode.



Schematic representation of the final encapsulation machine.





Images of the final encapsulation machine.